EXPERIMENTAL STUDIES ON THE FREEZING OF MODERATE-SIZED RAINDROPS

DISSERTATION

For the award of the degree -
'Doctor rerum naturalium (Dr. rer. nat)' through the department:
F08 - Physics, Mathematics, and Informatics
of

JOHANNES GUTENBERG UNIVERSITY
MAINZ

submitted by
Martanda Gautam
Born 05.01.91 in Guwahati, India

Mainz, December 2025

Thesis accepted on the recommendation of

PD. Dr. Miklós Szakall	Supervisor
Prof. Dr. Holger Tost	Co-Supervisor

Oral examination: **February 20, 2026**

Abstract

Freezing of raindrops does not merely refer to the change in the physical phase from liquid to solid ice, but rather plays a pivotal role by influencing multiscale atmospheric processes. It influences precipitation formation and cloud dynamics, contributes to charge separation during thunderstorms, affects atmospheric chemistry and vertical redistribution of trace gases, collectively impacting cloud radiative effects and climate feedback processes. This study probes into the microphysical and chemical aspects that govern the vertical redistribution and retention or scavenging of trace gases during the freezing process, alongside a descriptive analysis of freezing timescales. An essential aspect of this study is the implementation of heterogeneous freezing in the immersion mode, wherein freezing is initiated through the activation of ice nucleating particles (INPs), immersed in the drops. Freezing experiments were performed using acoustic levitation of the raindrops inside a walk-in cold room facility.

In the preliminary stage, experiments were carried out to characterize the INPs, namely silver iodide (AgI) and chemically treated montmorillonite (MMT) clay powder. These experiments, performed at different temperatures and concentrations with AgI as INP, provided a strong foundation for subsequent investigation of chemical retention of trace gases during freezing in the proceeding stage.

Chemical retention during freezing is essentially important to understand the fate of trace gases dissolved in the aqueous phase, when they are vertically transported into the upper tropospheric regions during deep convections. Previous studies with micrometer sized (μm) cloud droplets established a strong dependence on the solubility and dissociation of the chemical species, characterized by the effective Henry's law constant (H^*). For moderate sized ($\sim$ mm) raindrops, nitric, acetic, and formic acids, and 2-nitrophenol were investigated, and no such dependencies on H^* have been observed. Rather, physical aspects such as drop size and fast ice-shell formation (within milliseconds) during freezing had a dominant role in the chemical retention of the investigated substances. Freezing timescale analysis via a parameter called retention indicator (RI) provided comparable results with smaller cloud droplets. An updated parameterization for relating RI and retention coefficient R is provided, which now includes both cloud droplets and raindrops.

High chemical retention majorly due to either fast or slow ice-shell formation time, provided a concrete path to further investigate the freezing dynamics of a raindrop for the final stage of this dissertation. This goal was realized through the modification of the existing acoustic levitator setup with high-speed cameras. Ice-shell formation times, as well as diabatic and adiabatic freezing times, were recorded and measured from freezing experiments with different INPs – AgI, illite-NX, and feldspar, alongside AgI with different concentrations of dissolved NaOH. Ice-shell formation time was found to be positively correlated with drop freezing temperatures and molar concentration of INPs (at fixed ambient temperatures), and negatively correlated with dissolved NaOH concentrations.

This study contributes to ongoing research on understanding the transport, retention, and redistribution of trace gases in chemistry coupled atmospheric models. It further sheds light on the freezing timescales, specifically on ice-shell formation times and their associated dependencies. These findings lay the groundwork to better understand the freezing dynamics, as well as provide a diverse experimental database to refine theoretical studies concerning raindrop freezing.

Zusammenfassung

Das Gefrieren von Regentropfen bezeichnet nicht nur den physikalischen Übergang von der flüssigen zur festen Phase, es spielt auch eine entscheidende Rolle bei der Beeinflussung von multiskaligen atmosphärischen Prozessen. Es wirkt sich auf die Niederschlagsbildung und Wolkendynamik aus, trägt zur Ladungstrennung während Gewittern bei, beeinflusst die Chemie der Atmosphäre sowie die vertikale Umverteilung von Spurengasen und wirkt damit insgesamt auf wolkenbedingte Strahlungseffekte und klimatisches Feedback. Die vorliegende Studie untersucht die mikrophysikalischen und chemischen Aspekte, die die vertikale Umverteilung sowie die Retention oder das Auswaschen von Spurengasen während des Gefrierprozesses bestimmen, und liefert zugleich eine Analyse der Zeitskalen des Gefrierens. Ein wesentlicher Bestandteil dieser Arbeit ist die Untersuchung von heterogenem Gefrieren im Immersionsmode, bei dem das Gefrieren durch in den Tropfen suspendierte Eiskeime (ice nucleating particles, INP) initiiert wird. Diese Experimente wurden mittels akustischer Levitation von Regentropfen in einer begehbaren Kältekammer durchgeführt.

In einer Voruntersuchung wurden Experimente zur Charakterisierung der verwendeten Eiskeime, Silberiodid (AgI) und chemisch behandeltes Montmorillonit (MMT), durchgeführt. Die bei unterschiedlichen Temperaturen und Konzentrationen mit AgI als Eiskeim durchgeführten Experimente bildeten die Grundlage für die nachfolgende Untersuchung der chemischen Retention von Spurengasen während des Gefrierens.

Die chemische Retention ist von wesentlicher Bedeutung, um zu verstehen, was während des konvektiven Transports in die obere Troposphäre mit Spurengasen geschieht, die in der flüssigen Phase gelöst sind. Frühere Studien mit mikrometergroßen Wolkentröpfchen zeigten eine starke Abhängigkeit von der Löslichkeit und Dissoziation der chemischen Spezies, charakterisiert durch die effektive Henry-Konstante ($H*$). Für millimetergroße Regentropfen wurden Salpetersäure, Essigsäure und Ameisensäure sowie 2-Nitrophenol untersucht, wobei keine vergleichbare Abhängigkeit von $H*$ festgestellt werden konnte. Stattdessen dominierten physikalische Faktoren – insbesondere die Tropfengröße und die extrem schnelle Bildung einer Eishülle (innerhalb von Millisekunden) – den Retentionsprozess der untersuchten Substanzen.

Die Analyse der Zeitskalen des Gefrierens anhand eines Parameters, des sogenannten Retentionsindikators (RI), ergab vergleichbare Ergebnisse wie bei kleineren Wolkentröpfchen. Eine Parametrisierung zur Verknüpfung von RI und dem Retentionskoeffizienten R wurde aktualisiert, sodass sie nun sowohl für Wolkentröpfchen als auch für Regentropfen verwendet werden kann.

Die hohe chemische Retention, die entweder durch eine schnelle oder eine langsame Entstehung der Eishülle verursacht wurde, führte zur weiteren Untersuchung der Dynamik des Gefrierens eines Regentropfens im abschließenden Teil dieser Dissertation. Dafür wurde der Aufbau des akustischen Levitators mit Hochgeschwindigkeitskameras modifiziert. Die Zeiten für die Bildung der Eishülle sowie die diabatischen und adiabatischen Gefrierzeiten wurden in Experimenten mit verschiedenen Eiskeimen – AgI, Illit-NX und Feldspat sowie AgI in Kombination mit unterschiedlichen NaOH-Konzentrationen – erfasst und analysiert. Die Zeit der Bildung einer Eishülle zeigte eine positive Korrelation mit den Gefriertemperaturen der Tropfen und der molaren Eiskeim-Konzentration (bei konstanten Umgebungstemperaturen) sowie eine negative Korrelation mit der Konzentration des gelösten NaOH.

Diese Studie leistet einen Beitrag zur laufenden Forschung über den Transport, die Retention und die Umverteilung von Spurengasen in chemisch gekoppelten atmosphärischen Modellen. Darüber hinaus liefert sie neue Erkenntnisse zu den Zeitskalen des Gefrierens, insbesondere zur Bildung der Eishülle und deren Abhängigkeiten. Die erzielten Ergebnisse bilden eine Grundlage für ein verbessertes Verständnis der Gefrierdynamik von Regentropfen und stellen zugleich eine breit gefächerte experimentelle Datenbasis zur Verbesserung theoretischer Studien zum Gefrieren von Regentropfen bereit.

Declaration

I hereby declare that I wrote the dissertation submitted without any unauthorized external assistance and used only sources acknowledged in the work. All textual passages which are appropriated verbatim or paraphrased from published and unpublished texts as well as all information obtained from oral sources are duly indicated and listed in accordance with bibliographical rules. I used Chat-GPT and Perplexity-AI for structural editing, grammatical corrections, translations, and scientific literature survey. In carrying out this research, I complied with the rules of standard scientific practice as formulated in the statutes of Johannes Gutenberg University Mainz to insure standard scientific practice.

Mainz, December 2025

Contents

List of Figures

List of Tables

Chapter 1

Introduction

1.1 Atmospheric aerosols

Atmospheric aerosols are suspensions of solid or liquid particles in the air, with sizes typically ranging from a few nanometers to several tens of micrometers. They originate from both natural sources, such as sea spray, desert dust, volcanic emissions, biogenic activity, as well as anthropogenic sources, including fossil fuel combustion, industrial activities, and biomass burning (Seinfeld and Pandis, 2016). Aerosols play a central role in atmospheric processes through several pathways. Physically, they act as cloud condensation nuclei (CCN) and ice-nucleating particles (INPs), thereby modulating cloud microphysical properties, precipitation efficiency, and radiative transfer (Pöschl, 2005). For example, chemically they participate in heterogeneous reactions that influence the oxidative capacity of the troposphere and the lifetimes of greenhouse gases (Andreae and Crutzen, 1997).

Our atmosphere comprises a rich and diverse array of chemical constituents vital to cloud microphysics, atmospheric chemistry, and climate dynamics. These include permanent gases such as nitrogen, oxygen, carbon dioxide, ozone, mineral dusts, as well as a myriad of compounds encompassing both organic and inorganic species. The organic fraction includes aldehydes, carboxylic acids, and various oxygenated and reduced hydrocarbons. Inorganics are chiefly nitrogen oxides (NOx) and ammonia-containing compounds, reflective of the high nitrogen abundance and its ensuing atmospheric transformations (Graedel, 2012). Low-molecular-weight carboxylic acids — specifically formic and acetic acid — are particularly noteworthy among organic species. They are ubiquitous, highly soluble, and chemically reactive (Chebbi and Carlier, 1996). Observational data attest to their widespread presence in clouds and rain (Chapman et al., 1986), snow and ice (Gunz and Hoffmann, 1990), and aerosol particles (Sempére and Kawamura, 1994; Chebbi and Carlier, 1996). Their pervasive occurrence reflects both direct emissions (e.g., from biomass burning, vegetation, soils, fossil fuel combustion) and abundant secondary production via photochemical oxidation of anthropogenic and biogenic volatile organic compounds (Paulot et al., 2011; Mungall et al., 2018).

Aerosols in the atmosphere can absorb and scatter both short and long wave radiation and subsequently alter planetary albedo, which are considered as the direct aerosol effects (Haywood and Boucher, 2000; Carlton et al., 2009). Indirect aerosol effects contribute to the alteration of in-cloud microphysical and radiative properties and affect cloud lifetimes (Haywood and Boucher, 2000; Lohmann and Feichter, 2005). One of the well-known indirect aerosol effects includes the increase in cloud condensation nuclei (CCN) concentration, also called the "Twomey effect" (Twomey, 1974). However, uncertainties and mismatch with global estimates of total indirect aerosol effects were reported in different modeling studies due to the use of different empirical relations, different background aerosol concentrations, and different microphysical treatments for estimating aerosol mass and cloud lifetimes (Lohmann and Feichter, 2005; Boucher et al., 2013). Beyond climate, aerosols also impact air quality and human health, contributing to respiratory and cardiovascular diseases due to fine particulate matter (PM) exposure (Cohen et al., 2017).

Particles emitted directly into the atmosphere from the sources mentioned earlier are termed as primary aerosols. Their size ranges from sub-micrometer to several micrometers, from both organic and inorganic sources. The atmospheric lifetime of aerosols lies in the order of a few hours to days for most coarse inorganic particles, such as dust, sea salt, except for fine volcanic ash. The organic aerosols can however, have slightly longer atmospheric lifetimes, lasting about 1-2 weeks (Kaufman and Tanré, 2003; Seinfeld and Pandis, 2016; Kanakidou et al., 2018). In contrast, secondary aerosols are not emitted directly in particulate form, they form via chemical transformation of precursor gases within the atmosphere (Baltensperger et al., 2005). Secondary organic aerosols (SOA) are a subcategory of secondary aerosols, originating from oxidation of volatile organic compounds commonly referred to as VOCs (Zheng et al., 2021). Oxidation pathways include photochemical reactions, aqueous-phase processing, and formation of oligomers (low molecular weight polymers with small repeated units), organosulfates, and organonitrates (Fan et al., 2022). Besides chemical transformation, SOA can also form via pathways such as organic nucleation, which was reported as a major source of new particle formation (NPF) in the atmosphere (Tröstl et al., 2016; Williamson et al., 2019). Some well known precursors for SOA formation consist of aromatic hydrocarbons (e.g., phenols and toluene), isoprene and monoterpenes (α-pinene), and various carbonyl compounds (Baltensperger et al., 2005).

1.2 Transport and uptake of aerosols

Biogenic and anthropogenic emissions both contribute substantially to atmospheric chemical composition. However, convective transport, and in particular, the vertical redistribution it affords, is equally critical. Deep convection facilitates the rapid mixing of trace gases and aerosols from the planetary boundary layer (PBL) into the upper troposphere and lower stratosphere (UTLS). For instance, case studies have documented the injection of water vapor several kilometers above the tropopause, significantly influencing stratospheric humidity and radiative balance (Homeyer et al., 2014). In the Amazon region, numerical models reveal that up to 17% of boundary-layer air may reach altitudes above 10 km during deep convective events, while downdrafts can transport free-tropospheric species downward, impacting boundary-layer chemistry (Bardakov et al., 2022). Furthermore, in weather systems such as the Asian monsoon anticyclone, deep convection efficiently transports surface-emitted aerosol precursors into the upper atmosphere, substantially enhancing aerosol concentrations near the tropopause. On an annual basis, approximately 15% of the Northern Hemisphere's stratospheric aerosol surface area is attributable to this mechanism, which is comparable to contributions from small volcanic eruptions (Yu et al., 2017). It is shown in recent studies that models sometimes underestimate the available organic content (Bardakov et al., 2021). For example, Williamson et al. (2019) showed that NPF is not adequately accounted for in tropical convection cases in higher latitudes. Thus, vertical transport and redistribution of aerosols can potentially impact the global radiation budgets and overall climate (Tsigaridis et al., 2014; Shrivastava et al., 2017). In the following sections, the focus is not on the physical process of transporting trace gases vertically, but rather on some of the microphsyical and chemical aspects that occur alongside the physical transport process during convective updrafts.

1.2.1 Chemical retention of trace gases

An important aspect in terms of transport and redistribution of aerosols is the phenomenon of chemical retention, wherein a chemical substance can be retained during freezing of droplets. Chemical retention is specifically important for substances that can be exchanged between the gaseous and aqueous phases in the atmosphere. Trace gases present in aqueous phase in cloud droplets or raindrops can either be trapped in the ice phase during freezing, scavenged via precipitation, or re-volatilized into the gas phase higher up in the atmosphere via sublimation (Pruppacher and Klett, 2010). Such freezing and revolatilization events occurring during convective updrafts could be a possible explanation for the underestimation of organic matter observed in the higher latitudes (Barth et al., 2007). Another possible pathway would be the structural incorporation of organics into growing ice structures, also termed as diffusional ice-uptake (Kolb et al., 2010). These freezing processes during vertical transport are shown in Fig. 1.1. Within the boundaries of the chosen subject matter, transport and redistribution due to chemical retention during freezing were primarily researched in this thesis.

Existing literature highlights both experimental studies and theoretical frameworks on the significance of chemical retention in the atmosphere. Around 1980-90s Iribarne et al. (1983), Lamb and Blumenstein (1987), and Iribarne et al. (1990) experimentally investigated the chemical retention of sulfur dioxide during freezing of supercooled droplets. Snider et al. (1992) and Snider and Huang (1998) performed experiments investigating the chemical retention of hydrogen peroxide and molecular oxygen. This database was expanded by von Blohn et al. (2011, 2013) with their chemical retention experiments in the Mainz vertical wind tunnel for ammonia, nitric acid, hydrochloric acid, in addition to sulfur dioxide and hydrogen peroxide. Jost et al. (2017) and Borchers et al. (2024) performed further studies on

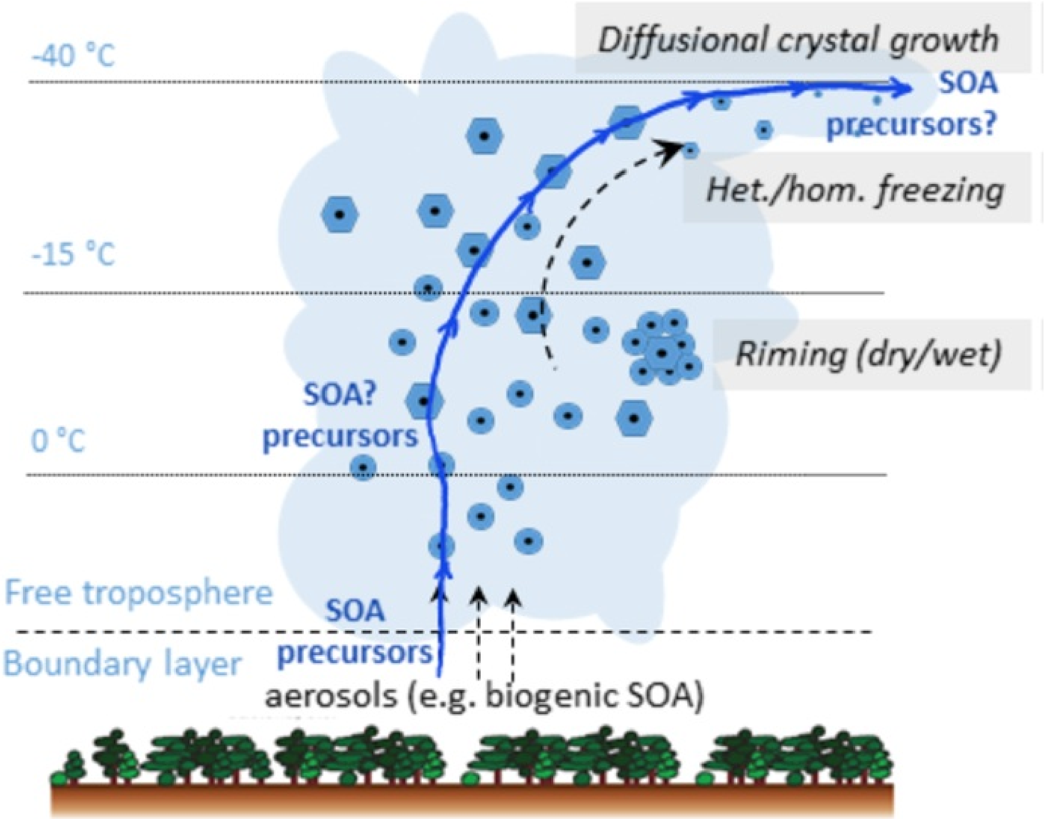

Figure 1.1: Schematic for vertical transport of trace gases such as SOA precursors in a convective system.

chemical retention from low molecular weight organics, such as acetic, formic, oxalic, malonic acid, to larger organics such as α-pinene derivatives and aromatic phenols, also with the vertical wind tunnel setup. A common feature of these experimental studies was riming of supercooled droplets with dissolved chemicals as their freezing mechanism. Riming refers to the freezing of supercooled droplets upon collision with an existing ice particle (Pruppacher and Klett, 2010). The supercooled droplets in the above mentioned experimental studies were in the μm size range. However, chemical retention for mm sized raindrops has not been studied so far, experimentally.

Mari et al. (2000) and Barth et al. (2001) reported that convective clouds strongly influence the distribution of trace gases in the troposphere. Solubility of the trace gases was a key factor that governs their vertical transport – highly soluble substances are easily precipitated out. Retention of trace gases in the ice phase and revolatilization critically control their scavenging efficiencies. Further modeling studies (Bela et al., 2016; Cuchiara et al., 2020; Ryu and Min, 2022) and model intercomparision studies (Barth et al., 2007; Tost et al., 2010) also confer the significance of solubility and ice phase retention of trace gases, alongside high uncertainties among convection parameterizations used for different models. Lack of observations and experimental studies was also mentioned to be an important factor in the proper representation of vertical transport of trace gases. For an experimental investigation of chemical retention for moderate sized raindrops in convective systems, the freezing-related aspects must be addressed as a necessary prerequisite.

1.3 Ice nucleation

Ice particles in the atmosphere play a very significant role in governing cloud microphysical properties by influencing important in-cloud processes such as precipitation, radiative transfer, and cloud electrification (Cantrell and Heymsfield, 2005; Kanji et al., 2017). In the context of atmospheric chemistry, ice particles also influence tropospheric compositions via photochemistry and new particle formation, adsorption, and scavenging of trace gases (Abbatt, 2003; Seinfeld and Pandis, 2016; Williamson et al., 2019). As such, understanding ice formation mechanisms has been a core subject for atmospheric research over the decades, in the form of in-situ measurements, laboratory experiments, and via theoretical modeling approaches (Hoose and Möhler, 2012; Kanji et al., 2017).

The intrinsic nature of the transformation of water from liquid-phase to ice-phase in clouds plays an important role in cloud formation and precipitation (Korolev and Mazin, 2003). Vali et al. (2015) in their proposal for ice nucleation terminology stated that ice nucleation is "the first appearance of thermodynamically stable ice phase". Freezing of liquid water to ice in the atmosphere could be either homogeneous or heterogeneous (Pruppacher and Klett, 2010). Homogeneous freezing refers to ice formation directly from supercooled water, without the help of any foreign substances. Supersaturation in the atmosphere refers to the state where the vapor pressure of water is much greater than the equilibrium saturation vapor pressure of the air. Very high supersaturation ($>$ 150%) and very low temperatures ($<$ -36 °C) are essential conditions for homogeneous mode of ice nucleation, which are seldom found in the natural atmosphere, mostly in cirrus clouds. The occurrence of homogeneous ice nucleation is less frequent than that of heterogeneous ice nucleation (Yau and Rogers, 1996; Vali et al., 2015). Heterogeneous ice nucleation or heterogeneous freezing refers to the mechanism where freezing is initiated or aided by the presence of a foreign particle (aerosols, existing ice particles, or other foreign objects). Such freezing mechanisms occur at lower supersaturation or supercooling as compared to the homogeneous mode. Heterogeneous mode of freezing in the atmosphere proceeds through three major pathways:

(a) Deposition mode

(b) Immersion Mode

(c) Contact Mode

A schematic of these freezing processes is shown in Fig. 1.2. Deposition mode (a) pertains to the deposition of saturated water vapor on an ice nucleating particle (INP) such as an aerosol particle. Here, ice nucleation can take place directly on an INP at conditions higher than ice supersaturation i.e., relative humidity w.r.t. ice is $>$ 100% (Vali et al., 2015; Kanji et al., 2017). Deposition mode of nucleation is characterized by the absence of a liquid phase prior to ice formation, however, the extent of deposition INPs remains unclear and is not expected to be significant in mixed-phase clouds (Kanji et al., 2017).

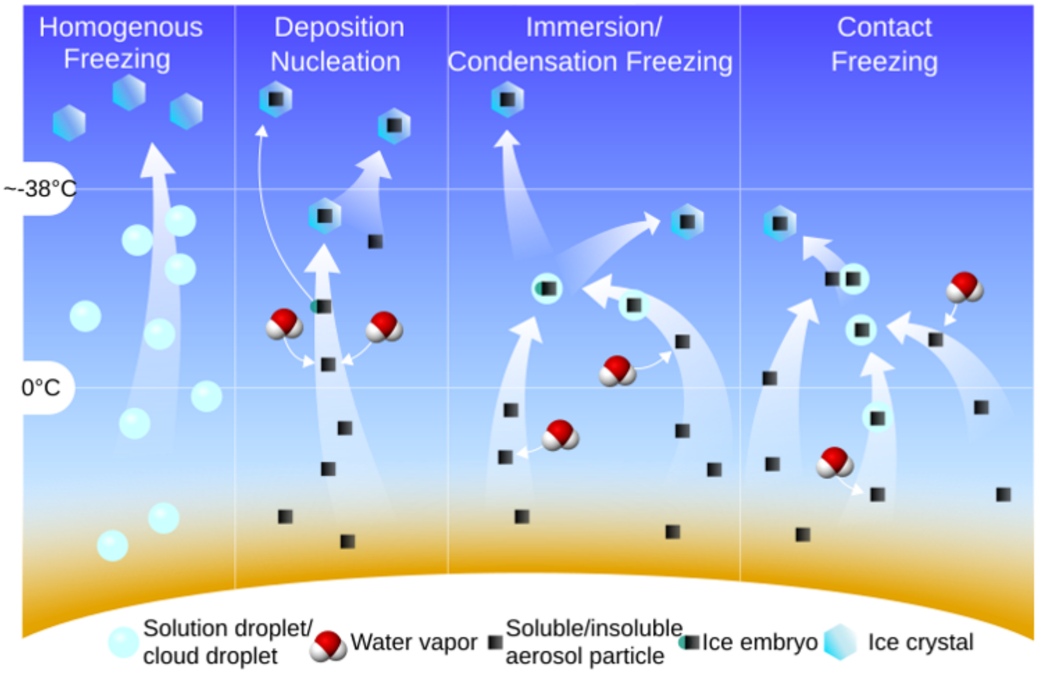

Figure 1.2: Different mechanisms for ice nucleation. Used in accordance with the Creative Commons Non-commercial 4.0 International license.
(Source: https: //commons.wikimedia.org/wiki/File:Ice_Nucleation_Mechanisms.svg)

The immersion mode (b) refers to the activation of INPs immersed inside supercooled droplets. This mechanism of freezing is observed and reported to be the most significant mode of freezing of liquid water in mixed phase clouds (Murray et al., 2012; Kanji et al., 2017). The range of immersed INPs in the atmosphere includes a wide range of mineral dust particles, metal oxides, organic compounds, as well as airborne biogenic particles such as pollen, bacteria, fungal spores (Cantrell and Heymsfield, 2005; Hoose and Möhler, 2012; Kanji et al., 2017; DeMott et al., 2018).

In contact mode (c), as the name suggests, freezing is characterized through contact of INPs on supercooled droplets at the air-liquid-particle interface (Vali et al., 2015). Contact freezing can occur at warmer temperatures than immersion freezing, potentially due to the low energy barrier for ice formation at the air-water interface. (Hussain and Haji-Akbari, 2021; Kar et al., 2021). Another mode of freezing, sometimes combined with immersion freezing, is the condensation freezing, where the formation of liquid on cloud condensation nuclei and the simultaneous initiation of freezing occur. Vali et al. (2015) states that condensation freezing is not as fully established as the other three modes of nucleation.

Among the various freezing processes, immersion mode has been implemented in this study to initiate the freezing of raindrops in the experiments, due to its prominent role in natural mixed-phase clouds. Furthermore, the wide diversity of INPs found in the atmosphere influences the freezing rates and introduces substantial variability in ice formation within clouds, which makes immersion freezing a compelling subject of research.

Chapter 2

Objectives and outline

Effective implementation of immersion freezing requires a detailed understanding of the freezing characteristics of INPs. Comprehensive INP characterization would eventually facilitate a systematic investigation of chemical retention of dissolved substances during raindrop freezing. Based on the theory introduced in the previous section, the following research questions are formulated:

- S1: How is ice nucleating behavior affected due to the incorporation of metal ions in montmorillonite (MMT) samples?
- S2: Do chemical retention vary with drop sizes, for micrometer-sized cloud droplets to millimeter-sized raindrops?
- S3: Are chemical species retained differently during freezing, for single components and their binary mixtures?
- S4: Which physical and chemical factors govern the timescale of ice-shell formation, and how does this timescale vary with different types of INPs?
- S5: To what extent do dissolved solutes influence the kinetics of freezing, and how can their effects be parameterized or represented in modeling frameworks?

The objectives of this dissertation are developed based on the above mentioned research questions, and are listed as follows:

- O1: Perform immersion freezing experiments with an existing acoustic levitator setup inside a walk-in cold room facility, at different temperatures, INP concentrations, and using different INP species (S1, S4).
- O2: Investigate chemical retention of substances, as single components and their binary mixtures, for freezing of mm sized raindrops, using the acoustic levitator setup (S2, S3).

- O3: Modifications to existing acoustic levitator setup to investigate freezing timescales during freezing of raindrops with high-speed cameras (S4, S5).
- O4: Experimentally study the chemical retention of nitroaromatics, specifically for cloud droplet sizes (in μm) with a vertical wind tunnel setup (S2).
- O5: Investigate chemical retention of ambient filter samples for raindrops with the acoustic levitator (S2).

These aforementioned objectives were achieved in this dissertation as delineated below:

In Chapter 3, the conceptual framework for the dynamics of a freezing raindrop is explained, along with mathematical formulations used for analyzing the freezing experiments. Furthermore, the chemical retention during freezing, with some aspects of freezing timescale analysis, is discussed. And an overview of the experiential setup - acoustic levitator is also introduced in Chapter 3.

Chapter 4 discusses the results of immersion freezing experiments by characterizing different INPs - silver iodide (AgI), and metal doped-montmorillionite (MMT) at ambient cold room temperatures ranging from -15 to -28 °C, and at different concentrations. Chapter 4 presents the results of the first objective.

Chapter 5 reveals the results from retention experiments (second objective) for single components and their binary mixtures. These experiments utilize the acoustic levitator setup, followed by quantitative analysis of the dissolved substances using Ion chromatography (IC) and High performance liquid chromatography (HPLC) instruments. This chapter highlights the impact of physical aspects such as surface to volume ratios and ice-shell formation during freezing of raindrops, as the controlling factor for high chemical retention observed during the experiments.

Chapter 6 further investigates the freezing timescales. Here, freezing experiments were performed with the same setup, and the freezing process was recorded using two high-speed cameras. In addition to AgI, illite-NX and feldspar were used as INPs. Furthermore, NaOH was also added to the AgI solution, to study the effect of dissolved solutes on the freezing timescales. Ice-shell formation time, diabatic and adiabatic freezing times were investigated in this chapter (third objective).

Chapter 7 provides an overview of the collaborative works performed in addition to the topics mentioned above. Two major tasks were accomplished within these collaborations: Firstly, investigating retention during freezing of raindrops for ambient aerosols, sampled in Beijing. Secondly, retention during riming of cloud droplets with the vertical wind tunnel setup was investigated for α-pinene oxidation products and nitro-aromatic compounds.

These works briefly summarize the results of the fourth and fifth objectives, and full citations are provided for reference.

An assessment of the uncertainties and potential sources of error inherent in this work is discussed in Chapter 8. Chapter 9 subsequently synthesizes the key findings of this dissertation and outlines their broader implications and future research outlook.

Author's note: Chapter 5 has been published in the peer-reviewed journal, Atmospheric Physics and Chemistry. The sections, tables, figures, and equations have been renumbered for maintaining uniformity of the dissertation. These editorial changes have not affected the original content. In the case of co-authored articles, personal contributions to each work have been clearly specified in Chapter 7. All symbols are in SI units, unless mentioned otherwise.

Chapter 3

Theoretical background

3.1 Dynamics of a freezing drop

In this section, the drop freezing processes and the associated key aspects while analyzing the experimental results are discussed. Figure 3.1 shows the evolution of the drop surface temperature as it undergoes freezing. The supercooling and subsequent freezing of the drops were analyzed using the description postulated by Hindmarsh et al. (2003), where they state that the freezing process can be divided into four stages. The first stage is the supercooling stage. For the levitated drops, the drop surface temperature is initially warmer than 273.15 K or 0 °C when injected in the acoustic field and gradually cools down with time. The supercooling rate of the levitated drop is dependent on the amount of heat that is transferred from the relatively warm drop to its environment. In the absence of an INP, i.e., for a drop with pure water, this supercooling stage will continue until it reaches an equilibrium temperature, usually seen after stage 4 (Hindmarsh et al., 2003). The actual freezing of the levitated drop takes place in stages 2 and 3. The second stage is the adiabatic freezing stage. Here, rapid crystal growth can be seen immediately after the freezing or phase change is initiated. This is a relatively short stage, and a very tiny fraction of the latent heat of freezing is transferred to the environment (Pruppacher and Klett, 2010). The majority of the latent heat released is absorbed by the liquid part, which raises the temperature of the drop to 0 °C.

The third stage is the diabatic freezing stage, which has a much slower freezing rate compared to its previous stage. Diabatic freezing is characterized by the rate of heat transfer from the drop to its environment, as the remainder of the drop undergoes freezing. The flattened section in the third stage, shown in Fig. 3.1 at 0 °C, corresponds to a phase where solid ice and liquid water are at equilibrium. As the liquid phase solidifies with time, the drop surface temperature decreases gradually. After the drop is entirely frozen, it enters a cooling stage shown as stage 4 in Fig. 3.1, until it reaches an equilibrium with the ambient conditions. This drop surface temperature evolution measured by the infrared thermometer, in the M-AL setup, is shown in Fig A.1.

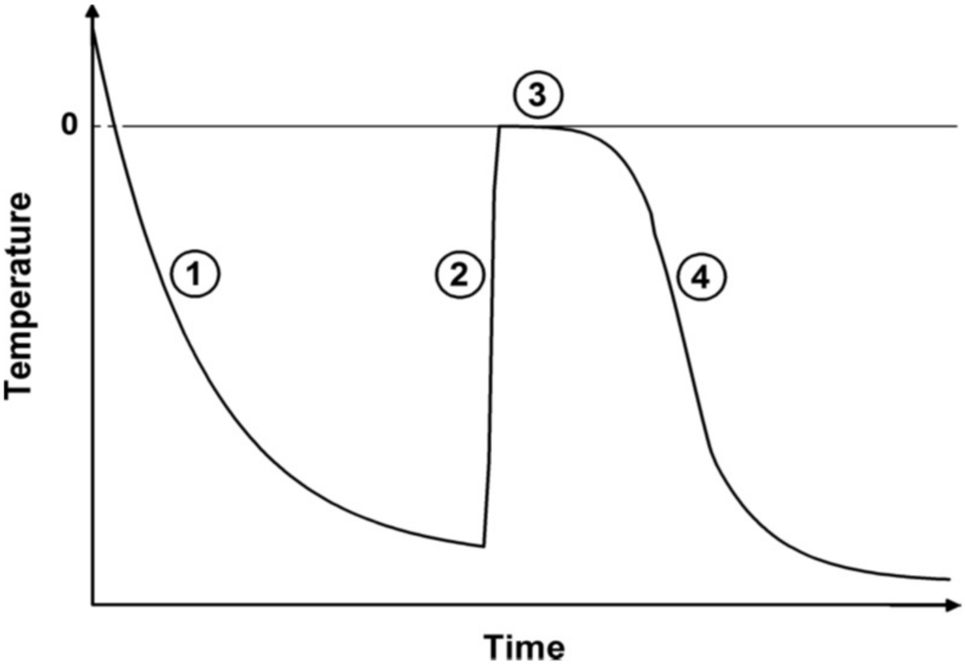

Figure 3.1: A schematic of the temporal evolution of a freezing raindrop. Adopted from Szakáll et al. (2021).

During the freezing of a raindrop, after the initiation of freezing, i.e., the rapid crystal growth stage, an ice-shell may be formed around the drop (Pruppacher and Klett, 2010; Lauber et al., 2018). If freezing is initiated at the center of a drop and ice crystal growth proceeds outward, then the ice-shell may not be formed (Pruppacher and Klett, 2010; Stuart and Jacobson, 2004). Both ice-shell formation and adiabatic freezing are dependent on the rate of ice crystal growth in water (Pruppacher and Klett, 2010). Once an ice-shell is formed, the freezing proceeds radially inwards, encompassing the semi-frozen ice-water liquid core of the drop. Solidification of liquid to ice exerts mechanical stress on the ice-shell. Recent studies have shown that due to high internal pressure built up inside a semi-frozen drop during freezing, the ice-shell could deform from its nearly spherical geometry, and potentially lead to cracking of the ice-shell, followed by ejecting of splinters (Lauber et al., 2018; Kleinheins et al., 2021). These ejections of splinters or cracking during freezing of drops serve as a source of secondary ice production (SIP) in natural systems, further leading to rapid in-cloud glaciation and precipitation (Field et al., 2017; Korolev and Leisner, 2020). The probability of cracking of ice-shells during freezing rather depends on the strength of the ice-shell, the degree of radial symmetry of cooling, and drop sizes (Wildeman et al., 2017).

3.2 Ice nucleating efficiency

Efficient ice nucleation depends on several factors such as the size of INPs, their crystal structure, and chemical bonding capacity (Pruppacher and Klett, 2010; Vali, 2014). Ice nucleation can be described numerically by two different approaches, stochastic and singular. A classical nucleation theory describes freezing as a stochastic process, which describes how the liquid phase transforms into the solid phase due to the growth of ice nuclei (Hoose and Möhler, 2012; Vali, 2014). According to Ickes et al. (2015), classical nucleation theory describes the probability of ice nucleation to be governed by both thermodynamic and kinetic factors. The probability of homogeneous ice nucleation is highly sensitive to the interfacial surface tension between ice and liquid water. In addition, the activation energy also strongly influences the rate of the nucleation process. Heterogeneous ice nucleation can be formulated by two approaches: stochastic approach and singular approach.

3.2.1 Stochastic approach

Variations of classical nucleation theory were also used for parameterizing heterogeneous nucleation, which is known as the stochastic approach. Stochastic approach considers heterogeneous freezing events occur with a certain probability over time, as ice nucleation occurs from random fluctuations. The longer a drop remains at a given supercooling temperature, the probability of freezing increases. Freezing is treated as both a time and temperature dependent process in the stochastic approach (Kanji et al., 2017; Vali, 2014).

A freezing rate F can be determined by the frequency of freezing events (see Vali (2014) for more details), as a function of time t and temperature T as

$$F(t,T) = -\frac{1}{N_o - N_f}\frac{dN_f}{dt} \tag{3.1}$$

N_o is the total number of samples, N_f number of frozen samples. If we consider the frozen fraction N_f/N_o of the sample, as f_{ice}, Eq. 3.1 can be rewritten as

$$F(t,T) = -\frac{1}{1 - f_{ice}}\frac{df_{ice}}{dt} \tag{3.2}$$

Assuming freezing rate at a constant ambient temperature, $F_T(t)$ and integrating Eq. 3.2, freezing rate takes the form

$$F_T(t) = -\frac{ln(1 - f_{ice})}{t} \tag{3.3}$$

The nucleation rate J takes into consideration the probability of ice nucleation per unit time for identical ice embryos/nuclei. In case of homogeneous nucleation, the nucleation rate J_v can be represented as freezing rate per unit volume, i.e $J_v = F/V$, where V is the volume. For heterogeneous nucleation, the nucleation rate (J_s) is expressed in terms of the probability of ice nucleation per unit surface area of an INP. At this point, it has to be considered that among a large population of drops, the size of the individual nucleating particles is the same, and all the drops contain the same concentration of INPs. Additionally, any part of a drop surface area will have an equal probability distribution of ice nucleating sites as other drops. This assumption mainly arises due to unknown characteristics of nucleating sites and lack of empirical approaches for identifying such sites (Vali, 2014). Nevertheless, the nucleation rate for heterogeneous freezing can be expressed as:

$$J_s = F/A \tag{3.4}$$

where A is the particle surface area for each drop and can be determined as:

$$A = V \times c \times SSA \tag{3.5}$$

In Eq. 3.5, c is the mass concentration of the INP in a sample solution in g/L, SSA is the specific surface area of the INP per unit mass with units m^2/g. SSA indicates the number of potential nucleation sites an INP can provide for heterogeneous ice nucleation. A common method for determining the SSA is using the Brunauer–Emmett–Teller (BET) method, where the adsorption of a gas on a material surface is measured, and the adsorbed gas on the material is correlated with the surface area (Ambroz et al., 2018). BET measurements are highly sensitive to the molecular structure of a material and could sometimes overestimate the SSA values, for example, when adsorbent gas gets deposited in multiple layers on top of already adsorbed gaseous molecules, rather than on the solid surface of the material (Ambroz et al., 2018). Cloud chamber experiments have been used to measure SSA from their particle size distribution, however, there could be mismatches in the measured SSA values for the same material due to different size resolutions of both these SSA measurement techniques (Hiranuma et al., 2021).

3.2.2 Singular approach

Another well established approach for characterizing heterogeneous freezing is the singular or deterministic approach, which is an empirical description for evaluating the ice nucleating rates of an INP. This approach is based on observations that freezing of INPs would occur at a certain temperature, independent of time, once the ice nucleating sites reach the characteristic temperature (Hoose and Möhler, 2012; Vali et al., 2015). Within the scope of this study, this deterministic approach has been implemented for characterizing the INPs, where ice nucleation starts at material specific ice nucleating active sites (INAS) below a specific temperature.

The cumulative nucleus spectra $K(T)$ with reference to INAS density $n_s(T)$ and A is obtained from Vali et al. (2015) as

$$K(T) = n_s(T) \times A \tag{3.6}$$

Furthermore, the INAS density and frozen fraction can be related from Szakáll et al. (2021) as

$$n_s(T) = -\frac{ln(1 - f_{ice}(T))}{A} \tag{3.7}$$

Alternately rearranging Eq. 3.7, f_{ice} also can be expressed as

$$f_{ice}(T) = 1 - exp(-n_s(T) \times A) \tag{3.8}$$

Here, $f_{ice}(T) = N_f(T)/N_o$ relation mentioned earlier, is the cumulative fraction of drops that froze between O °C and given temperature T. Majority of the analysis for the immersion freezing experiments reported in this dissertation utilizes Eq. 3.7 and Eq. 3.8.

Both these approaches have their advantages and disadvantages (Niedermeier et al., 2011; Kanji et al., 2017). Several studies have reported that time dependent stochastic effects are of less importance as compared to the dominance of active nucleating sites for an INP (Connolly et al., 2009; Wright et al., 2013; Vali, 2014; Kanji et al., 2017). The choice of approach clearly depends on the type of freezing experiment or modeling study performed (Vali, 2014; Diehl et al., 2014).

3.3 Chemical retention - formulations

Understanding the underlying chemical and microphysical processes during a macrophysical transport event, such as in convective systems, is crucial in estimating atmospheric compositions and their subsequent effect on our climate. The partitioning of dissolved chemicals during such vertical transport and subsequent freezing from liquid to ice phase depends on solute properties such as solubility and dissociation, characterized by the dimensionless effective Henry's constant H^*. Classical Henry's law states that the equilibrium concentration of a gas dissolved in a liquid is proportional to its partial pressure in the gas phase (Henry, 1803). H^* accounts for both the solubility of a gas and, in addition, the aqueous phase chemical reactions (dissociation). Chemical species with a high H^* are most likely to be retained, whereas for substances with low H^*, freezing conditions such as temperature, pH, ventilation, and drop size have a significant effect on the chemical retention (Stuart and Jacobson, 2003). The inherent phenomenon of dissolved trace gases remaining inside a hydrometeor during freezing is quantified via two characteristic metrics: a retention coefficient - R and a retention indicator -RI (Stuart and Jacobson, 2003; Jost et al., 2017).

Retention coefficient can be defined as the fraction of the chemical substance retained inside a frozen hydrometeor compared to its initial liquid phase concentration. Substances that are completely retained during freezing have a retention coefficient value of 1. Jost et al. (2017) showed that R can be represented as a function of H^* via a sigmoidal relationship. This sigmoidal relationship was further augmented by Borchers et al. (2024) to include a wide range of organic compounds as well. The parameter RI is a ratio of the solute mass expulsion time to the freezing time of a hydrometeor. Additionally, a well-established correlation exists between H^* and a RI parameter, which links experimentally derived R with model-derived estimates (Stuart and Jacobson, 2003, 2004).

3.3.1 Retention coefficient

The retention coefficient R is the fraction of solute mass remaining in the ice phase, as compared to its initial liquid phase concentration before freezing. Mathematically, it can be expressed in simple terms as

$$R = \frac{[ice - phase]}{[liquid - phase]} \tag{3.9}$$

Here, mass concentrations are indicated by square brackets. During experiments, a concentration tracking tracer is present, which accounts for any changes in mass concentrations in the course of the quantitative analyses. The selected tracer has a known retention coefficient of 1. Depending on the experimental setup, Eq. 3.9 may change its form slightly. For example, in experiments for deriving retention coefficients during riming using a wind tunnel setup (Jost et al., 2017; Borchers et al., 2024), in addition to quantifying the mass of a frozen rime collector (a graupel in their case), the mass of ice accumulated on reference surfaces (Teflon tubes and a liquid nitrogen cooled surface) is used for calculating R.

Another aspect in this type of measurement is the effect of desorption during the experiments. Freezing of raindrops does not initiate instantaneously. A period of thermal stabilization and supercooling exists before the initiation of freezing, and there could potentially be a loss of dissolved solute mass due to desorption and evaporation. These changes in the liquid phase concentration are addressed via a desorption factor. For quantification, the desorption factor is calculated as the mass concentration of the supercooled drop immediately before freezing to the mass concentration of the initial liquid phase concentration. More experiment specific details in calculating retention coefficient and desorption for the present study are provided in Chapter 5.

3.3.2 Retention indicator

Another way of characterizing retention of chemical species is through the parameter retention indicator - RI. As suggested by Stuart and Jacobson (2003), the parameters influencing chemical retention can be understood via a timescale analysis of the entire process. RI is the ratio of solute expulsion time τ_{exp} to the total freezing time τ_{frz}. The solute expulsion time can be expressed as the sum of aqueous phase mass expulsion time τ_{aq}, gaseous phase mass expulsion τ_g, and interfacial solute mass expulsion τ_i. Another component of expulsion time scale introduced by Jost et al. (2017) is the aqueous phase reaction timescale (τ_r). Collectively, the total expulsion time can be calculated as

$$\tau_{exp} = \tau_g + \tau_{aq} + \tau_i + \tau_r \tag{3.10}$$

τ_g is the characteristic time required for gas-phase mass transfer of a solute for a spherical particle (Pruppacher and Klett, 2010; Stuart and Jacobson, 2003). The gaseous expulsion time τ_g is obtained from the equation

$$\tau_g = \frac{a^2 H^*}{3 D_g f} \tag{3.11}$$

τ_g depends on the radius of the drop a, H^*, gaseous diffusivity D_g and the ventilation around the drop f. In the expression for τ_g, the variable a has to be considered carefully. Jost et al. (2017) in their updated RI formulation used the drop spreading height in place of the drop radius. A μm-sized cloud droplet upon collision with a larger hydrometeor was visualized to spread in a cylindrical manner, a spread height was used instead of the drop radius (Jost et al., 2017). For a standalone raindrop, this spread factor was not applicable and was replaced with the drop radius. Ventilation coefficient $f = 5.6$ for a 2 mm raindrop in an acoustic levitator setup (Szakáll et al., 2021), was used in Eq. 3.11.

The aqueous expulsion time τ_{aq} is computed from the characteristic time for aqueous-phase mass transport time for a spherical drop (Schwartz, 1986; Jost et al., 2017), as

$$\tau_{aq} = \frac{a^2}{D_{aq}} \tag{3.12}$$

where D_{aq} is the aqueous diffusivity of the chemical species. Similar to τ_g, drop spreading height is replaced with drop radius a, in Eq. 3.12

The interfacial mass transport time is calculated from the liquid to gas interfacial mass transport time for a spherical drop (Stuart and Jacobson, 2003; Seinfeld and Pandis, 2016), as

$$\tau_i = \frac{4 a H^*}{3 v \alpha} \tag{3.13}$$

where v is the thermal velocity of the chemical in air and α is the mass accommodation coefficient. α is the probability of uptake of gaseous chemical substances on condensed surfaces, such as water, aerosols (Davidovits et al., 2006).

The aqueous phase reaction time scale τ_r was introduced to take into account the aqueous phase interactions of dissolved solutes with CO_2. The retention coefficient measurements for formaldehyde and ammonia were affected due to their interaction with atmospheric CO_2 (Jost et al., 2017). For instance, in their measurements with NH_3, the cloud droplets were reported to absorb CO_2, until they reached the rime collector. For other substances, however, this time scale was very minimal (Jost et al., 2017). The substances investigated for their chemical retention during freezing of raindrops in this study, this timescale τ_r was neglected, as acid-base neutralization reactions are much faster than such aqueous phase reactions (Stuart and Jacobson, 2003, 2004).

The freezing time scale τ_{frz} is computed as the sum of diabatic and adiabatic freezing, and given as

$$\tau_{frz} = \tau_{ad} + \tau_d \tag{3.14}$$

Combining Eq. 3.10 and Eq. 3.14, the retention indicator can be calculated as

$$RI = \frac{\tau_{exp}}{\tau_{frz}} = \frac{\tau_g + \tau_{aq} + \tau_i + \tau_r}{\tau_{ad} + \tau_d} \tag{3.15}$$

From their timescale analysis, Stuart and Jacobson (2004) provided an exponential fit relating RI and experimentally reported R as

$$R = 1 - exp(-kRI) \tag{3.16}$$

where k (= 0.002) was a fit parameter for the calculated RI values (Stuart and Jacobson, 2004) and experimentally obtained R values. Jost et al. (2017) suggested that there is rather a smoother transition for such a relation between RI and R, which can be represented through a sigmoidal relationship of the form

$$R = \left[1 + \left(\frac{a1}{RI}\right)^{b1}\right]^{-1} \tag{3.17}$$

From their observed dependency of H^* on experimentally derived R, Jost et al. (2017) also present such a sigmoidal relationship for H^* and R, as

$$R = \left[1 + \left(\frac{a2}{H^*}\right)^{b2}\right]^{-1} \tag{3.18}$$

The $a1$, $b1$, $a2$, and $b2$ are sigmoidal fit parameters.

3.4 The acoustic levitator setup - overview

The Mainz Acoustic Levitator (M-AL) setup (Diehl et al., 2014; Szakáll et al., 2021) used for implementing a contact free immersion mode of freezing is shown in Fig. 3.2. The central components of this setup are an ultrasonic wave transmitter (max. frequency of 58 kHz) and a metal reflector plate. Due to the reflector plate, a standing wave is generated. The nodes of the standing wave served as the optimal position for levitating the raindrops. A video camera is placed on the left side of the setup. The details of the video camera(s) used for each specific set of experiments are provided in the corresponding chapters. The drop surface temperature was measured via an infrared thermometer (KT 19.82 II, Heitronics). The infrared thermometer records the radiation from a source and translates it to an equivalent temperature reading. The levitator setup was used inside a Plexiglass housing for shielding from any external ambient air disturbances during the experiments. Additionally, a platinum resistor thermometer Pt100 was placed in the vicinity of the levitated drop to monitor the

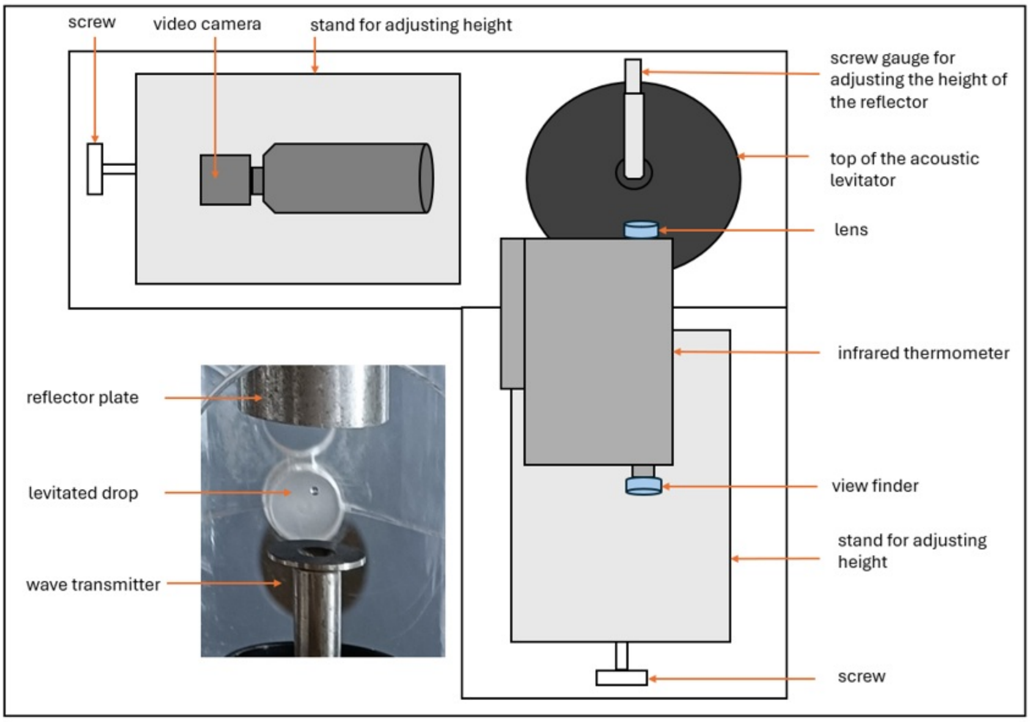

Figure 3.2: A schematic of the Mainz Acoustic Levitator (M-AL) setup used for immersion freezing.

air temperature inside the Plexiglass housing.

The Pt100 sensor was also used to calibrate the infrared thermometer, and implemented in an existing data acquisition via LabVIEW software application. At different temperatures of the cold room, the temperatures measured by the Pt100 sensor and the infrared thermometer were recorded and plotted against each other. The Pt100 was used as a reference for this calibration. Further details of calibration can be found in Mayer (2016). Besides the calibration for data acquisition, another method was used for checking the calibration of the infrared camera after prolonged measurements. The Pt100 was placed in an ice-water mixture inside a spoon, where the temperature stays at the thermal equilibrium temperature of 0 °C, until the liquid portion completely freezes. Simultaneous recordings of the slush mixture were taken from the infrared thermometer, at a distance similar to that of the experimental distance between a levitated drop and the infrared thermometer (about 3 cm apart). Any offset produced during these checks was then corrected in the data acquisition interface. An important aspect to take into consideration while calibrating is that background surfaces (air or the spoon) should not be in the field of view of the infrared thermometer. Otherwise, they might create a bias in the reflectivity measured by the infrared thermometer. For experiments below -15°C, a +5 V DC heating pad was connected to the infrared thermometer, to maintain the accuracy of internal components of the thermometer within its operational temperature limit of -15°C.

Further, the cameras and other electronics were placed inside insulation boxes for maintaining steady operation at cold temperatures. An additional insulation box for the ultrasonic wave generator was made from 30 mm Armaflex sheets, which improved the stability and reproducibility of the setup substantially, especially for experiments performed at ambient temperatures lower than -15°C. The setup was cleaned thoroughly with deionized water and dried in between each set of measurements, especially for retention measurements, where many different chemicals were used. Aqueous solutions with suspended INPs were prepared from distilled and deionized water. These solutions were then transferred to a syringe with a flat tip needle for ejecting spherical drops for levitation. The syringe was kept in a hot water bath to prevent freezing inside the cold room. Prior to any measurements, 5-10 drops generated from the purified water and without any INPs were levitated for about 100 s. Szakáll et al. (2021) show that a small background frozen fraction spectra from pure water can still exist, possibly from particles with ice nucleating ability, already existing in the purified water. Such background spectra were more prominent at drop freezing temperatures lower than -21°C ($\sim$ 253K) and need to be carefully considered. However, drops with pure water, without any INPs, did not undergo freezing at ambient temperatures warmer than -28 °C, as expected (Pruppacher and Klett, 2010). This indicates that the probability of freezing with pure water was almost negligible. Details regarding the immersion freezing experiments and their results are shown and discussed in the following Chapter.

Chapter 4

Immersion freezing of raindrops

The central mechanism for investigating the freezing of raindrops in this study revolves around immersion freezing. The majority of the freezing studies were performed with AgI as INP, and its general freezing characteristics are discussed in Sec. 4.1. The hexagonal crystal lattice structure of AgI complements well with the hexagonal lattice structure of ice. As such, AgI as an INP has been widely used in cloud glaciation and cloud seeding processes due to its high ice nucleating efficiency (Marcolli et al., 2016). Further freezing experiments with montmorillonite (MMT) and metal-doped montmorillonite samples were performed to investigate how the incorporation of readily available metallic elements in the atmosphere with INPs could affect their ice nucleating behavior. These findings are discussed in Sec. 4.2.

4.1 Silver iodide

4.1.1 Frozen fraction

Silver iodide was used as an INP in aqueous solutions to freeze the levitated drops with the M-AL setup. Characterizing AgI involved performing freezing experiments at different INP concentrations at different ambient temperatures. The AgI concentrations were 0.2, 0.01, and 0.0003 g/L, at ambient cold room temperatures -15, -20, and -28°C, respectively. About 50 drops were frozen at each of the three different temperatures. Levitated drops that did not freeze after entering the supercooling state for more than 60 seconds were counted as unfrozen drops. The drop surface temperature was measured with the infrared thermometer as discussed in the Sec. 3.4. The average of three consecutive temperature recordings just before the initiation of nucleation (adiabatic freezing stage) was considered as the drop freezing temperature. The 50 frozen drops at each temperature were grouped in temperature bins of ± 0.5 K. A cumulative distribution was obtained from the grouped data. The plot of this cumulative distribution against drop freezing temperature shows the frozen fraction (f_{ice}) at different ambient temperatures, shown in Fig. 4.1. For each ambient temperature, the frozen fraction of 0.5 is used to determine the median drop freezing temperature. The average size of the levitated drops was 2.01±0.10 mm in diameter.

The average drop sizes for these freezing experiments were 2.0 ± 0.1 mm. The median drop freezing temperatures at 50% frozen fraction from Fig. 4.1 for different INP concentrations are summarized in Table 4.1. The median freezing temperatures were found to be at 269.25, 266.45, and 264.25 K (or -3.9, -6.7, and -8.9 °C, respectively).

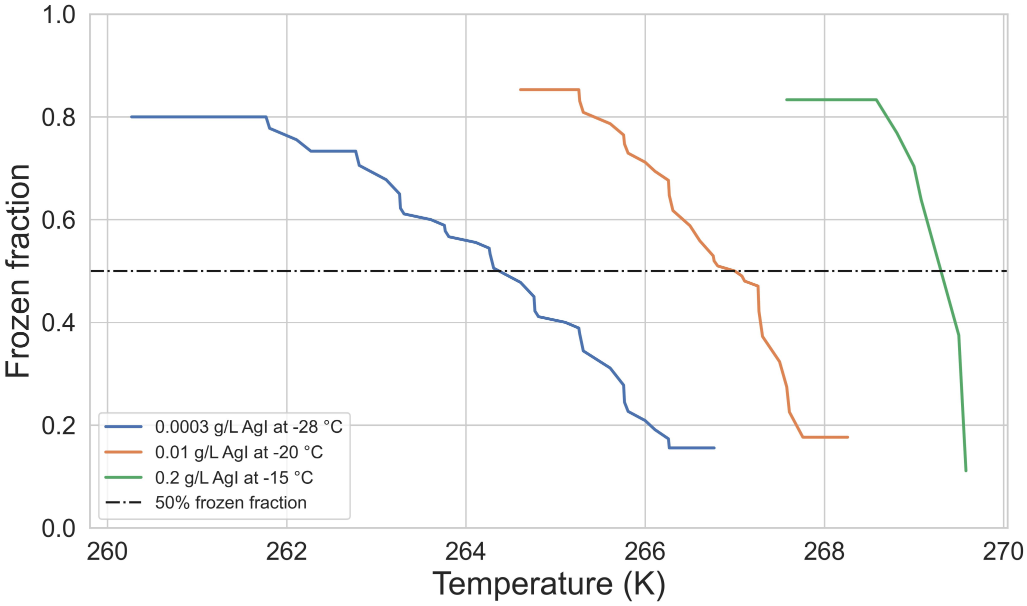

Figure 4.1: Frozen fraction as function of drop freezing temperature for different concentrations of AgI. Blue, orange, and green lines representing experiments performed at -28, -20, and -15 °C ambient temperatures.

Table 4.1: Results of experiments with different INPs and concentrations.

AgI concentration (g/L)	Ambient temperature	Median drop freezing temperature
0.2	258.15 K (-15 °C)	269.25 K (-3.9 °C)
0.01	253.15 K (-20 °C)	266.45 K (-6.7 °C)
0.0003	245.15 K (-28 °C)	264.25 K (-8.9 °C)

4.1.2 INAS density

The ice nucleation efficiency of AgI is shown and discussed in terms of ice nucleation active site density n_s(T). This can also be interpreted as the cumulative number density of active sites that become active between 0°C and any temperature T. From f_{ice} values, n_s(T) was calculated using Eq. 3.7. For n_s(T) calculations, f_{ice} values below 10% and above 90% were neglected. The specific surface area (SSA) for AgI was assumed to be 13 m^2/g after inferring the experimental results from Koopal (1978). A plot of the n_s(T) is shown in Fig. 4.2.

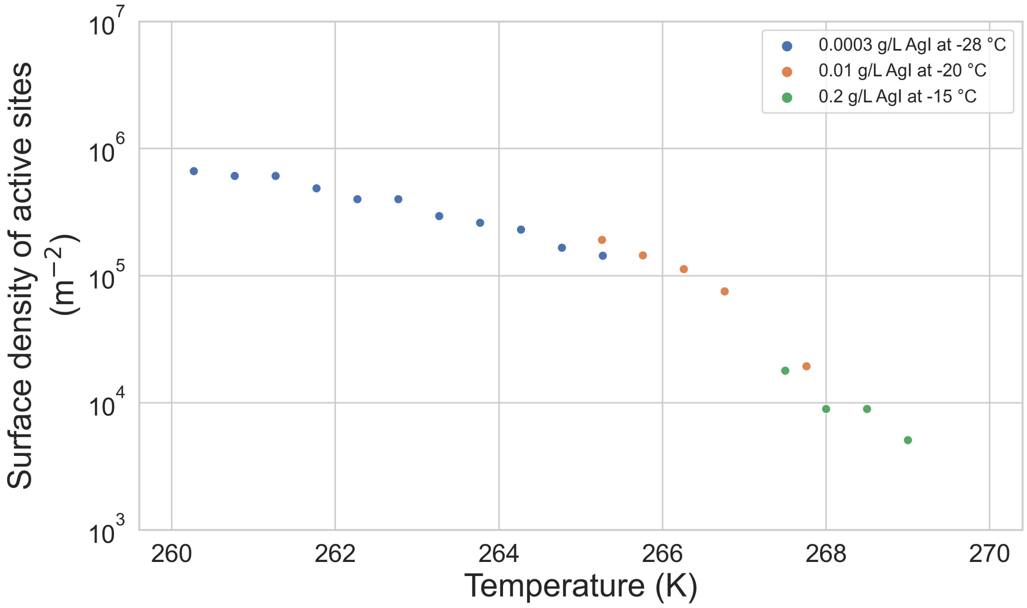

Figure 4.2: The variation of the surface density of active ice nucleating sites with temperature for different concentrations of AgI. Blue, orange, and green dots representing experiments performed at -28, -20, and -15 °C ambient temperatures.

From Fig. 4.2, the n_s(T) values were observed to vary around 3 orders of magnitude in the experimental temperature interval of 260-269 K. Szakáll et al. (2021) found that feldspar was the most efficient INP among their reported substances. For feldspar, the n_s(T) values of 10^5 were found to be around 257 K (in their Fig. A6(a)). For AgI in this present study, the n_s(T) values of 10^5 were around 267 K. At values around 267 K, feldspar has barely any active ice nucleating sites available. Therefore, it was used as the preferred INP in the majority of experimental studies.

4.2 Cation doped montmorillonite

These experiments were also performed with the M-AL setup, placed inside the cold room facility of the wind tunnel laboratory, to study the ice nucleating activity of altered MMT particles. The doped MMT samples were prepared at the Weizmann Institute, Israel, and brought over for conducting freezing experiments. MMT is a commonly found mineral dust in the atmosphere and has been widely used in immersion freezing experiments (Kanji et al., 2017). The weakly bound layered aluminosilicate structure of natural MMT particles results in a charge imbalance between the layers, which provides a basis for frequent substitutions of cations such as $\mathrm{Mg_2}^+$, $\mathrm{Al_3}^+$ between the layers (Murray et al., 2012). And the charge imbalance is counter balanced by cations such as $\mathrm{Ca_2}^+$ or Na^+. This behavior of MMT particles facilitated the investigation of the freezing characteristics of doped MMT samples, where such ion exchanges could occur within natural clouds.

Doped MMT samples were prepared by ionic substitutions with commercially available MMT-Swy2 (Sodium - Wyoming montmorillonite clay) in the powdered form, which predominantly consists of Na^+ cations. Swy-2 MMT was purified by a set of centrifugation cycles to remove larger feldspar particles, which could compete with ice nucleating activity. This purified MMT sample is named D2 PMT (purified montmorillonite). Further samples were prepared via ion-exchange with:

1. monovalent cations: Li and Cs, using LiCl and CsCl
2. divalent cation: Ca using $CaCl_2$
3. trivalent cation: Al using $AlCl_3$

The samples were washed with MiliQ water to remove any Cl^- residues, dried in an oven at 70 °C for 24 h, and afterwards grinded using a mortar and pestle. Freezing experiments with all the samples were performed at cold room temperatures of -23±1.5 °C. Due to operational limitations of the walk-in cold room, experiments at temperatures lower than -23±1.5 °C could not be performed at that time. The average diameter of the levitated drops was 2.01±0.11 mm.

4.2.1 Frozen fraction

The frozen fractions were obtained in a similar manner as for AgI. About 50 frozen drops were grouped in temperature bins of ±0.5 K. The cumulative distribution of the grouped frozen drops is shown in Fig. 4.3. The results of freezing experiments with the doped MMT samples are summarized in Table 4.2.

Table 4.2: Results of freezing experiments with different MMT samples

Sanmple name	Concentration (g/L)	Median drop freezing temperature
D2-PMT	0.1	260.35 K (-12.8 °C)
Li-PMT	0.1	258.65 K (-14.5 °C)
Cs-PMT	0.17	257.65 K (-15.5 °C)
Ca-PMT	0.1	257.05 K (-16.1 °C)
Al-PMT	0.2	259.75 K (-13.4 °C)

In Fig. 4.3, none of the substances had frozen fraction above 0.7, i.e., at least 30% of the levitated drops did not freeze during the experiments. In particular, Cs-PMT and Al-PMT showed a large proportion of drops in the unfrozen state at a concentration of 0.1 g/L. Concentrations of Cs-PMT and Al-PMT were subsequently increased to 0.17 g/L and 0.2 g/L so that at least 50% of levitated drops would freeze within our experimental constraints.

Nevertheless, a slight decrease in the median drop freezing temperatures can be seen for the cation doped samples as compared to purified D2-PMT samples.

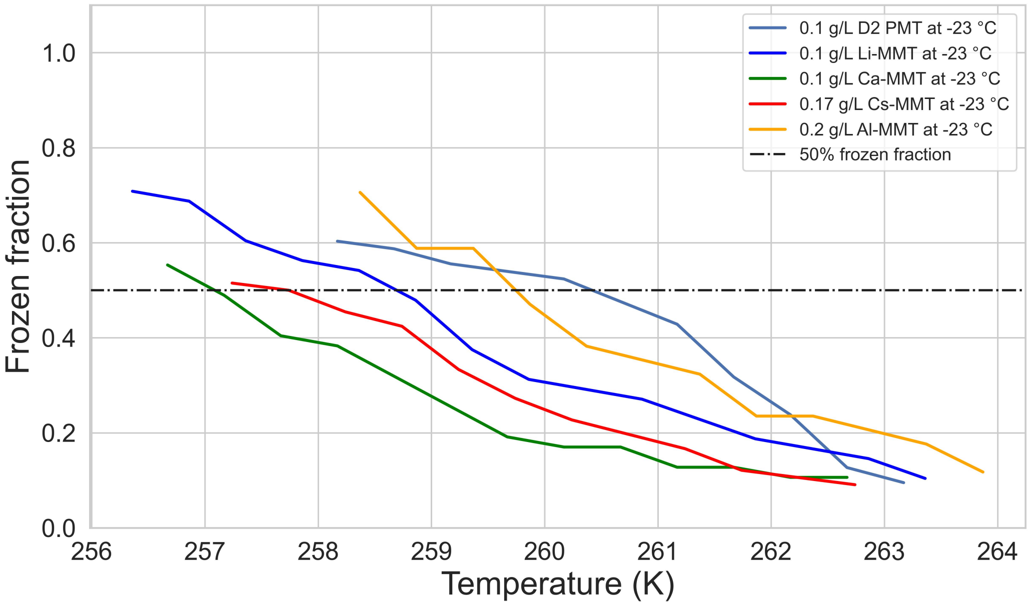

Figure 4.3: The variation of frozen fraction with drop freezing temperature for different samples of MMT. Blue, green, red, and yellow lines represent MMT samples doped with Lithium, Calcium, Cesium, and Aluminum, respectively. Light blue line representing frozen fractions of the D2-PMT sample.

4.2.2 INAS density

The INAS densities were calculated using Eq. 3.7 for n_s(T) as with AgI. Several immersion freezing studies were done with MMT as INP in an aqueous suspension (Hoose and Möhler, 2012). Pitter and Pruppacher (1973) reported experimentally derived median drop freezing temperatures of -19 °C and -24 °C for drop radii of 350 and 50 μm respectively. In their numerical simulations of freezing drops Diehl et al. (2006) mentioned that the drop size and the median freezing temperature vary inversely. In our experiments, the average drop radius was about 1000 μm for the MMT samples, and seems to follow the inverse size and median drop freezing temperatures relation accurately. Diehl et al. (2014) also performed immersion freezing experiments with MMT-K10 as INP, and with the same setup, where they reported a median drop freezing temperature of -20 °C for 1000 μm drop radius. The specific surface area for MMT-K10 was about 220 m^2/g. The D2-PMT samples used in the current experiments were found to have a specific surface area of 31.8 m^2/g, which is an order of magnitude lower than the MMT-K10 powder. The structural composition and the surface area of the INP play a significant role in the median freezing temperatures, and these differences could be attributed to the differences in composition of MMT samples as compared to Diehl et al. (2014).

The n_s(T) of MMT as a function of temperature is shown in Fig. 4.4. Also, INAS data from freezing experiments with D2-PMT samples performed at Weizmann Institute using a microfluidic assay (Reicher et al., 2018) are plotted. The drop radii for experiments with the microfluidic assay were 50 μm. Due to smaller drop sizes, the freezing temperatures were quite low compared to our measurements. However, a similar slope for n_s(T) can be seen for both data sets (black and blue dots in Fig. 4.4).

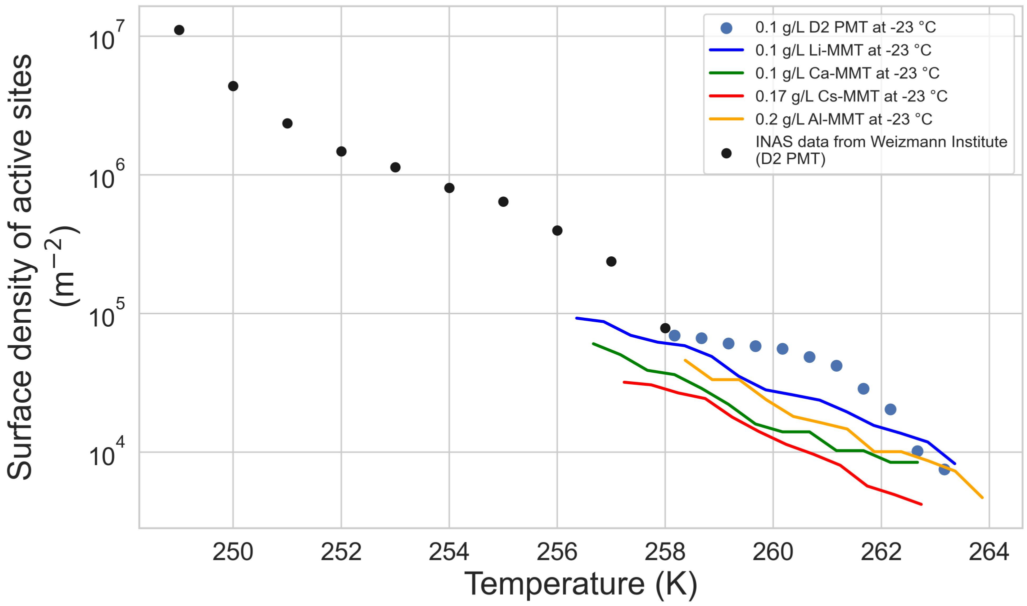

Figure 4.4: The variation of the surface density of active ice nucleating sites with temperature for the different MMT samples. Blue, green, red, and yellow lines represent MMT samples doped with Lithium, Calcium, Cesium, and Aluminum, respectively, investigated with the M-AL setup. Coloured dots represent D2-PMT samples investigated with the M-AL setup (blue) and with microfluidic assay (black). For experiments with microfluidic assay, the drop sizes were 100 μm in diameter. For all other experiments with the M-AL setup, the drop sizes were about 2 mm

4.3 Implications

These experiments served as a prerequisite for understanding the range and variation of drop freezing temperatures at different INP concentrations and cold room temperatures. The characterization of AgI was used in Chapter 5 during the experiments for measuring retention coefficients and in Chapter 6 while investigating fast dynamics of freezing raindrops. AgI was found to be a very stable INP throughout the specific ranges of temperature and concentrations. For raindrop sizes, cation doped montmorillonite tended to lower the drop freezing temperatures as compared to purified montmorillonite INP, i.e., the ice nucleating ability worsened for the doped MMT samples.

Chapter 5

Retention during freezing of raindrops

This chapter has been published in the peer-reviewed journal, Atmospheric Chemistry and Physics. The full citation:

"**Gautam, M.**, Theis, A., Seymore, J., Hey, M., Borrmann, S., Diehl, K., Mitra, S. K., and Szakáll, M.: Retention during freezing of raindrops – Part 1: Investigation of single and binary mixtures of nitric, formic, and acetic acids and 2-nitrophenol, Atmos. Chem. Phys., 25, 11813–11828, https://doi.org/10.5194/acp-25-11813-2025, 2025."

Abstract: The influence of freezing processes and vertical transport of trace gases into the upper atmosphere during deep convection is critical to understanding the distribution of aerosol precursors and their climate effects. We conducted experimental studies inside a walk-in cold room for freely levitating rain drops (drop diameter: 2 mm) using an acoustic levitator apparatus. We investigated the effect of freezing raindrops on the retention of organic species for the first time with silver iodide as the ice nucleating agent. Quantitative chemical analysis determined the retention coefficient, which is defined as the fraction of a chemical species remaining in the ice phase compared to their initial liquid phase concentrations. We measured the retention coefficients of nitric acid, formic acid, acetic acid, and 2-nitrophenol as single components. Furthermore, we determined the retention coefficients of these substances as binary mixtures. Our results show the dominance of physical aspects such as drop size and ice-shell formation over their chemical counterparts on overall retention for the investigated large drops. Thus, for rain sized drops almost everything is fully retained during the freezing process i.e., retention coefficients close to 1, even for species with low effective Henry's law constants, $H^* < 10^{-4}$. An ice-shell is formed within 4.8 ms around the drops just after the freezing was initiated. This ice-shell formation was found to be the controlling factor for the overall retention of the investigated species, which inhibited any further expulsion of dissolved substances from the drop.

5.1 Introduction

The Earth's atmosphere consists of a diverse range of chemical constituents, starting from ever present gases such as nitrogen, oxygen, carbon-dioxide, ozone, etc., to a wide range of chemicals in trace amounts as well. Biogenic and anthropogenic source contributors are known to be important for understanding the role that trace constituents have on the atmosphere over long timescales (Kolb et al., 2010; Andreae, 2019). However, vertical redistribution can be just as critical (Martini et al., 2011; Ervens, 2015; Wang et al., 2016). During convective transport, there is a rapid redistribution of trace gases and aerosols from the boundary layer and troposphere, that can alter the overall concentration of the chemical constituents (Warneck, 1999; Corti et al., 2008; Ervens, 2015).

Organic aerosol mass is usually underestimated in the boundary layer and beyond (Carlton et al., 2009; Hodzic et al., 2020). As a consequence, the potential impact of aerosols on the global radiation budget, radiative forcing, and overall climate can be misrepresented (Lohmann and Feichter, 2005; Tsigaridis et al., 2014; Shrivastava et al., 2017; Sporre et al., 2020). Williamson et al. (2019) also reported that there is an under-representation of total organic mass due to low estimations for new particle formation, particularly in tropical convective regions.

During vertical transport in deep convective systems, there is phase change of the water droplets as they undergo cooling and subsequent freezing at lower temperature regimes higher up in the atmosphere. Trace gases dissolved in these droplets could be either retained, revolatized, or scavenged during the freezing process (Pruppacher and Klett, 2010). The fraction of chemical species remaining inside the frozen hydrometeor, compared to their initial concentration in liquid phase before freezing, results in the so-called retention coefficient. Substances that are completely retained after freezing will have a retention coefficient of 1. Modeling studies concerning convective transport and redistribution of trace gases have stressed on the importance of experimentally determined retention coefficients (Mari et al., 2000; Barth et al., 2001, 2007; Tost et al., 2010; Long et al., 2010; Bela et al., 2016; Cuchiara et al., 2020; Ryu and Min, 2022; Cuchiara et al., 2023). However, such experimental databases are quite few in this regard.

Previous studies on experimentally determining retention coefficients in the context of riming of supercooled droplets of single substances help bridge the uncertainty gap and provide a backbone for effective parameterization for modeling frameworks (Iribarne et al., 1983; Lamb and Blumenstein, 1987; Iribarne et al., 1990; Snider et al., 1992; Snider and Huang, 1998; von Blohn et al., 2011, 2013; Jost et al., 2017; Borchers et al., 2024). The term "riming-retention" will be used to refer to these above mentioned studies collectively. The following substances were studied for retention during riming of supercooled droplets: SO_2, H_2O_2, O_2, HNO_3, HCl, NH_4, formic acid, acetic acid, malonic acid, oxalic acid, formaldehyde, α-pinene oxidation derivatives and nitro- aromatic compounds. These experimental studies revealed dependencies of the retention of trace gases on both chemical and physical properties. There is established correlation with effective Henry's law coefficient (H^*)

and a retention indicator (RI) parameter, which relates experimentally derived retention coefficients to model derived values (Stuart and Jacobson, 2003, 2004). H^* shows the dependence on the solubility and dissociative properties of trace gases, whereas RI provides a ratio of expulsion timescales to freezing timescales. A freezing time significantly lower than the solute expulsion time would result in a chemical substance being retained. These expulsion timescales are described in Schwartz (1986), that take into account the aqueous, interfacial, and gaseous mass transfer rates and the aqueous phase kinetics as explained in Jost et al. (2017). In addition to these chemical properties, physical properties such as drop size, ventilation around the drop, temperature, and liquid water content are the major contributing factors affecting retention (Jost et al., 2017; Jost, 2017). All the above mentioned experimental studies concerning riming-retention were mostly related with cloud droplets (i.e. diameters in the μm size range), for which the chemical properties were determined to be the dominant factors. The present study focuses on large rain drops (diameters in the mm size range), which have not been experimentally investigated thus far. A significant difference from a physical perspective in terms of retention of trace gases for cloud droplets and rain drops is the freezing mechanism. For riming experiments involving cloud droplets freezing is initiated upon contact with a frozen substrate, whereas, for rain drops investigated in this present study, immersion freezing was the main mechanism. The geometry of the droplets upon contact also changes leading to spreading of the droplets under ventilated conditions in the riming-retention experiments. This change in geometry influences the heat transfer into the ice as it freezes(Jost et al., 2017). Moreover, the surface to volume ratio for cloud droplets is about 3 orders of magnitude higher as compared to rain drops. This higher surface to volume ratio facilitates faster mass expulsion time for cloud droplets. Freezing of raindrops is especially important for the case of convective clouds with warm bases where collision and coalescence can produce such large mm sized drops, which can be further transported into the upper troposphere during deep convection. Henceforth, the term "freezing-retention" will be used to refer to the present study, investigating retention during freezing of rain drops.

The motivation for this study was to investigate and understand the retention of chemical species dissolved in larger drops, and thereby augment experimental databases to further enhance modeling frameworks. To visualize our experimental outlook, we selected four chemical substances namely: 2-nitrophenol, acetic acid, formic acid, and nitric acid, with increasing H^* values of 3.50×10^3, 1.28×10^5, 8.31×10^5 and 7.56×10^{11}, respectively, at 0 °C and pH about 4, for all. These substances are commonly found in the atmosphere and their previously measured retention coefficient values in riming cloud droplets lie between 0 to 1 and scale with H^*. In addition to investigating these four substances as single components, we also studied their potential interactions as binary mixtures. Binary mixtures were studied to improve understanding of the retention process as in how the differential incorporation or segregation of two substances during freezing might affect their overall retention.

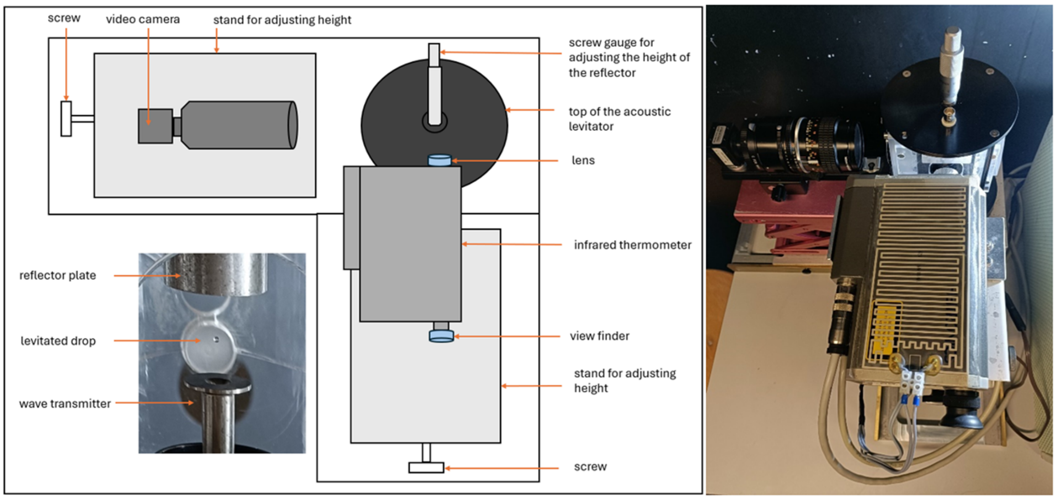

Figure 5.1: The Mainz Acoustic Levitator (M-AL) setup. Left: A schematic of the setup. Right: Setup in-situ.

5.2 Methods

5.2.1 Experimental Setup

In this study, we used the Mainz-Acoustic Levitator (M-AL) setup (Fig. 5.1), placed inside a walk-in cold room. M-AL employs an ultrasonic wave source (58 KHz) and a metal reflector to produce a standing wave. Water drops can be injected with a syringe and levitated contact-free at the intersection of the incident and reflected waves (i.e. at the nodes of the standing wave). The diameters of the levitated water drops used in this study were 2.0 ± 0.1 mm. The M-AL is enclosed inside a Plexiglas housing to minimize any external interference to the standing wave. More details about the M-AL can be found in Diehl et al. (2014) and Szakáll et al. (2021).

In addition to the ultrasonic source, an infrared thermometer (KT 19.82 II, Heitronics) was used to measure the surface temperature of the levitated drops, and a USB camera (USB-103H, Phytec GmbH, Germany) to record the drop size information. The top left section of the schematic (Fig. 5.1) shows the placement of the video camera, which had a wide video graphics array of 752 × 480 pixels and a minimum pixel size of 6×6 μm. The infrared thermometer can be seen at the bottom right section of the schematic. A small heating element was incorporated into the infrared thermometer to maintain its internal components when it was operated at temperatures lower than -15 °C. Both the video camera and the infrared thermometer were placed on adjustable stands, which allowed vertical and horizontal adjustments. In addition to the infrared thermometer, another temperature sensor (PT-100) was placed inside the Plexiglas housing to monitor the thermal stability of the setup during experiments.

The retention experiments were carried out inside the walk-in cold room of the laboratory at temperatures between -15 and -28 °C. Silver iodide (AgI; Sigma Aldrich-99%) was used as the ice nucleating particle (INP) to initiate the freezing process. We first characterized the INP at three different concentrations (0.2, 0.01, and 0.0003 g/L) at three different cold room temperatures (-15, -20, and -28 °C). This provided the freezing curves of silver iodide at various temperatures and concentrations (Fig. A.2); more details can be found in Appendix A.1.1. These steps were a pre-requisite for retention experiments to infer the correct drop freezing temperature ranges during our measurements.

5.2.2 Sampling procedure

In total, the retention of 4 single components and 3 binary mixtures were investigated. Nitric acid, formic acid, acetic acid, and 2-nitrophenol were measured as single components. Two sets of combinations were studied for the binary mixture of a strong and a weak acid, namely: nitric acid and acetic acid (mixture A1) as well as nitric acid and formic acid (mixture A2). Another set of binary mixtures was the combination of a small and a large molecule, due to their differences in molecular size and mobility. Here we investigated the mixture of formic acid and 2-nitrophenol (mixture B). The substances along with their purity labels are listed in Table 5.1.

Table 5.1: Substances and mixtures investigated in this study.

Substance	Label/purity	Tracer	Concentration (mg/L)
Single components			
Nitric acid	Merck (65% w/w)	Sulphate$^+$	20
Acetic acid	Riedel-de Haen (100%)	Nitrate *	20
Formic acid	Emsure (98-100%)	Nitrate *	20
2-nitrophenol	Thermo Scientific (99%)	2-nitrobenzoic acid**	20
Binary mixtures			
A1. Nitric acid and Acetic acid	– –	Sulphate$^+$	20
A2. Nitric acid and Formic acid	– –	Sulphate$^+$	20
B. Formic acid and 2-nitrophenol	– –	Nitrate* and 2-nitrobenzoic acid**	20

Tracers: $^+$ Sulphate standard (SO_4): TraceCERT (99%), * Nitrate standard (NO_3): TraceCERT (99%), **2-nitrobenzoic acid: Thermo Scientific (95%)
Hydrochloric acid (HCl): Roth (37% w/w) and Sodium Hydroxide (NaOH): Merck (99%) were used to adjust the pH in the sensitivity studies.
The label/purity of the substances in binary mixtures are same as that of the single components.

Aqueous solutions of the investigated substances were prepared at an initial concentration of about 20 mg/L. Typical mixing ratio of dissolved gases in the atmosphere lies in the range of ppb to tens of ppm (on mass basis). This higher concentration of 20 mg/L helped us maintain proper detection levels during our quantitative analysis. A high initial concentration of 20 mg/L would also imply that the internal partial pressure of any dissolved substances were high enough to overcome the internal resistances inside the liquid drop. Higher concentrations used in our experiments served as the upper limit for minimum possible retention of the dissolved substances. Additionally, high solute concentration could decrease the freezing rate (Pruppacher, 1967). For 20 mg/L, the effect of dissolved substances influencing the freezing process could be considered negligible as compared to pure water. In terms of molar concentration, 20 mg/L corresponds to 4.34 $\times 10^{-4}$ moles/L for formic acid - which has the lowest molar mass among the investigated species - is about 2 orders of magnitude lower to significantly affect the freezing process (Pruppacher, 1967).

The prepared solutions were transferred to a syringe for injecting a single drop inside the M-AL. For each experiment 11 measurement points were recorded. Each measurement point consisted of a total of 10 frozen drops collected in a vial. The volume of one frozen drop was approximately 4.2 μL which makes the total volume for one measurement point being about 42 μL. These frozen drops were diluted 10 times in order to increase the injection volume for chemical analysis and filtered with a 2 μm pore size filter (Carl Roth GmbH).

Subsequent quantitative analysis was done using a DIONEX-ICS 1000 anion Ion Chromatography unit (IonPac AS9-HC column, 9 μm particle size, 4 × 250 mm dimension, Thermo Fisher Scientific Inc.) for nitric, formic and acetic acid. 2-nitrophenol and 2-nitrobenzoic acid were analysed with a high precision liquid chromatography (HPLC) unit (Hypersil GOLD column, 9 μm particle size, 150 × 2.1 mm dimension, Vanquish-Thermo Fisher Scientific Inc.).

For each of the investigated substances a concentration tracking tracer was added in order to track changes in mass concentration during the quantitative analyses. A tracer is a known chemical substance that is completely retained in ice, i.e. it has a retention coefficient of 1. The tracers used in this study were nitrate, sulphate, and 2-nitrobenzoic acid, which had a known retention of 1 from previous riming-retention studies (von Blohn et al., 2011; Borchers et al., 2024).

5.2.3 Calculation of retention coefficient

The retention during freezing was quantified by the retention coefficient R. It is the fraction of the chemical species that remains inside the frozen drops in the ice phase and the original solution in the liquid phase. The mathematical expression for calculating the initial retained fraction is given by

$$R_i = \frac{\frac{[substance]_{ice\ phase}}{[tracer]_{ice\ phase}}}{\frac{[substance]_{liquid\ phase}}{[tracer]_{liquid\ phase}}} \tag{5.1}$$

In Eq. 5.1, the square brackets indicate the concentration of the investigated chemical species and the tracers and R_i is the retention coefficient without any correction for desorption. The numerator is the ratio of ice phase concentration of the measured species with their specific tracer, whereas the denominator is the ratio of liquid phase concentrations.

Correction for desorption

The freezing of the levitated drops is not an instantaneous process when injected into the acoustic trap. The drop is initially at a temperature higher than 0 °C. It then undergoes gradual supercooling until the freezing is initiated (Fig. A.1). During this stage, starting from injection of the drop into the acoustic field of the levitator and its subsequent progression to the supercooling stage, the drop is exposed to external and internal forces until it is in equilibrium with its surroundings. Effects from the acoustic field potentially enhance ventilation while thermal stabilization can produce evaporation and desorption, leading to changes in aqueous concentration in the supercooled state. To account for all these effects, a correction parameter, called the desorption correction parameter D, was introduced as

$$D = \frac{\frac{[substance]_{supercooled\ phase}}{[tracer]_{supercooled\ phase}}}{\frac{[substance]_{liquid\ phase}}{[tracer]_{liquid\ phase}}} \tag{5.2}$$

To determine D, experiments were conducted under similar conditions as the retention experiments, with the exception of not adding any INP. In this case, the freezing process was not initiated and the liquid drop remained at a supercooled stage for a longer time. The drop was kept suspended for about 15 to 20 seconds, which is a typical time for the onset of freezing of the levitated drops under these experimental conditions (Fig. A.1). Afterwards, the supercooled drops were instantly frozen inside a liquid nitrogen bath, which has a temperature of about -197 °C (Scott, 1976; Jost et al., 2017). At such cold temperatures all substances inside the drops are retained during freezing. Quantitative analysis of these drops provided us with the concentration of the chemical substances in their supercooled stage and allowed the characterization of the desorption process.

The final retention coefficients R of the investigated chemical substances were calculated as

$$R = \frac{R_i}{D} \tag{5.3}$$

Colder temperatures essentially slows down the reaction kinetics for desorption to be effective (Mitra and Hannemann, 1993; Seinfeld and Pandis, 2016). For experimental temperatures below -15 °C, desorption would play a negligible role. We applied the desorption corrections measured at -15 °C for substances measured at lower temperatures as well. The experimental data for retention coefficients of the investigated species and their desorption can be accessed at Gautam and coauthors (2024).

5.2.4 Sensitivity studies

Retention experiments with the investigated substances were also carried out at different pHs and temperatures. pH sensitivity of the single components and the binary mixtures were studied at pH values of 3, 4, and 6/7. Hydrochloric acid (HCl) was used to lower the pH of the original solution and sodium hydroxide (NaOH) was used to increase the pH of the solution. The temperature sensitivity studies were performed at -3.9 ± 0.3 °C and -6.9 ± 1.1 °C drop freezing temperatures. These two different temperature ranges were evaluated from the temperature graph (more details in Appendix A.1.1). From the temperature profile obtained for experiments conducted at -15 °C cold room temperature and 0.2 g/L AgI, the median drop freezing temperature was found to be -3.9 ± 0.3 °C, under these experimental conditions (Fig. A.2). Similarly, retention experiments were conducted at -23 °C cold room temperatures and AgI concentration of 0.008 ± 0.001 g/L as the second experimental condition. The median drop freezing temperature for this second set of experimental conditions was obtained by extrapolating the temperature graph obtained at -20 °C cold room temperature and 0.1 unitg/L AgI (Fig A.2), as the drop surface temperature cooling rates at -20°C and -23°C were practically identical (0.4 °C/s). The median drop freezing temperature for -23°C cold room temperature, was found to be -6.9 ± 1.1 °C. The two temperature ranges were selected to compare the temperature sensitivity in earlier experiments concerning retention coefficients for cloud droplets (von Blohn et al., 2011, 2013; Jost et al., 2017; Borchers et al., 2024). The average size of the droplets was 21.5 ± 8.5 μm in the above mentioned studies involving riming-retention. In the present freezing-retention study with large levitated drops, the average drop sizes were 2.0 ± 0.1 mm.

5.3 Results and Discussions

5.3.1 Retention coefficient

The final retention coefficients for single components and binary mixtures are shown in Table 5.2. It can be seen that most of the substances measured as single components were completely retained in the ice phase. The exceptions were acetic acid and 2-nitrophenol, which were found to have retention coefficients of 0.88 and 0.90, respectively. However, for acetic acid as a single component, the standard deviation was much larger (± 0.12) compared to the other single component substances. Thus, acetic acid could also be completely retained during freezing. The standard deviation of 2-nitrophenol was smaller compared to acetic acid and it was the least retained substance (0.85 to 0.95) of investigated single components.

Brand (2014) studied the retention of formic, acetic, oxalic and malonic acids -— for large drops (2.67 mm and 7.25 mm spherical equivalent diameter) by freezing them on a Teflon coated pallet -— also reported high retention coefficients (close to 1). For example, for drop sizes of 2.67 mm (i.e. 10 μL drop volume), formic acid showed a retention coefficient of 0.94 ± 0.04. However, in our study contact-free immersion freezing was employed, representing a more realistic scenario to initiate freezing as compared to Brand (2014). Nevertheless, the measured retention coefficients in the present freezing-retention study and in Brand (2014) indicate near complete retention for the large rain sized drops.

Comparing our present results from freezing-retention experiments with previous riming-

Table 5.2: Retention coefficients at drop freezing temperature of -3.9 ± 0.3°C and pH values about 4 for all the investigated substances. The corresponding walk-in cold room temperature (ambient temperature) was -15 ± 1°C.

Substance	Retention coefficient (R)
Single components	
Nitric acid	1 ± 0.03
Acetic acid	0.88 ± 0.12
Formic acid	1.01 ± 0.08
2-nitrophenol	0.90 ± 0.05
Binary mixtures	
A. Mixture of a strong and a weak acid	
1. Nitric acid and Acetic acid	Nitric : 0.97 ± 0.06
	Acetic : 0.86 ± 0.15
2. Nitric acid and Formic acid	Nitric : 0.99 ± 0.05
	Formic : 0.99 ± 0.03
B. Mixture of a large and a small molecule	
Formic acid and 2-nitrophenol	Formic : 1 ± 0.07
	2-nitrophenol : 1.01 ± 0.09

retention studies (von Blohn et al., 2011, 2013; Jost et al., 2017; Borchers et al., 2024), one can observe a deviation from their findings. Retention coefficients measured for cloud droplets during riming-retention experiments show a sigmoidal dependency on the solubility and dissociative properties of the individual substances (i.e. their effective Henry's law constant H^*). Our present experiments do not reveal these observed dependencies for the large rain sized drops. For instance, 2-nitrophenol (as single component in Table 5.2) having the lowest H^* among the investigated substances, was highly retained inside a freezing raindrop indicated by a retention coefficient of 0.9. However in the case of riming-retention, 2-nitrophenol showed a retention coefficient of 0.12 at pH 4 and 0.27 at pH 5.6 (Borchers et al., 2024). Further discussion comparing the results from riming-retention of cloud droplets and freezing-retention of raindrops from this study is provided in Section 5.3.4.

In the binary mixture experiments, in which we combined a strong and a weak acid (A1 and A2 in Table 5.2), nitric acid was the stronger acid with a pKa value of -1.3 (Haynes, 2016). Acetic acid and formic acid, having pKa values of 4.76 and 3.77 respectively, were the weaker acids compared to nitric acid. The results shown in Table 5.2 indicate that binary mixtures do not seem to alter the retention coefficients of their individual species for the combination of a strong and a weak acid.

Mixture B had the combination of a small and a large compound. There the average retention coefficient of 2-nitrophenol in a mixture with formic acid was observed to have increased slightly as compared to its retention as a single component. As a binary mixture component, both 2-nitrophenol and formic acid are completely retained during freezing.

5.3.2 pH Sensitivity

Retention coefficients of the single components were each measured at three different pH values. As a strong acid, nitric acid completely dissociates and is therefore assumed to be

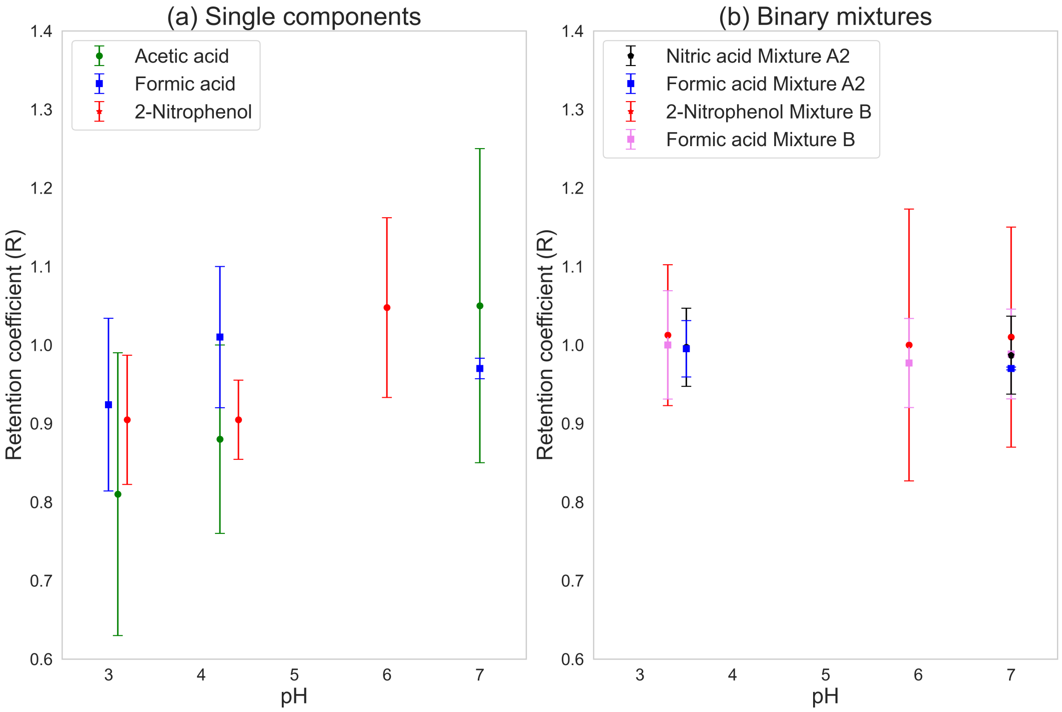

Figure 5.2: pH sensitivity of the retention coefficient of (a) single components, and (b) binary mixtures.

completely retained. Hence, sensitivity studies for nitric acid were not done. pH of the solutions was altered by adding HCl and NaOH. The pH sensitivity for the three single components- acetic acid, formic acid and 2-nitrophenol are shown in Fig. 5.2a.

Linear regression test (SPSS V23) reveals a significant statistical dependence of the retention of acetic acid (green marker) on pH, with $p = 0.047$. Acetic acid was not completely retained at pH 4.2 ($R = 0.88$), and an increase in retention was seen at higher pH. With increasing pH, the $H*$ also increases for acetic acid, (see Fig. A.4). The retention coefficients for acetic acid were 0.81, 0.88, and 1.05 for pH values of 3.1, 4.2, and 7.0, respectively, while their corresponding standard deviations were 0.18, 0.12, and 0.2.

Formic acid (blue marker) did not show any dependency on pH ($p = 0.182$). Formic acid is already completely retained at pH 4.1 ($R = 1.01$), and as such, any increase in pH would not lead to an enhancement of the retention, even though $H*$ for formic acid varies in a similar fashion to acetic acid (Fig. A.4)

2-nitrophenol (red marker) showed statistically significant dependence of retention on pH ($p = 0.005$), for our measured pH range. The retention coefficients of 2-nitrophenol at pHs of 3.2 and 4.4 and 6 were 0.90, 0.90 and 1.05, respectively, and their corresponding standard deviations were 0.08, 0.05 and 0.11. This result for 2-nitrophenol is contradictory to the expected form of dependence of $H*$ on pH, as in Fig. A.4. 2-nitrophenol is more dissociated at pH 6 than at pH 3.2 and 4.4. The fraction of deprotonated to protonated ions at pH 3.2, 4.4 and 6 for 2-nitrophenol was found to be 7×10^{-5}, 7×10^{-4} and 7×10^{-2}, respectively. This

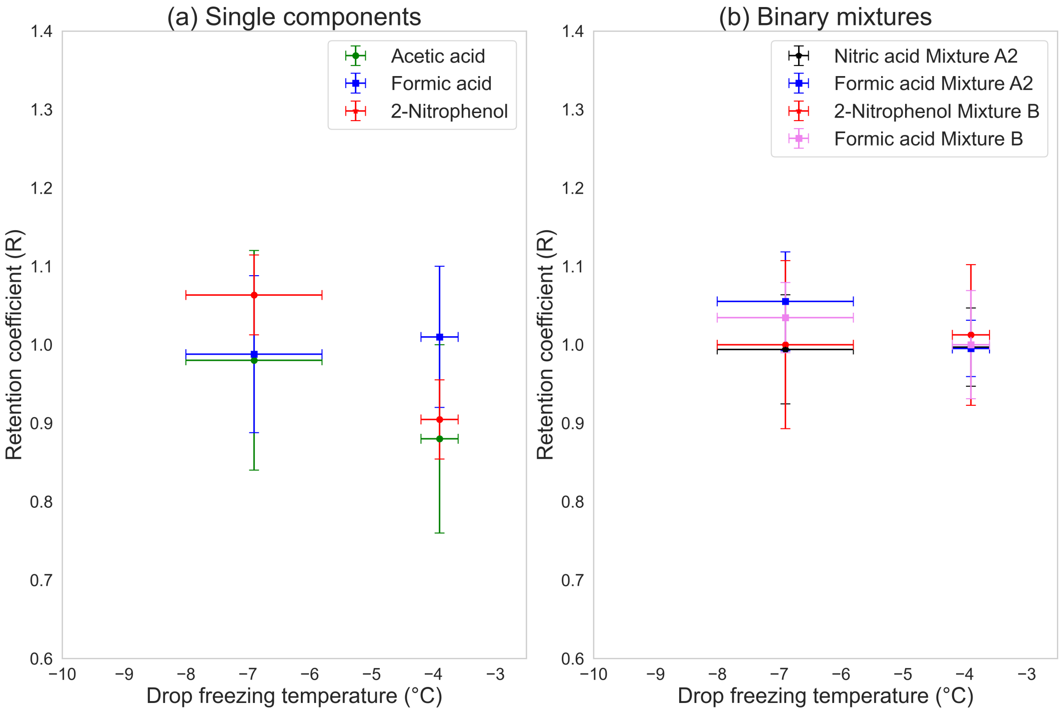

Figure 5.3: Temperature sensitivity of the retention coefficient of (a) single components, and (b) binary mixtures.

means that at pH 6, about 7% of 2-nitrophenol is present in deprotonated form. During the freezing process, deprotonated molecules must undergo protonation to achieve neutrality before they can be expelled from the drop. At pH 6, a higher proportion of molecules remain confined within the drop due to the requirement for proton recombination prior to volatilization and their subsequent expulsion. This pH dependence for 2-nitrophenol is also in agreement with Borchers et al. (2024), for riming retention of cloud droplets.

The pH sensitivities for the binary mixtures are shown in Fig. 5.2b. Mixture A1 was omitted due to the larger standard deviation for acetic acid compared to formic acid as a single component. In mixture A2, both substances were retained completely. The same was found for mixture B. As shown in Fig. 5.2b, none of mixtures show any sensitivity to changes in pH.

5.3.3 Temperature Sensitivity

The temperature sensitivities for the single components are shown in Fig. 5.3a. Acetic acid (green marker) showed a higher retention coefficient at the lower temperature with large standard deviations of the measurements at both temperatures. At -6.9°C the retention coefficient for acetic acid was 1.14±0.24 and at -3.9°C it was 0.88±0.12. Formic acid (blue marker) did not show any variation in retention coefficient with changes in the drop freezing temperatures and was completely retained at both temperatures. 2-nitrophenol (red marker) also had a higher retention coefficient at the colder temperature (1.06±0.05) as compared to the warmer temperature (0.90±0.08). The retention coefficients for both acetic acid and 2-nitrophenol appeared to have a weak dependency on temperature and were completely retained at (-6.9°C) along with formic acid, which had no dependency and was completely retained at both temperatures. In the atmosphere, freezing is initiated at lower temperatures than our experimental temperatures here, indicating towards complete retention of the investigated species.

Unlike the single components, the binary mixtures did not show any temperature dependency as seen in Fig. 5.3b. Both sets of binary mixtures were fully retained at -3.9 ± 0.3 °C. At the colder temperature, the retention coefficients did not change and the mixtures were completely retained.

5.3.4 Relation with effective Henry's law coefficient

Retention coefficients of substances are strongly dependent on chemical properties such as aqueous diffusion, gaseous diffusion, interfacial mass transport, solubility and dissociation. Among them, solubility and dissociative effects characterized by effective Henry's law constant H^* were reported to be the dominant ones. Stuart and Jacobson (2003) and Jost et al. (2017) showed this relationship between the retention coefficient and H^*, where they stated that substances with H^* greater than 10^7 are completely retained. Substances with H^* lower than 10^4 are less likely to be retained or more likely expelled from the drop during riming-retention. Retention coefficients of all other substances with H^* values between these ranges followed a sigmoid shape (see Borchers et al., 2024, Figure 7).

The relation between effective Henry's law coefficient and retention coefficient for cloud droplets i.e., retention-riming, was modeled by the following equation

$$R_{H^*} = \left[1 + \left(\frac{a}{H^*}\right)^b\right]^{-1} \tag{5.4}$$

where the parameters $a = (2.41 \pm 1.06) \times 10^4$ and $b = 0.27 \pm 0.04$, respectively. Values a and b were taken from Borchers et al. (2024).

Figure 5.4 shows the relation between H^* and R. The gray markers are from previous studies for riming-retention (von Blohn et al., 2011; Jost et al., 2017; Borchers et al., 2024). The coloured markers are from the present study utilizing freezing-retention. Equation 5.4 was plotted in Fig. 5.4 against our current data for comparing the dependency of R on H^*, for μm sized droplets and mm sized drops.

It is apparent from Fig. 5.4, that nitric acid with an H^* of 10^{11} was completely retained. Formic acid was completely retained, too, which is in contrast to previous measurements from riming-retention studies in which it showed a lower retention coefficient (0.76). No definitive conclusion regarding changes in its measured retention coefficient can be made for acetic acid (0.88 for single component), due to large standard deviation and the overlap between the single components and the binary mixture measurements. Conversely, the riming-retention of acetic acid was much lower (0.6). 2-nitrophenol showed a much higher retention coefficient for large drops (0.9 and above) compared to its retention for small μm

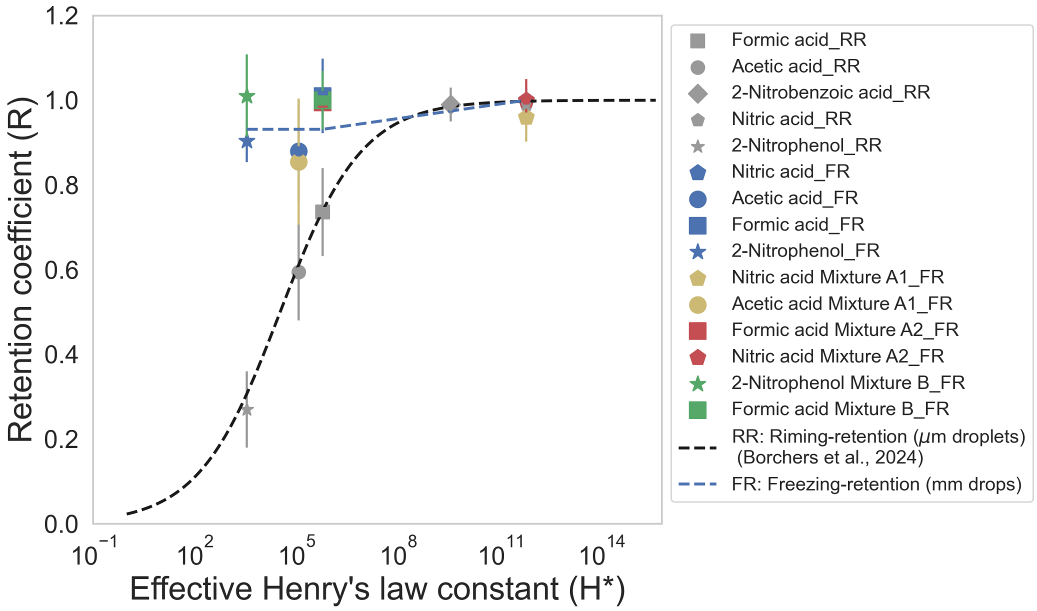

Figure 5.4: Retention coefficient (R) as a function of effective Henry's law coefficient (H^*). Grey markers: from riming-retention (RR) of small droplets (von Blohn et al., 2011; Jost et al., 2017; Borchers et al., 2024). Colored markers: from freezing-retention (FR, present study), with drop freezing temperature of -3.9 ± 0.3 °C. Blue markers: single components. Yellow (mixture A1), red (mixture A2) and green (mixture B) markers: binary mixtures.

sized droplets (0.27 at pH 5.6; Borchers et al. 2024). Considering its low H^* (10^3), one could expect the retention coefficient of 2-nitrophenol as a single component to be lower than 0.9, which was not the case here. In the mixture with formic acid, 2-nitrophenol was also completely retained. Specifically, Fig. 5.4 demonstrates that our results from freezing-retention deviate from the sigmoidal relationship between retention coefficients and H^* unlike the previous experimental studies involving riming-retention. This result is also seen in the conclusions of Part II of this publication series, where the retentions for ambient water soluble organic compounds of over 450 species were also investigated.

5.3.5 Retention indicator analysis

Another method to analyze retention is from the point of view of mass and heat transfer considerations, such as the mass expulsion and freezing timescales as suggested by Stuart and Jacobson (2003, 2004) and Jost et al. (2017). Retention indicator (RI) is introduced that is the ratio of total mass expulsion time (τ_{exp}) to the freezing time (τ_{frz}) as shown in Eq. (5.5). Table 5.3 shows the calculated timescales for the retention indicator of the single components investigated in this study.

$$RI = \frac{\tau_{exp}}{\tau_{frz}} \tag{5.5}$$

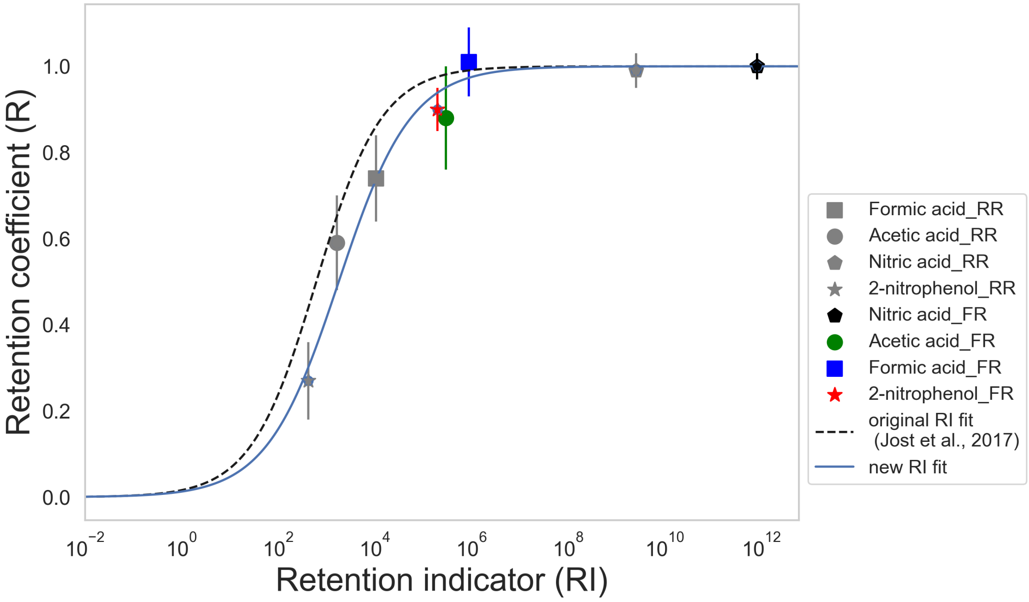

Figure 5.5: Retention coefficient of the substances investigated as single components as a function of the empirical retention indicator. Gray markers: from riming-retention (RR), coloured markers: from freezing-retention (FR). Dashed line: original retention indicator fit parameters from Jost et al. (2017), solid line: updated fit from current study.

$$\tau_{exp} = \tau_g + \tau_{aq} + \tau_i \tag{5.6}$$

where, $\tau_g = \frac{a^2 H^*}{3 D_g f}$; $\tau_{aq} = \frac{a^2}{D_{aq}}$; $T_i = \frac{4aH^*}{3v\alpha}$

The total solute mass expulsion time τ_{exp} is the sum of aqueous phase mass expulsion time τ_{aq}, gaseous phase mass expulsion time τ_g, and interfacial mass transfer expulsion time τ_i. In Eq. (5.6) τ_g accounts for the gaseous diffusivity D_g, where a is the radius of the drop, H^* is the effective Henry's law coefficient and f is the ventilation coefficient (f= 5.6; Szakáll et al. 2021). τ_{aq} accounts for the aqueous diffusivity D_{aq} of the substance. τ_i takes into consideration for the mass accommodation coefficient α and the thermal velocity of the chemical in air, v .

A fourth timescale involving the aqueous phase kinetics was also introduced by Jost et al. (2017). This timescale is specifically important for substances such as ammonia and formaldehyde since they react with atmospheric carbon dioxide and are affected by dehydration of methanediol, respectively (Jost et al., 2017). For substances investigated in this study, the aqueous phase kinetics and reactions are negligible, so this timescale was not considered. The experimental temperatures, pH values, initial concentrations and H^* are also listed in Table 5.3 for reference. The freezing time τ_{frz} was derived experimentally via high speed camera (Motion Pro Y3M; pixel size: 12 × 12 μm; resolution: 1024 × 1280 pixels) at 600 frames per second, as shown in Fig. A.3. The time from the initiation of freezing to the complete formation of an ice-shell around the levitated drop was approximately 4.8 ms. The ice-shell formation takes place very rapidly during the adiabatic freezing stage of the drop, where drop surface temperature rises to 0°C (see A.1.1). After the formation of the ice-shell the dissolved solute remains inside and retained during freezing. Hence, this ice-shell formation time was considered as the freezing time for the retention indicator calculation.

It is also clearly evident in Table 5.3 that τ_{frz} is several orders of magnitude smaller compared to τ_{exp}. Gas phase expulsion time τ_g appears to be the controlling factor contributing to the total high τ_{exp} for nitric and formic acid, and aqueous phase expulsion timescale τ_{aq} for acetic acid and 2-nitrophenol. In Jost et al. (2017) the parameterization relating RI and retention coefficient is given as

$$R_{RI} = \left[1 + \left(\frac{c}{RI}\right)^{d}\right]^{-1} \tag{5.7}$$

Equation 5.7 is depicted in Fig. 5.5, where the original parameters taken from Jost et al. (2017) are $c_1 = 618 \pm 71$ and $d_1 = 0.64 \pm 0.06$ (black dashed line, Fig. 5.5). From our study, an updated fit is provided with $c_2 = 1800 \pm 95$ and $d_2 = 0.58 \pm 0.07$ (blue solid line, Fig. 5.5).

Figure 5.5 shows the variation of retention coefficients with RI. In contrast to Fig. 5.4, both the riming-retention and freezing-retention measurements fit well with the parameterization given in Eq. 5.7. This analysis corroborates our experimental results for mm sized raindrops with μm sized cloud droplets. These results can be categorized with timescale analysis and follow a similar relation with both previous experimental (Jost et al., 2017) and theoretical (Stuart and Jacobson, 2003, 2004) studies.

5.3.6 Physical parameters

Our study shows that retention is dependent on the size of the droplets which needs to be considered when modeling the mass flux of trace substances with numerical models. An aspect of the importance of the physical parameters is surface area to volume ratio. The rain sized drops in this study have a surface area to volume ratio of 3×10^3 m^{-1}. The cloud droplets in earlier retention-riming studies have a surface area to volume ratio of about 2×10^7 m^{-1}. Thus, this ratio is approximately 4 orders of magnitude higher for the cloud droplets compared to the rain drops. As such, the dissolved substances in raindrops have more diffusional volume and smaller surface area. Additionally, low surface area to volume ratio for the case of the rain drops is an indicator of lower overall desorption as well (Jost, 2017).

Another physical parameter influencing retention is the ventilation coefficient. It describes the enhanced heat and mass transfer around hydrometers in an airflow. For the riming-retention studies, substances measured inside a wind tunnel (μm sized droplets) had ventilation coefficients of about 30 to 32 (Jost et al., 2017, Table 4). In contrast, the ventilation coefficient in the acoustic levitator for the 2 mm diameter drops was about 5.6 (Szakáll et al., 2021). As such, a smaller ventilation coefficient would incur less transfer of mass and heat for the 2 mm raindrops as compared to the retention measurements for μm

Table 5.3: List of parameters used for retention indicator calculation.

Parameters	Nitric acid	Acetic acid	Formic acid	2-nitrophenol	Comments
^{1}D$_{aq}$	2.25×10^{-5}	1.29×10^{-5}	1.63×10^{-5}	1.07×10^{-5}	Aqueous diffusivity (cm^2/s)
^{1}D$_g$	0.12	0.12	0.14	0.07	Gaseous diffusivity (cm^2/s)
pH	4.1	4.2	4.2	4.4	Experimental pH values
$^2H^*$	7.56×10^{11}	1.28×10^5	8.31×10^5	3.50×10^3	Dimensionless Henry's law constant
$^3\alpha$	0.06	0.07	0.05	0.01	Mass accommodation coefficient
T	-3.9	-3.9	-3.9	-3.9	Temperature (°C)
C	20	20	20	20	Concentration (mg/L)
τ_g	3.88×10^9	6.37×10^2	3.55×10^3	2.81×10^1	Gas phase expulsion time (s)
τ_i	2.11×10^7	7.78×10^0	6.36×10^1	2.19×10^0	Interfacial expulsion time (s)
τ_{aq}	6.81×10^2	7.72×10^2	6.13×10^2	9.28×10^2	Aqueous phase expulsion time (s)
τ_{exp}	3.90×10^9	1.42×10^3	4.23×10^3	9.59×10^2	Total expulsion time (s)
τ_{frz}	4.80×10^{-3}	4.80×10^{-3}	4.80×10^{-3}	4.80×10^{-3}	Ice-shell formation time (s)
RI	8.13×10^{11}	2.95×10^5	8.80×10^5	2.00×10^5	Retention indicator
R	1.00 ± 0.03	0.88 ± 0.12	1.01 ± 0.08	0.90 ± 0.05	Retention coefficient
Controlling parameter	τ_g	τ_{aq}	τ_g	τ_{aq}	

[1] The diffusivities in water D_{aq} and in air D_g calculated at 273K (Thibodeaux and Mackay, 2010), [2] Effective Henry's law constant calculated at 273K and at their corresponding pH (Tremp et al., 1993; Johnson et al., 1996; Warneck and Williams, 2012), [3] The mass accommodation coefficient at 273K (Ervens et al., 2003; Davidovits et al., 2006).

sized droplets.This could be seen as an important physical parameter aiding higher expulsion times and, consequently, higher retention coefficients as seen in the RI analysis. We found aqueous and gaseous diffusion as a limiting factors in our RI analysis, which limits the mass transport of the species to the environment (Table 5.3). In a real atmospheric scenario, 2 mm drops falling at their terminal velocity have a ventilation coefficient of about 15 (Pruppacher and Klett, 2010). A higher ventilation coefficient will increase the mass transfer and thereby decrease the expulsion timescale. However, the ventilation coefficients of heat and mass transfer is almost the same. Therefore an increase in mass transfer would also imply a faster freezing time..

The fast freezing rates observed in our study imply that the molecules do not have much time to diffuse away from the forming ice front. This means the molecules are easily captured by the ice and form defects in the ice crystal lattice. Stuart and Jacobson (2006) reported the formation of liquid pockets that can trap solutes during freezing, informed from previous studies of dendritic crystal growth in solutions. These liquid pockets were also seen in our experiments. The ice-shell formation impedes further retention because diffusion in ice is orders of magnitude lower compared to the liquid. As a result, only a small fraction of the solute is expelled. This high degree of solute incorporation into the ice is the primary factor contributing to the observed high retention in our study.

Observations of naturally frozen drops and laboratory experiments (Lauber et al., 2018) have shown frozen rain drops having deformations and protuberances. Rise in internal pressure during freezing could have the potential for cracks or splitting of ice-shell during freezing, leading to expulsion of solute mass and perhaps source for secondary ice production (Field et al., 2017; Korolev and Leisner, 2020). Kleinheins et al. (2021) reported cracking of the ice-shell for internal pressure above 100 bar for 300 μm sized drops. The internal pressure built up during freezing in our experiments was found to be about 81 bar. Within our experimental conditions, these occurrences were however not seen.

The temperature difference between the freezing drop and the environment may influence the freezing and retention. During the initiation of freezing the drop temperature rises to 0°C (FigA.1), where the fraction of liquid freezes and majority of latent heat released during cooling contributes to warming the supercooling drop to 0°C (Szakáll et al., 2021). We assume that ice-shell forms very rapidly at this stage, which can be perceived as adiabatic freezing (see A.1.1) with no exchange of heat to the environment. Thus, we expect that this freezing stage should not be affected by the temperature difference between the drop and the ambient air.

5.4 Conclusions

At the onset, we successfully characterized the freezing of levitated rain drops (2.0 ± 0.1 mm) at three different concentrations and temperatures using the acoustic levitator setup. We measured the retention coefficients of nitric acid, formic acid, acetic acid and 2-nitrophenol as single components and their combinations as binary mixtures, during the freezing of rain drops. In addition to these measurements, we also checked the sensitivity at three different pH levels (pH 3, 4 and 6/7) and at two different temperatures (-3.9 ± 0.3 °C and -6.9 ± 1.1 °C) .

We conclude that for rain sized drops (mm and above), most of the chemical species are completely retained during freezing. This can be interpreted as the physical parameters -— such as drop size and ice-shell formation -— dominating the chemical properties concerning retention influences. After an ice-shell is formed around a drop during the initiation of freezing, it is significantly more difficult for the dissolved species to be expelled from the drop, thus leading to higher mass expulsion timescales.

Substances studied as single components show sensitivity (for 2-nitrophenol and acetic acid) with changes in either pH or temperatures. Formic acid as a single component is not sensitive to changes in pH or temperatures. Binary mixtures also do not show any sensitivity for changes in pH and freezing temperature.

Our retention indicator analysis shows that the shorter freezing and longer expulsion timescales (a minimum of 5 orders of magnitude higher) lead to higher retention for the investigated species. This indicates that during the freezing of mm sized raindrops all dissolved trace gases may be removed by precipitation in deep convective clouds or transported within the ice phase into the UT where it can be released upon sublimation. Concurrently, factors such as ventilation, temperature differences, crack formation during freezing and concentration of dissolved solute needs to be dealt meticulously. Our results, combined with results from riming-retention studies facilitates the extrapolation of retention of the investigated trace gases from μm to mm sized drops in computational studies.

Our results show higher retention coefficients (close to 1) for similar substances in mm sized raindrops as compared to previously determined retention coefficients in μm sized cloud droplets (von Blohn et al., 2011; Jost et al., 2017; Borchers et al., 2024). It is important to note that in addition to the differences in droplet size, the freezing pathways were also different. The previous studies utilized the riming-retention mechanism while in the present work we incorporated a contact-free freezing-retention mechanism.

We derived new parameterizations for the retention indicator to include large mm sized raindrops, and thus, updated the previously obtained ones that only considered μm sized cloud droplets (Jost et al., 2017). This result is beneficial in terms of computational expense for the chemistry coupled atmospheric and earth system modelling as modelling freezing raindrops would not require much additional computational resources.

Our experiments were conducted with single components and binary mixtures but in the real atmosphere, air is mixed with numerous complex trace gases that are in constant turbulent motion. Our current database does not have many substances with H^* values lower than 10^3, and such substances might behave differently during freezing. Future retention experiments that sample for trace gas at the ground level and at different vertical profiles could improve our understanding of the underlying micro-physical and chemical processes within convective systems. Our experiments also indicate that it is critical to further investigate the ice-shell formation process during the freezing of raindrops. Furthermore, in-depth investigation of the effect of ventilation and examination of internal pressure build up during freezing for rain drops also provides an interesting aspect to investigate in future studies.

Future studies should investigate how these and similar organic compounds behave when they are in the real atmosphere. In Part II we investigate the retention of a complex mixture of organic compounds sampled from Beijing urban aerosols through the same experimental setup with high resolution mass spectrometry analysis.

Data Availability: The data supporting this study are available at the repository Gautam and coauthors (2024). Additional data (if required) for this study are available upon request from the corresponding authors.

Author Contribution: MG, MZ, AT, JS, SM participated in designing the experiments; MG, MH performed the experiments; MG, MH, JS conducted analytical measurements, MG analysed the data and wrote the manuscript draft; AT, JS, MH, SB, KD, MZ reviewed and edited the manuscript.

Competing Interests: The authors declare no competing interests.

Acknowledgements: This work was funded by the Deutsche Forschungsgemeinschaft (DFG, German Research Foundation) – TRR 301 – Project-ID 428312742.

Chapter 6

Fast dynamics of freezing raindrops

In this chapter, the results of the experiments conducted to investigate the freezing timescales are presented. The primary focus was on the formation of an ice-shell just after the initiation of freezing. This ice-shell was found to be a major limiting factor for high chemical retention of dissolved solutes during freezing, as reported in Chapter 3. Hence, an in-depth timescale investigation of the freezing process was the main motivation for explaining the contrasting high retention coefficients.

6.1 Methods

6.1.1 Modifications of the M-AL setup

The experimental setup used for investigating the ice-shell formation during the freezing of raindrops with high-speed camera was modified from the earlier setup employed in ice nucleation studies shown in Chapter 3 (see Fig. 3.2). (see Fig. 3.2). The USB camera and the infra-red thermometer were replaced with two high-speed cameras as shown in Fig. 6.1. The high-speed cameras were: 1) Motion Pro Y3M; pixel size: 12 μm × 12 μm; maximum resolution: 1024 × 1280 pixels, and 2) Motion Pro X3; pixel size: 12 μm × 12 μm; maximum resolution: 1024 × 1280 pixels. The size of the recorded images was 640 × 480 pixels. A light reflector plate was added to the setup for increasing the illumination for recordings at higher frame rates. Video recordings were done at 600, 1000, and 1500 frames per second, owing to light and storage availability during the experiments.

For measuring the adiabatic and diabatic freezing time, the infrared thermometer (KT 19.82 II, Heitronics) was used. For simultaneous measurement of the three characteristic timescales, one of the high-speed cameras (#2 in Fig. 6.1, Motion Pro X3) was replaced with the infrared thermometer. Following the definition from Sec. 3.1, the adiabatic freezing time is the freezing stage characterized by a rapid crystal growth and the latent heat released during freezing being mostly absorbed by the supercooled drop, raising its surface temperature to 0 °C. Whereas, diabatic freezing time is the longer freezing stage, characterized by the exchange of heat from the drop to its environment as the supercooled drop solidifies. The experiments were carried out around 3 different ambient temperatures, i.e., temperature of the walk-in cold room as -28 ± 1 °C (∼245 K), -20 ± 1 °C (∼253 K) and -15 ± 1 °C (∼258 K).

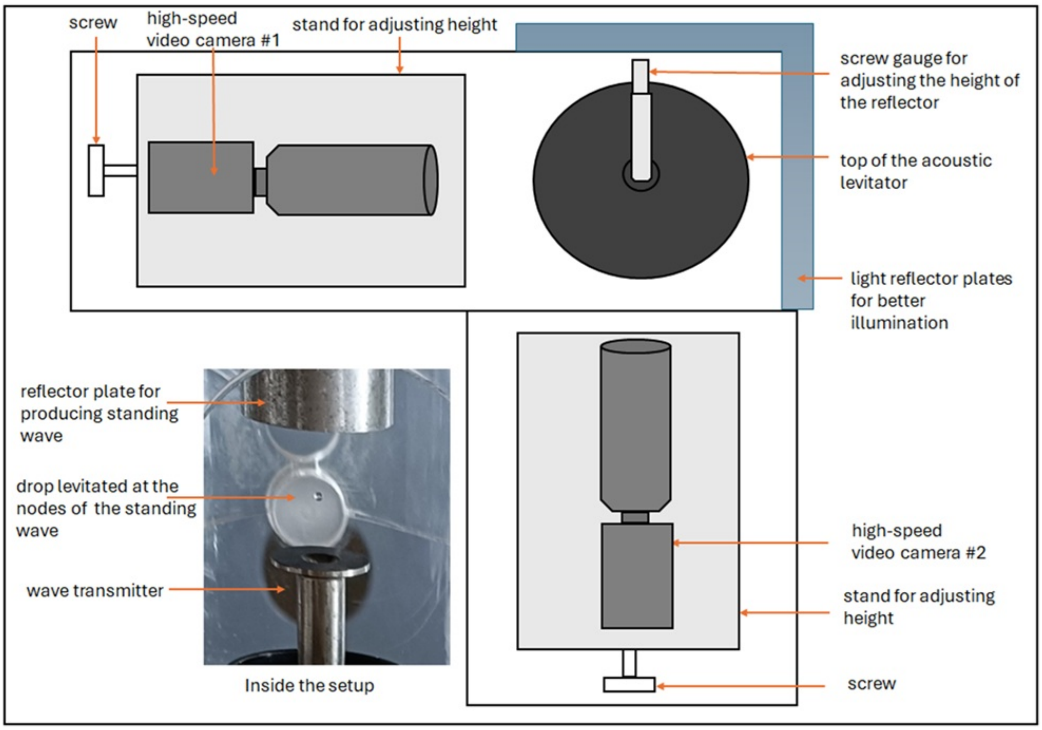

Figure 6.1: Schematic of the M-AL setup for recording ice-shell formation during freezing of raindrops, with high-speed cameras. Two light sources were located at about 45° angle to the high-speed video camera #1.

Freezing experiments were conducted with AgI, illite-NX, and feldspar as INPs. Experiments were also performed with AgI as a standalone INP and AgI with added solutes, namely NaOH, in varying solute mass concentrations of 20 and 60 mg/L. The list of INPs used and their concentrations are shown in in Table 6.1.

Table 6.1: List of INPs used in the high-speed experiments

INP Name	Concentration (g/L)	Source
AgI	0.016, 0.2	Sigma Aldrich (99%) [a]
Illite-NX	0.3, 0.6	Arginotec GmbH [b]
Feldspar (Microcline)	0.7	IAG TU Darmstadt [c]

[a] same as Ch. 5, [b] same as Szakáll et al. (2021), [c] same as Peckhaus et al. (2016)
Sodium Hydroxide (NaOH): Merck (99%) - for high-speed experiments with dissolved substances.

Another significant modification to the M-AL setup for these experiments was the addition of external ventilation to observe its effect on the freezing timescales. However, due to limitations of the setup, very minimal external flow of 0.6 L/hr could be achieved without disrupting the existing acoustic field of the setup. This external ventilation was equivalent to about 0.2 cm/s when measured with an anemometer (VelociCalc 9535, TSI).

6.1.2 Processing of data

The recorded images and videos were analyzed frame by frame to accurately pinpoint the start and the end of ice-shell formation time. The temporal evolution of the drop surface temperature from the infrared thermometer was used to calculate the adiabatic and diabatic freezing timescales. The adiabatic freezing time was evaluated from the initiation of freezing (i.e., at drop freezing temperature T_f), until the drop surface temperature reached 0 °C (T_0). The diabatic freezing time was evaluated from the time when the drop surface temperature reached T_0, until the drop surface temperature decreased consecutively for 3 measurement points. The temporal resolution of the infrared thermometer recording was 250 ms. Also seen in Fig. A.1 is that the drop surface temperature remained at 0 °C for a short while after reaching T_0, and started decreasing sharply only after the drop was completely frozen. Sizing of the drops from the high-speed video/image recording was done using the ImageJ software application (Schneider et al., 2012). For the plots in the subsequent sections, the characteristic timescales during freezing of raindrops, namely ice-shell formation time, adiabatic and diabatic freezing time, were plotted as a function of drop sizes, drop freezing, and ambient temperature. For each of these plots, either a linear, power law, or exponential fit is provided. The choice of either of these fits was determined by the one that had the lowest root mean square (RMSE) values. Only relations derived from the best fit (linear, exponential, or power law fits with the least RMSE values) of the experimental dataset were considered. Linear regression coefficients p and Pearson's correlation coefficients r were evaluated using SPSS V23. Linear regression tests were conducted within a 95% confidence interval. For p values less than 0.05, the pair of variables is considered to have a statistically significant linear relationship.

6.2 Results and Discussions

In this section, the results of high-speed freezing experiments are shown and discussed. Overall 274 frozen drops were analyzed from high-speed recordings. Out of these 274 drops, adiabatic and diabatic time freezing time were recorded for 192 drops. The drop sizes varied from 1.1 mm to 2.7 mm in diameter.

6.2.1 Phenomenological observations from high speed recordings

Some of the experimentally observed behaviors during the freezing process are shown in this section. Figure 6.2 shows the sequence of images for ice-shell formation during the freezing process, recorded at 1000 fps. The ice-shell formation time for illite-NX as INP was 19 ms (Fig. 6.2a) and 9 ms for feldspar (Fig. 6.2b). In Fig. 6.2a, three air bubbles can be seen on the top left corner inside the levitating drop. Such bubbles didn't impact the rapid crystal growth process or the ice-shell formation, as initiation of freezing even though random, was predominantly found to be a surface phenomenon.

As the levitated drop enters the diabatic freezing stage, exchange of heat and energy takes place between the drop and the environment. During this freezing stage, deformation of the close to spherical shape of the levitated drops can be seen in the vertical direction as the semi-frozen drop expands and aligns itself in the acoustic field. These deformations were seen in the form of protrusions from the drop surface in the vertical direction, along the standing wave produced by the acoustic field (Fig. 6.3).

Two very prominent features can be seen during the freezing of raindrops. Firstly, the formation of liquid pockets during freezing. And secondly, the rapid refreezing of the vertical protrusions

Trapping of liquid in pockets during dendritic growth during freezing of liquid solvents has been well described by Myerson and Kirwan (1977a,b). At the temperatures for the present experiments, in the adiabatic freezing stage, the rapid crystal growth occurred mostly in the form of dendritic projections. Myerson and Kirwan (1977a) and Stuart and Jacobson (2006) showed that for fast growth rates, dendritic projections trap pockets of liquids from either propagating side branches or via direct impingement of the dendritic branches on each other. Within our experimental conditions, formation of such liquid pockets was a regular feature, which can also be seen as bubbles around the vertical axis of the sequence of drops shown in Fig. 6.3. These liquid pockets were also dependent on the amount or concentration of impurities (INPs and NaOH in our case) present in the solvent (pure water in our case). The higher the concentration of the INPs and NaOH was, the fewer prominent liquid pockets were observed. This phenomenological observation was, however, not investigated to a greater extent within the scope of the analyses.

The rapid refreezing of the vertical protrusions are shown in Fig. 6.3, for the images at the later time frames in the sequence. Due to the rotation of the drop in the acoustic field, alongside potentially low internal circulation within the drop during its freezing, the liquid pockets mostly align themselves centrifugally along the vertical axis. Internal circulation within the drop is expected to be very low, given the small size of the levitated drops and the high viscosity of growing ice crystals. The liquid fractions of the semi-frozen drops, as they undergo subsequent freezing, exert pressure on the ice-shell. Lauber et al. (2018) also show such deformations in their experiments with 85 and 310 μm sized drops, and mention that this internal pressure is responsible for cracking of the ice-shell. As discussed in Chapter 5, the internal pressure built within our experimental constraints did not extend beyond the threshold of 100 bar specified in Kleinheins et al. (2021). During the current set of experiments, the internal pressure was calculated to be lower than 85 bar. Another possibility for cracking of the ice-shell is that the formed ice-shell could be incomplete or fissures could be present when freezing is initiated through a contact (Wildeman et al., 2017;

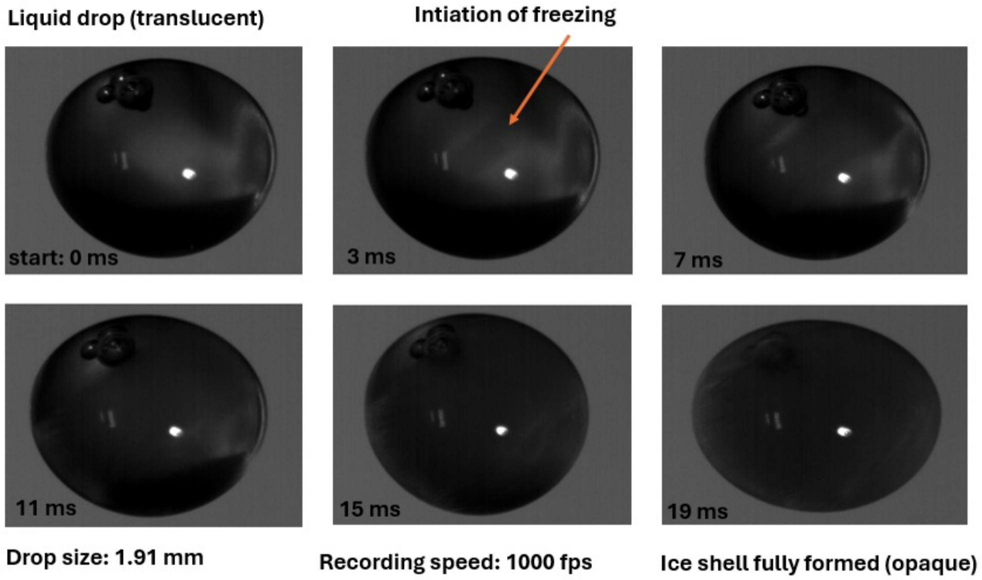

(a) Ice-shell formation with illite-NX as INP, at -20 °C ambient temperature, for a 1.91 mm drop, recorded at 1000 fps. The freezing front propagating from left to right direction.

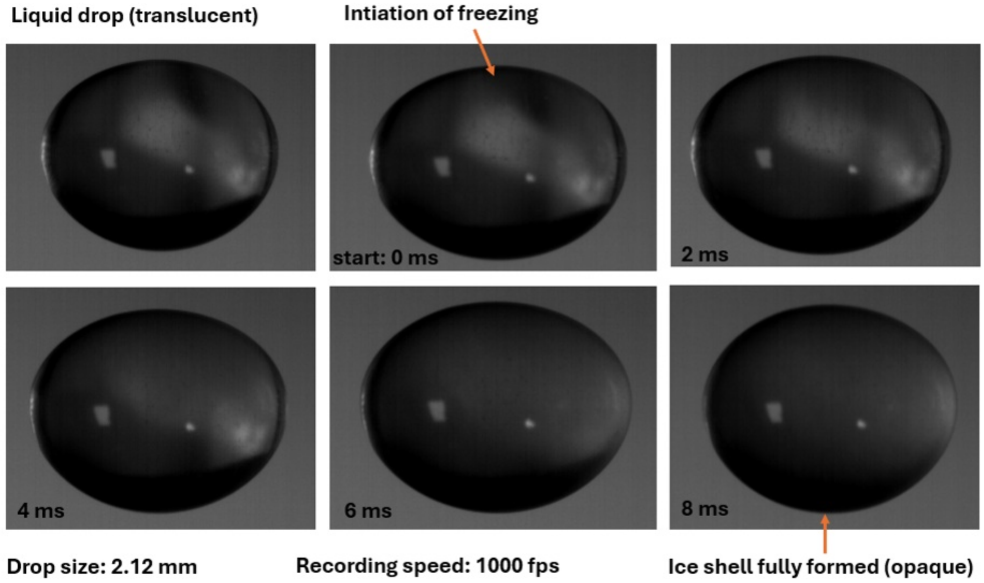

(b) Ice-shell formation with feldspar as INP at -28°C ambient temperature, for a 2.12 mm drop, recorded at 1000 fps. The freezing front propagating from top to bottom direction.

Figure 6.2: Sequence of images showing ice-shell formation for a) illite-NX and b) feldspar. Red arrows showing the location of freezing initiation.

Kleinheins et al., 2021). Nevertheless, any such incident could lead to small ice particles or spicules being ejected out during freezing, a form of secondary ice production (SIP) mechanism reported in experimental studies of Lauber et al. (2018) and Kleinheins et al. (2021). Such SIP pathways were not observed with the current setup and in the range of conditions investigated here.

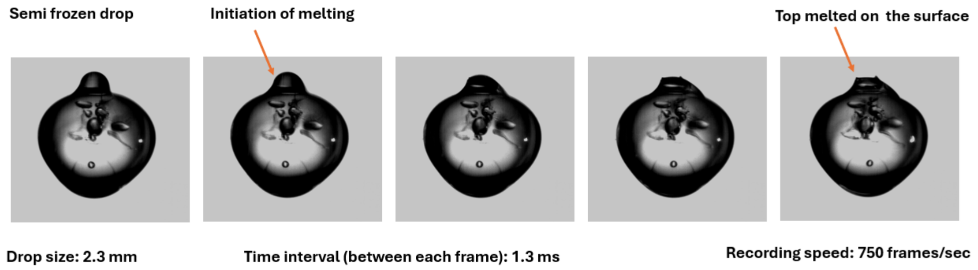

Figure 6.3: Image sequence showing the melting and refreezing of the vertical protrusions during freezing of raindrops. The drop was 2.3 mm in diameter, and was recorded at 750 fps

6.2.2 Crystal growth rates

The determination of ice crystal growth rates from the experiments was not straightforward measurements. The stochastic nature of ice nucleation, spherical geometry of the acoustically levitating drops, and the possibility of ice front propagating in multiple directions affects the actual crystal growth rates. This necessitated the estimation of possible range of growth rates. The crystal growth rates were estimated by considering both the possibilities that ice nucleation could occur on the surface of the drop, as well from inside the drop. For initiation of ice nucleation at the surface, the upper limit crystal growth rate G_{m1} was determined by the ratio of the drop circumference (assuming the near spherical geometry prior to deformation during freezing) to the time from the initiation until a fully developed ice-shell was seen for the levitated drops. The lower limit of the crystal growth rate was determined considering the scenario if by any chance initiation of freezing occurs inside the drop. The maximum time required for the growing ice crystals to encompass the entire drop would be, when ice nucleation takes place exactly at the center of the drop. In essence the lower limit of ice crystal growth rate G_{m2} was calculated from the ratio of the radius of the levitated drops to the ice-shell formation time. Both these growth rates are shown in Fig. 6.4. The coefficients of growth rates G_m from the present study take the form:

$$G_{m1} = 0.024(\Delta T)^{1.13} \tag{6.1}$$

$$G_{m2} = 0.0052(\Delta T)^{1.03} \tag{6.2}$$

where G_{m1} is the growth rate considering drop circumference, G_{m2} is the growth rate considering drop radius, and ΔT is the supercooling temperature. In the analysis, ΔT is the same as the drop freezing temperature T_f.

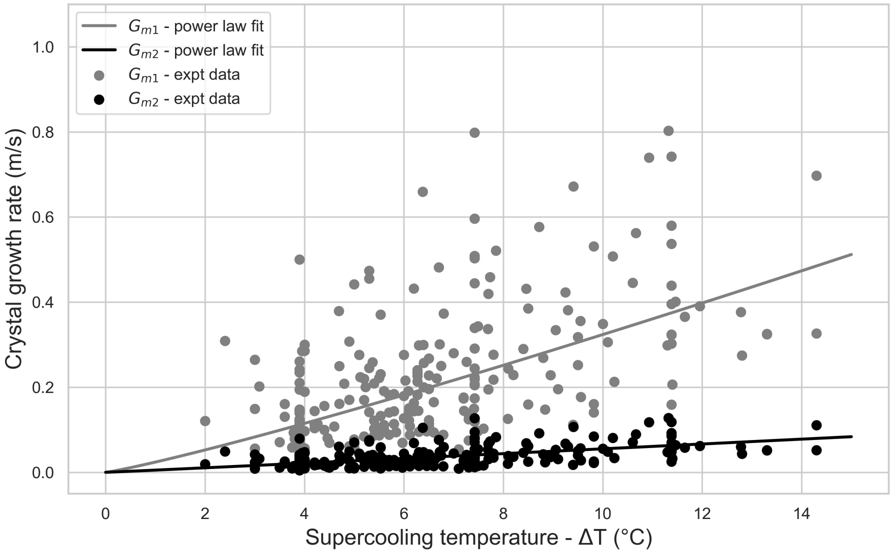

Figure 6.4: Crystal growth rates derived from experimental data. G_{m1} is the ratio of drop circumference to ice-shell formation time, and G_{m2} is the ratio of drop radius to ice-shell formation time.

A comparison of ice crystal growth rates from previous experimental studies is shown in Fig. 6.5. Pruppacher and Klett (2010), Tab. 16.1, show that the ice crystal growth rates vary approximately as the square of supercooling temperature (ΔT). From experiments with supercooled salt solutions, Pruppacher (1967) also reports a deviation from this near quadratic dependence of the crystal growth rates on ΔT around 9 °C and shows almost a linear dependence of crystal growth rates for ΔT beyond 12 °C. The crystal growth rates for ice were determined for supercooled water in fine tubular structures by Lindenmayer (1959, L 59) and Hallett (1964, H 64), shown in Fig. 6.5. The nature of their experiments enabled for much easier determination of crystal growth rates in bulk phase. Gokhale and Lewinter (1971, G 71) reported the freezing of 2 mm drops on a glass slide by spraying supercooled AgI particles on them. They reported the highest freezing rate among the three studies. In the present study, the crystal growth rates were found to vary almost linearly, as opposed to the observed quadratic form in those previous studies. Nevertheless, the ice crystal growth rates mentioned in previous studies lie well within our estimated crystal growth range.

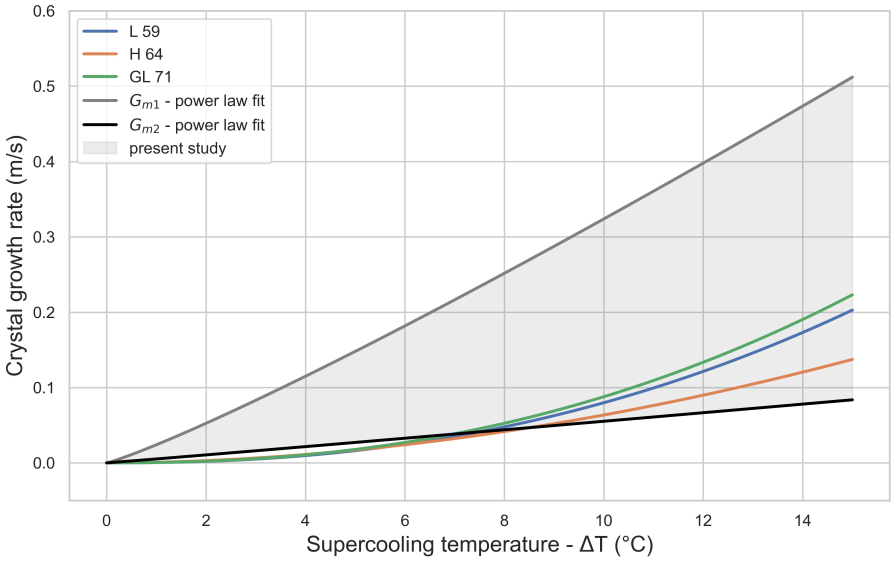

Figure 6.5: Comparison of crystal growth rates. L 59, H 64, and GL 71 are crystal growth rates from Lindenmayer (1959); Hallett (1964) and Gokhale and Lewinter (1971), respectively.

The findings of Lauber et al. (2018) and Stuart and Jacobson (2003) that the formation of ice-shell takes place only after adiabatic freezing is completed are somewhat debatable from our experimental findings. The ice-shell most likely forms during the adiabatic freezing stage, when the ice front after initiation propagates and covers the entire surface area of the drop. Further results and discussions specific to ice-shell formation times are given in the following section. Further comparative details regarding crystal growth rates for individual INPs are provided in Table 6.2.

6.2.3 Ice-shell formation time

Figure 6.6 shows the ice-shell formation time as a function of drop freezing temperature, indicating that it decreased with decreasing drop freezing temperatures. Red hollow circles are measurements without the use of any external ventilation in the setup, and the blue filled circles are measurements with additional ventilation. Overall, the average ice-shell formation time for the 274 frozen raindrops in the 1.1 to 2.7 mm size range was found to be 42.74 ms. The average externally introduced ventilation was about 0.2 cm/s of compressed nitrogen gas. The average values for ice-shell formation time without ventilation were found to be 48.69 ± 38.77 ms, and 35.47 ± 22.11 ms with external ventilation, a reduction of about 27%. Ice-shell formation time showed a highly significant linear dependence ($p = 1.2 \times 10^{-14}$) on drop freezing temperature. Wildeman et al. (2017) in their experiments on freezing of millimetric-sized drops reported the formation of an ice-shell within a few hundredths of a second (around 25 ms), after the initiation of freezing. However, their experiments were performed inside a vacuum chamber, and ice nucleation was induced via contact with a AgI tip, after the drop stayed at a fixed supercooling temperature for about 3 minutes. Wildeman et al. (2017) observed formation of ice spicules protruding out of the shell in about 60 ms, similar to the ones seen in Fig. 6.3. In the current experiments, such protrusions were seen only after 1-2 seconds. Following such protrusions, cracking of ice-shells or bursting of ice spicules were observed from about 250 ms to a few seconds from the start of freezing (Wildeman et al., 2017; Lauber et al., 2018; Kleinheins et al., 2021). As mentioned earlier (and in Chapter 5), no such cracking or bursting events leading to SIP were observed during the present study.

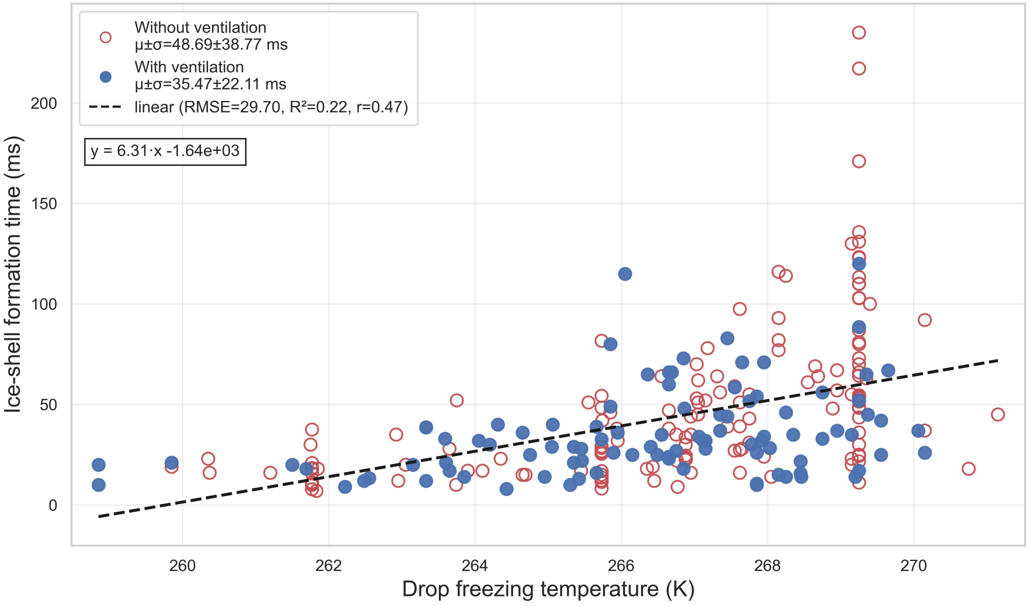

Figure 6.6: Ice-shell formation time as a function of the drop freezing temperature. Red empty circles show data points without external ventilation, while blue filled circles are data points where external ventilation was introduced.

The variation of ice-shell formation time with ambient cold room temperatures is shown in Fig. 6.7. Ice-shell formation time was observed to slightly decrease with decreasing ambient temperatures. The correlation between ice-shell formation time and ambient temperature was found to be about 0.15, much lower than 0.45 between ice-shell formation time and drop freezing temperatures. Similar to drop freezing temperature, ice-shell formation time showed significant linear dependence on ambient temperatures ($p = 0.019$).

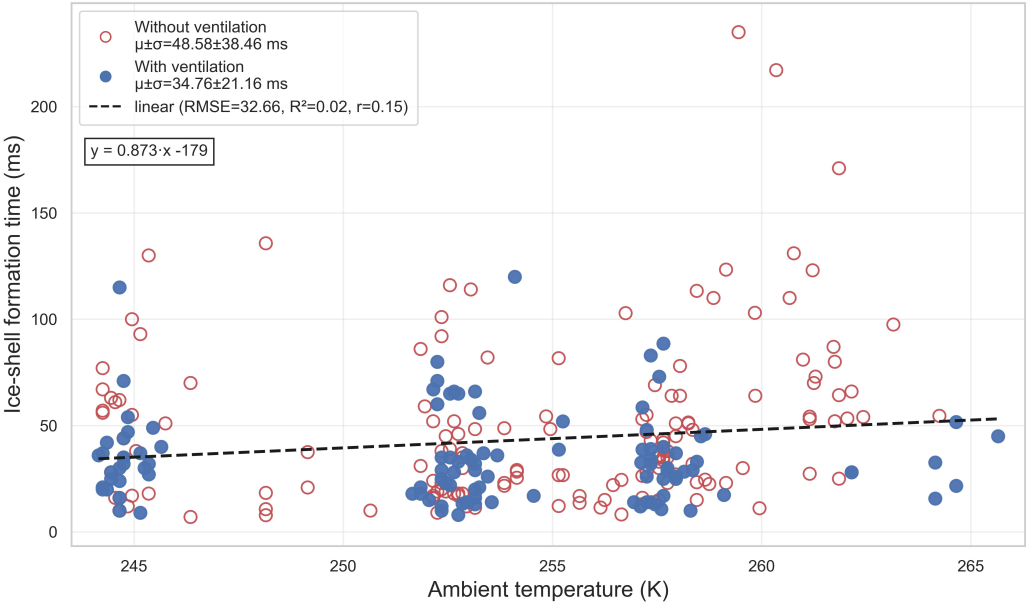

Figure 6.7: Ice-shell formation time as a function of the ambient temperature. Red empty circles show data points without external ventilation, while blue filled circles are data points where external ventilation was used.

In experiments where two video cameras were used, the infrared thermometer could not be placed within the frame of measurement. For those experiments and whenever AgI was the INP, the median drop freezing temperatures obtained in Table 4.1 were used as the drop freezing temperatures in our analysis. Those data points can be clearly seen in Figures 6.6 and in some of the subsequent plots as the vertically stacked red circles, most evidently seen at 269.25 K (-3.9 °C). Besides the three different experimental temperatures mentioned in Section **??**, a few experiments performed at intermediate temperatures and also around ∼265 K (-8 °C) are included as well in the analysis, as seen in Fig. 6.7.

The variation of ice-shell formation time with respect to drop diameter is shown in Fig. 6.8. Ice-shell formation time is seen to increase with increasing drop sizes. A decrease of 35% was seen in the average ice-shell formation time for experiments with external ventilation (blue filled circles). The average values for ice-shell formation time without ventilation were found to be 48.37 ± 38.42 ms, and 34.76 ± 21.16 ms with external ventilation. Similar to drop freezing temperatures, ice-shell formation time revealed highly significant linear dependence on drop diameter, with $p = 3.96 \times 10^{-7}$. The Pearson's correlation coefficient r was found to be 0.31.

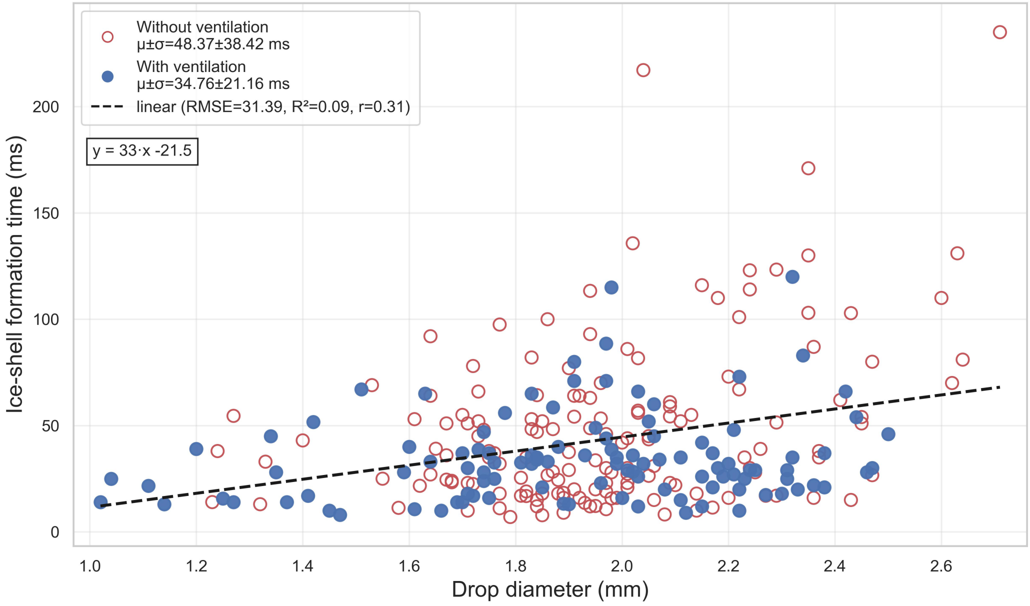

Figure 6.8: Ice-shell formation time as a function of the drop diameter. Red empty circles show data points without external ventilation, while blue filled circles are data points where external ventilation was used.

Normalized ice-shell formation time

In Figs. 6.6 to 6.8, the standard deviation in ice-shell formation time is quite significant for experiments with and without ventilation, as compared to their mean values. This large variation facilitated the use of a combined dataset of drops with and without external ventilation for determining mathematical expressions from the observations. Ice-shell formation time was normalized with drop circumference and plotted against drop freezing temperature (in Fig. 6.9) and ambient temperatures (in Fig. 6.10) for a better representation of the data. Normalized ice-shell formation time is the inverse of the crystal growth rates mentioned in the previous section. Assuming a very low probability of ice-shell formation as drop freezing temperature approaches 0 °C, 273.15 K, an asymptotic power law fit is proposed from the experimental data (shown in Eq. 6.3). The normalized ice-shell formation time I_{T1} as a function of drop freezing temperature (T_f) is given by

$$I_{T1} = -26.7 \times (T_f)^{0.182} + 44.2 \tag{6.3}$$

A similar expression for the normalized ice-shell formation time I_{T2} can be obtained as a function of ambient temperature (T_∞) from Fig. 6.10 as

$$I_{T2} = -1.25 \times 10^4 (T_\infty)^{0.00028} + 1.26 \times 10^4 \tag{6.4}$$

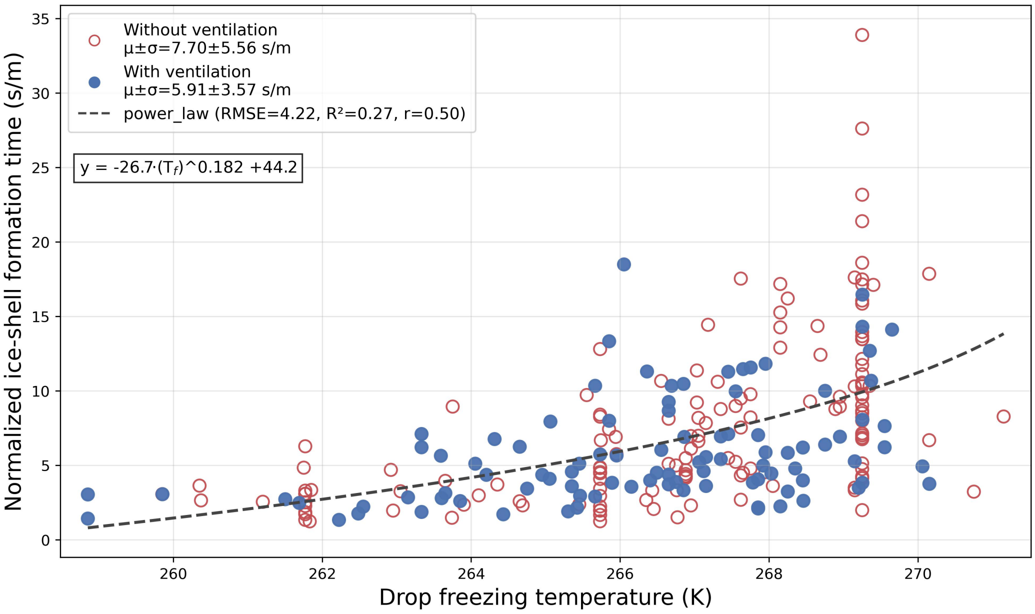

Figure 6.9: Normalized ice-shell formation time as a function of the drop freezing temperature.

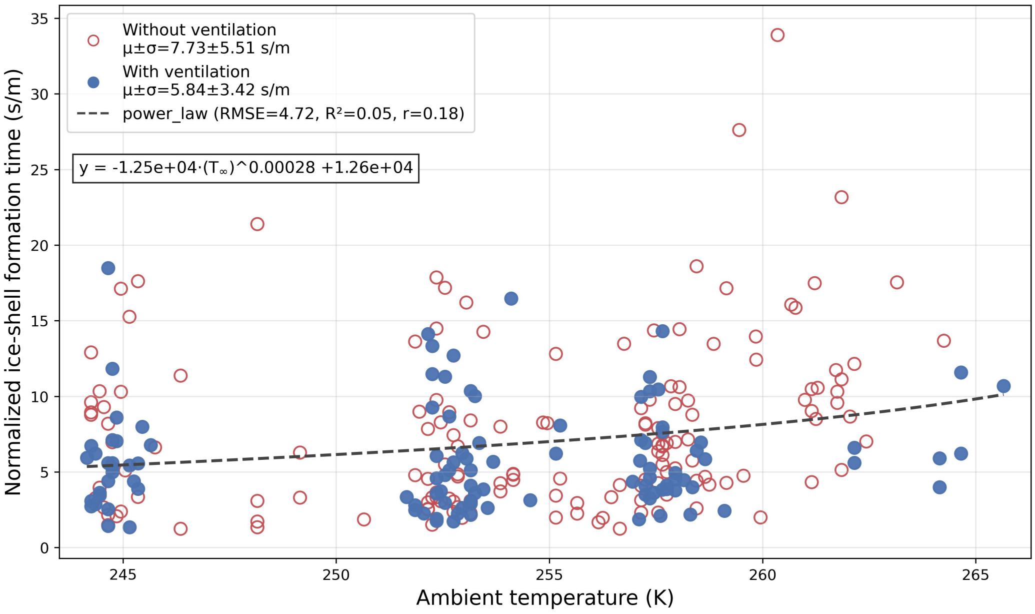

Figure 6.10: Normalized ice-shell formation time as a function of the ambient temperature.

6.2.4 Adiabatic freezing time

The adiabatic freezing stage is characterized by rapid ice crystal growth and warming up of the drop surface temperature to 0 °C. The temporal evolution recorded by the infrared thermometer was used to determine the adiabatic freezing time. The time taken for the drop surface temperature to increase from the drop freezing temperature (T_f) until it reaches 0 °C was considered as the adiabatic freezing time. Adiabatic freezing times were recorded for 192 drops from the total of 274 drops, as the infrared thermometer was not present in all the experiments due to limited space around the setup.

The adiabatic freezing time of a levitating drop was found to be about an order of magnitude higher than the ice-shell formation time. The variations of adiabatic freezing time with drop freezing temperature and ambient temperature are shown in Figures 6.11 and 6.12, respectively. The average adiabatic freezing time was found to be about 0.6 s for drops both with and without external ventilation. However, unlike ice-shell formation time, there was no statistically significant dependence of adiabatic freezing time on the drop freezing temperatures (Fig. 6.11), with $p = 0.98$.

Linear regression tests revealed significant dependence of adiabatic freezing time on ambient temperatures ($p = 0.009$). Colder ambient temperatures showed slightly shorter adiabatic freezing time on average, as compared to warmer ambient temperatures. However, the recorded data showed a lot of scatter, and the adiabatic freezing time varied from 0.17 s to 1.21 s.

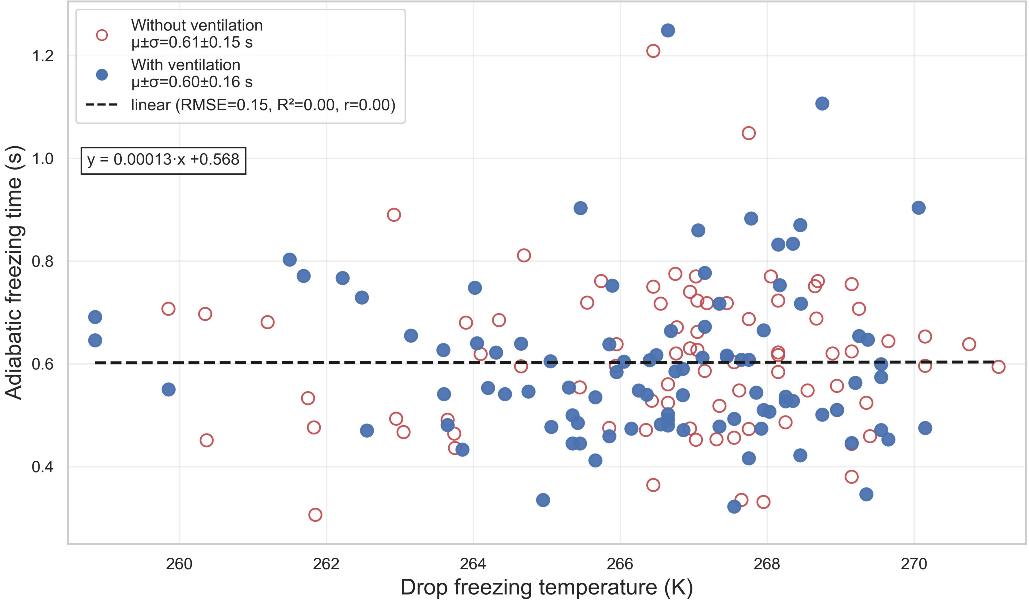

Figure 6.11: Adiabatic freezing time as a function of the drop freezing temperature.

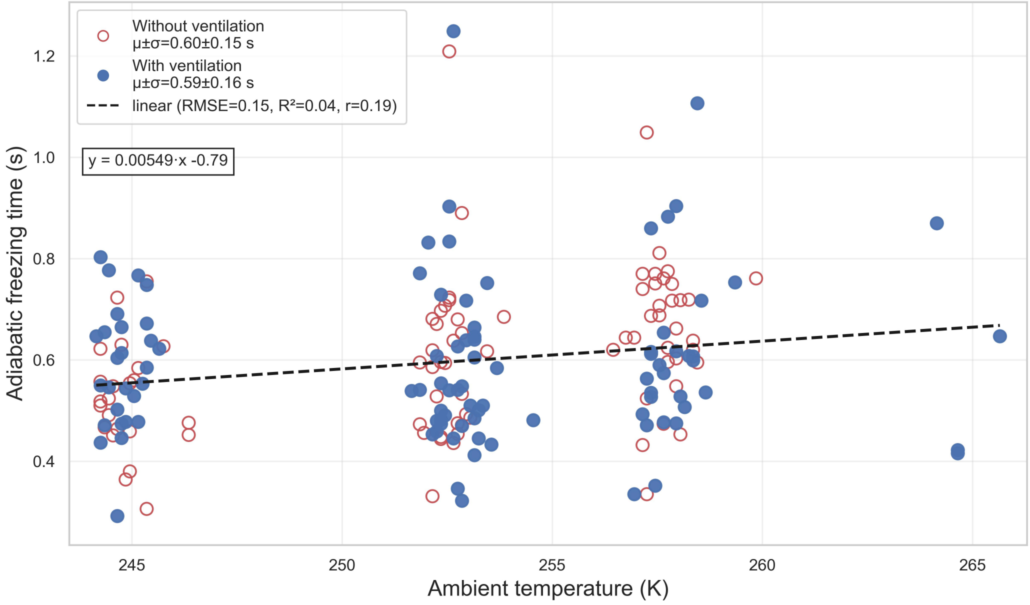

Figure 6.12: Adiabatic freezing time as a function of the ambient temperature.

The variation of adiabatic freezing time as a function of the drop diameter is shown in Fig. 6.13. In general, the smaller drops seem to have slightly lower adiabatic freezing times ($r = 0.29$). Linear regression tests showed highly significant dependence of adiabatic freezing time on drop diameter, with $p = 8.10 \times 10^{-5}$.

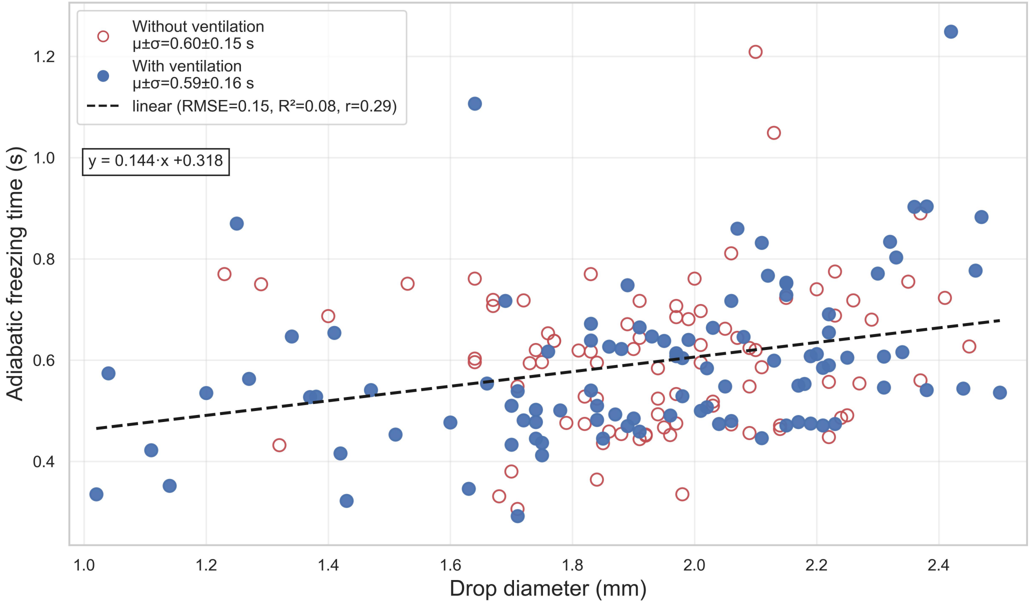

Figure 6.13: Adiabatic freezing time as a function of the drop diameter.

Normalized adiabatic freezing time

Adiabatic freezing time was normalized with respect to the drop surface area. Since in the adiabatic freezing stage, the latent heat released during the rapid crystal growth is used to raise the temperature of the entire drop surface to 0 °C, the normalization was performed w.r.t. the drop surface area. Normalized adiabatic freezing time showed slightly better correlations with both drop freezing temperature (Fig. 6.14, $r = 0.21$) and ambient temperature (Fig. 6.15, $r = 0.48$).

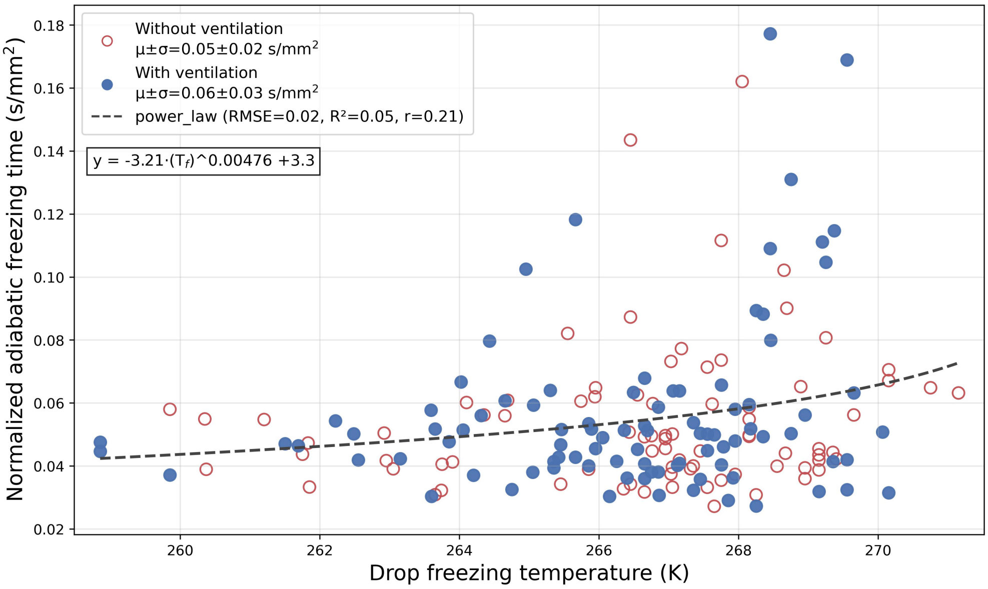

Figure 6.14: Normalized adiabatic freezing time as a function of the drop freezing temperature.

And the asymptotic relations derived from a power law fit are provided as

$$A_{T1} = -3.21 \times (T_f)^{0.00476} + 3.3 \tag{6.5}$$

$$A_{T2} = -148 \times (T_\infty)^{0.000324} + 148 \tag{6.6}$$

where, A_{T1} and A_{T2} are the ratios of adiabatic freezing time to drop surface area, dependent on drop freezing temperature (T_f), and ambient temperature (T_∞), respectively.

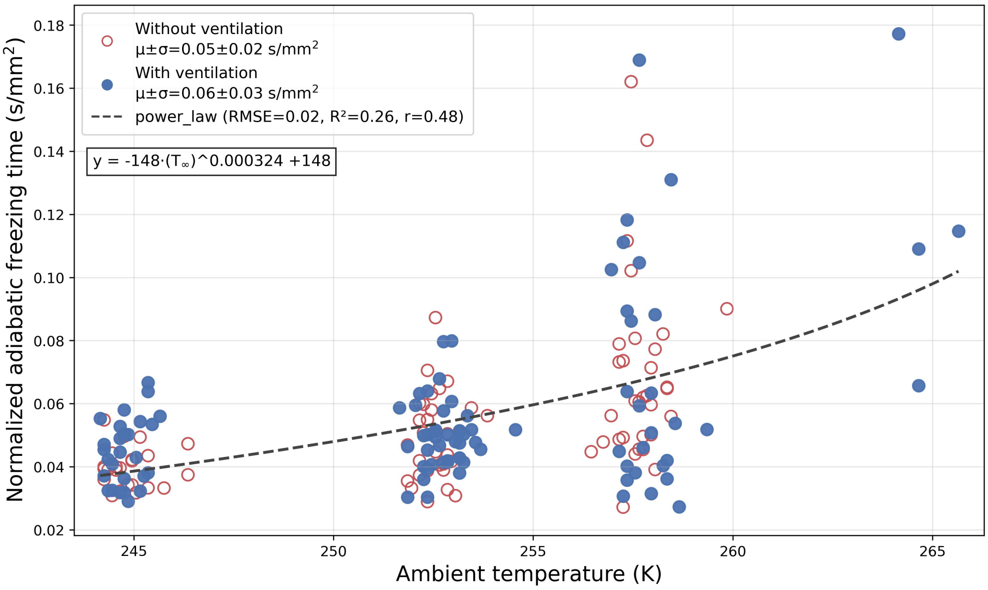

Figure 6.15: Normalized adiabatic freezing time as a function of the ambient temperature.

6.2.5 Diabatic freezing time

The recorded diabatic freezing timescales are plotted against drop freezing temperatures and the ambient temperature of the cold room. The variation of diabatic freezing time for different drop freezing temperatures is shown in Fig. 6.16. Diabatic freezing time was observed to be decreasing with the decrease in drop freezing temperatures. Due large scatter in the data, linear regression tests did not show any statistically significant dependence of diabatic freezing time on drop freezing temperatures ($p = 0.063$).

The exchange of latent heat of freezing and subsequent cooling is dependent on the ambient temperature (Pruppacher and Klett, 2010). Thus, in Fig. 6.17, a fairly linearly increasing relationship between diabatic freezing time and ambient temperature can be seen. Faster diabatic freezing times were observed for colder ambient temperatures. A stronger correlation for diabatic freezing time on ambient temperatures ($r = 0.44$) can be seen as compared to drop freezing temperatures ($r = 0.13$). Diabatic freezing time also showed highly significant statistical dependence on ambient temperatures, with $p = 1.80 \times 10^{-10}$.

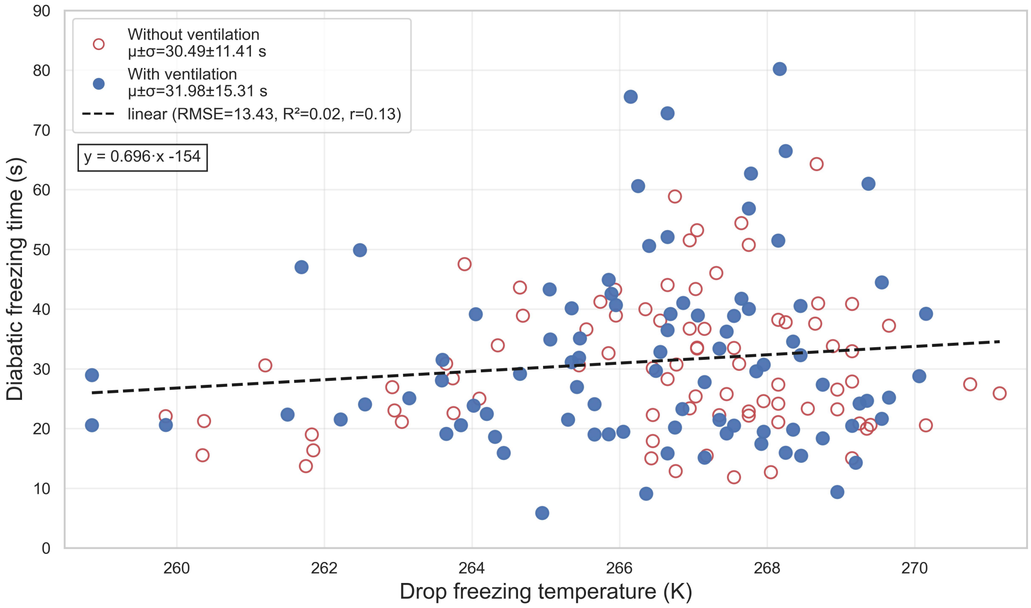

Figure 6.16: Diabatic freezing time as a function of the drop freezing temperature.

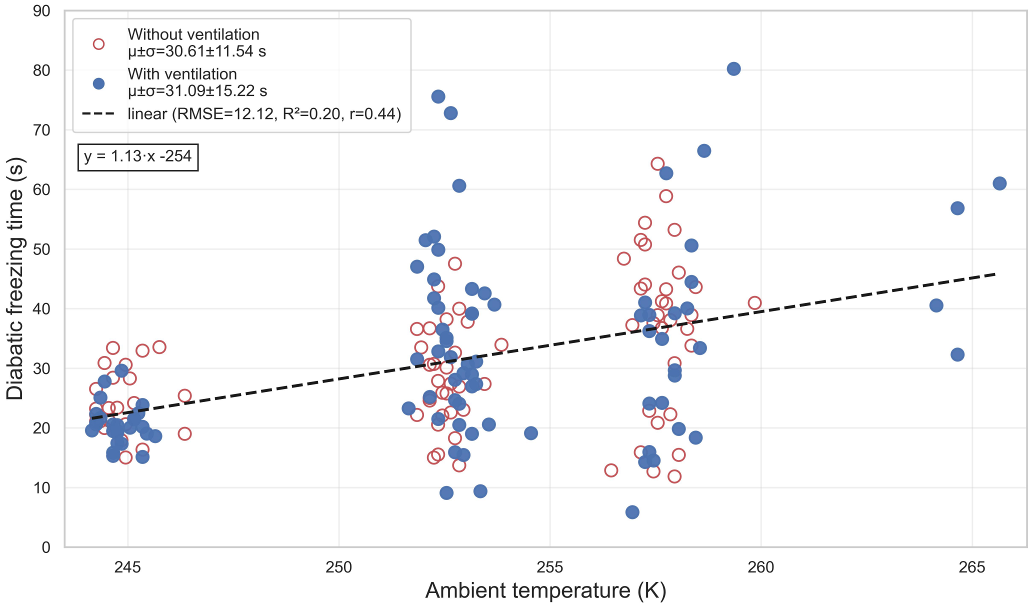

Figure 6.17: Diabatic freezing time as a function of the ambient temperature.

In Figures 6.16 and 6.17, the results from experiments including all different INPs and all drop sizes are shown. The average diabatic freezing time was found to be 30.61 ± 11.54 for drops without external ventilation and 31.09 ± 15.22 for drops with external ventilation (Fig. 6.17). In essence, any external ventilation should increase heat and mass transfer, leading towards shorter diabatic freezing times for the externally ventilated drops (Pruppacher and Klett, 2010). Experiments with external ventilation showed large scatter in the data and higher standard deviations, clearly seen in Fig. 6.17, at ambient temperatures around 253 K (-20 °C) and 258 K (-15°C). This could be attributed to the different INPs being activated at different supercooling temperatures, and also to instability in the acoustic field of the levitator. As described in section 4.1, AgI, for instance, is a very efficient INP so that for a fixed ambient temperature, AgI initiates freezing at warmer supercooling temperatures as compared to other mineral dusts, and comparatively warmer supercooling temperatures would affect slower crystal growth rates. Also, the fact that at 265K (-8 °C) four externally ventilated drops were observed, and no drops without external ventilation could create a small bias towards higher average diabatic freezing times seen for externally ventilated drops. A more detailed analysis of the diabatic freezing times and the effect of external ventilation for individual INP is discussed in Section 6.2.7.

The diabatic freezing time was seen to increase with increasing drop diameter ($r = 0.39$), shown in Fig. 6.18. Similarly, diabatic freezing time also showed highly significant dependence on drop diameter, with $p = 1.50 \times 10^{-5}$. Additionally, it can be noted that doubling the drop sizes results in almost doubling the diabatic freezing time.

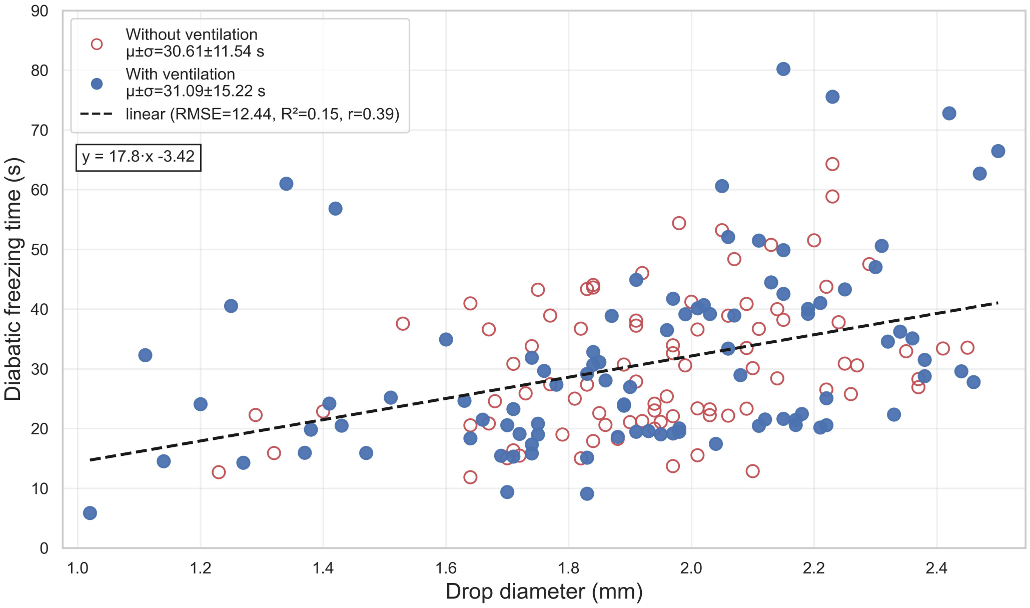

Figure 6.18: Diabatic freezing time as a function of the drop diameter.

Normalized diabatic freezing time

For the diabatic freezing stage, the rate of heat dissipated via forced convection from the drop surface to the environment influences the freezing time (see Sec. 3.1). For larger drops, more heat needs to be dissipated during its freezing. Similar to adiabatic freezing time, diabatic freezing time normalized over the drop surface area is shown as a function of drop freezing and ambient temperatures in Figs. 6.19 and 6.20. For normalized diabatic freezing time and its variation with drop freezing temperatures D_{T1}, a linear fit revealed the least RMSE values, while its variation with ambient temperatures D_{T2} revealed power law fit function with least RMSE values. These relations are given as

$$D_{T1} = 0.135(T_f) - 33.2 \tag{6.7}$$

$$D_{T2} = -1.73 \times 10^4 (T_\infty)^{0.000255} + 1.73 \times 10^4 \tag{6.8}$$

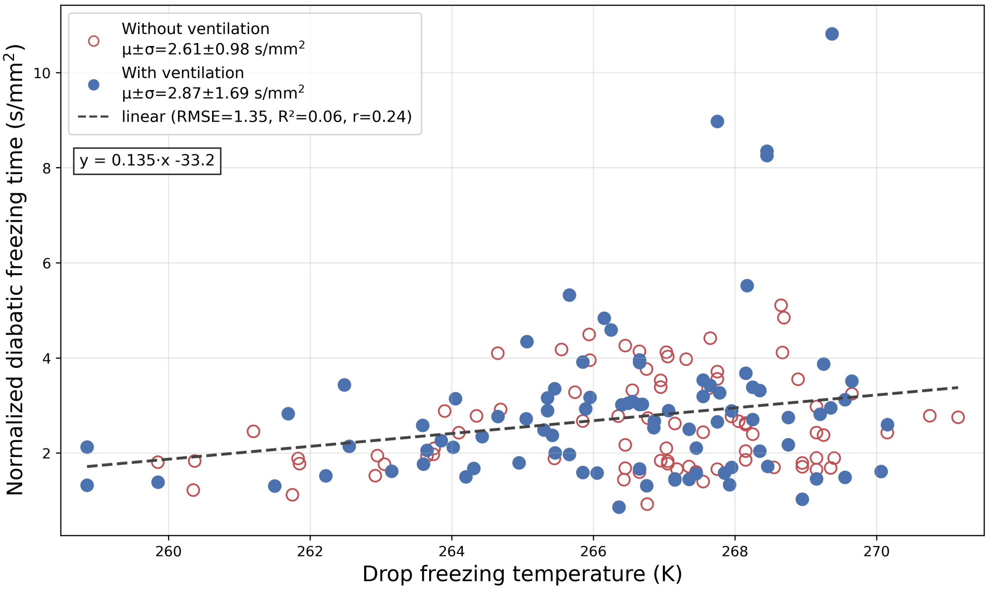

Figure 6.19: Normalized diabatic freezing time as a function of the drop freezing temperature.

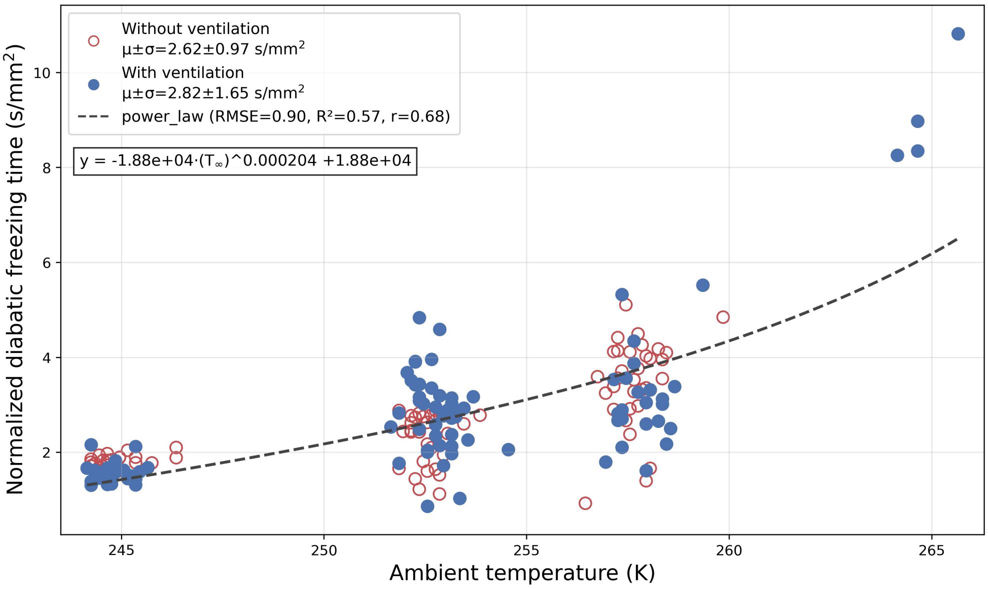

Figure 6.20: Normalized diabatic freezing time as a function of the ambient temperature.

6.2.6 Numerical approaches

Estimation of adiabatic freezing time

From experimental observations, adiabatic freezing did not show any significant dependencies on the drop freezing or supercooling temperature, but heavily depended on the drop sizes and ambient temperatures. To represent the freezing of the levitated drops with a comparatively warm core in a much colder ambient environment, a simple and energy based spherical shell model was considered. The latent heat released during the adiabatic freezing stage is absorbed by the supercooled drop to raise the drop temperature to 0 °C. Assuming no heat loss to the environment, the heat balance of the drop can be represented from Pruppacher and Klett (2010) as

$$m_{ice} L_f = m_{tot} c_p \Delta T \tag{6.9}$$

where m_{ice} is the mass of the frozen part of the drop and m_{tot} is the total mass of the drop (both frozen and unfrozen combined); L_f is the latent heat of freezing, which is 334 kJ/kg; c_p is the specific heat capacity of water and is about 4.2 kJ/(kg K); and ΔT is the supercooling temperature.

The frozen mass fraction can be found as

$$f_{mass} = \frac{m_{ice}}{m_{tot}} \approx \frac{c_p \Delta T}{L_f} \tag{6.10}$$

By assuming a very thin ice outer layer around the drop of radius a, the relation between volumetric frozen mass fraction and shell thickness δ can be represented as

$$\begin{aligned} f_{vol} &= 1 - \left(1 - \frac{\delta}{a}\right)^3 \\ &\approx \frac{3\delta}{a}, \forall(\delta \ll a) \end{aligned}$$

and rearranging the above equation gives

$$\delta \approx \frac{f_{vol} a}{3} \tag{6.11}$$

The total adiabatic freezing time can also be estimated using ice front growth velocity $(G^{'})$, as

$$t_{ad}{'} = \frac{\delta}{G'} \tag{6.12}$$

$G^{'}$ is not to be confused with the crystal growth rates G_{m1} and G_{m2} mentioned earlier. An intrinsic kinetic dependence can be assumed between growth velocity $G^{'}$ and the supercooling temperature ΔT (Zhang and Harrington, 2014). However, without finer details on the growth kinetics at a microscopic level, the intrinsic kinetic dependence is considered to be an empirical kinetic coefficient (k_{int}), which is related to $G^{'}$ and ΔT as

$$G^{'} = k_{int} \Delta T \tag{6.13}$$

Further assuming $f_{mass} \approx f_{vol}$, and using equations 6.10, 6.11, and 6.13, the theoretically estimated adiabatic freezing time in Eq. 6.12 can be expressed independently of the supercooling temperature ΔT and growth velocity $G^{'}$ as

$$t_{ad}{}' \approx \frac{c_p}{3L_f k_{int}} a \tag{6.14}$$

In the above equation, all the other terms except k_{int} are constant (c_p and L_f) or determined experimentally (a). k_{int} is dependent on the solvent (water in this case) and the interaction of dissolved solutes or suspended particles on the growth kinetics of ice.

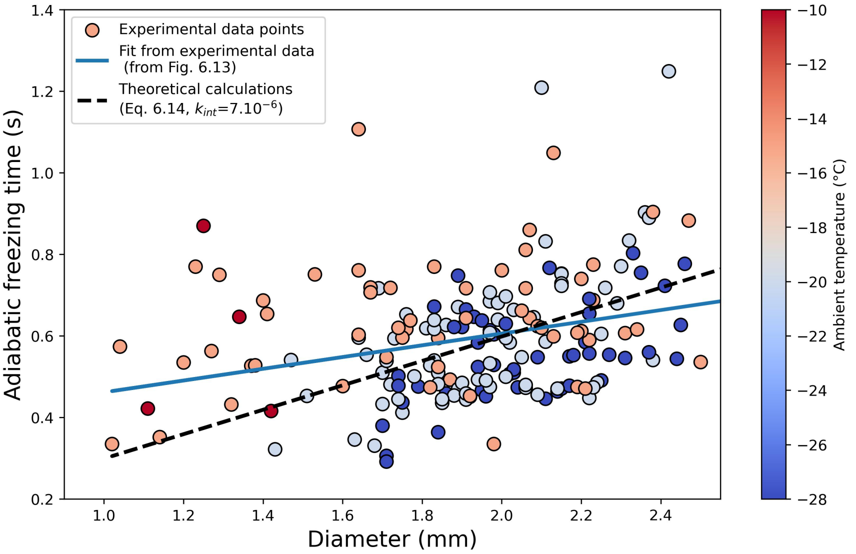

Figure 6.21: Comparison of experimental adiabatic freezing times with calculations from energy shell model. Different colors indicate the different ambient temperatures. Orange, red, light blue, and dark blue colored markers correspond to -10, -15, -20, and -28 °C ambient temperatures, respectively. The black dashed line shows the adiabatic freezing time calculated from Eq. 6.14. Blue line shows the linear fit for adiabatic freezing time as a function of the drop diameter obtained in Fig. 6.13.

Taking the average adiabatic freezing time as 0.6 s, and drop radius of 1 mm, k_{int} $= 7 \times 10^{-6}$ with units $\mathrm{m/(K\,s)}$. The adiabatic freezing times calculated from energy shell model via Eq. 6.14 and measured from the experiments are plotted in Fig. 6.21. Numerically estimated adiabatic freezing times ($t_{ad}{}'$) show fairly good agreement with the observed adiabatic freezing times, especially for experiments performed at -20 and -28 °C (light and dark blue dots, respectively). However, for the experiments at warmer temperatures (-10 and -15 °C), a large variation can be seen.

Estimation of diabatic freezing time

Similar to adiabatic freezing time, the diabatic freezing time can also be represented via diffusional heat conduction approach through a spherical ice substrate, explained in detail in Pruppacher and Klett (2010, Chapter 13). Due to the difference in temperature between a motionless drop and its environment, a sensible heat flux is produced. The conductive heat flux density (J_h) can be derived from Fourier's law as a function of thermal conductivity in air (k_a) and the temperature gradient (Pruppacher and Klett, 2010) as

$$J_h = -k_a(\nabla T) \tag{6.15}$$

where $\nabla T = \frac{\delta T}{\delta x}$ is the rate of change of temperature (T) with distance from the center of the drop (x). At $x = \infty$, T_∞ is temperature of the drop environment, at $x =$ drop radius a, T_a is the drop surface temperature. For the motionless drop in equilibrium, the rate of pure diffusional heat transfer (q) is given (Szakáll et al., 2021) as

$$\left(\frac{dq}{dt}\right)_0 = -k_a \int_S \left(\frac{\delta T}{dx}\right)_{x=a} dS \tag{6.16}$$

Solving the above integral for temperature at steady state conditions for $x = \infty$ and $x = a$, the conductive heat transfer over the drop surface area is expressed as

$$\left(\frac{dq}{dt}\right)_0 = -J_{h,a} = 4\pi a k_a(T_\infty - T_a) \tag{6.17}$$

Further, the rate of change of heat (q) and mass (m) due to the release of latent heat can be mathematically expressed as

$$\left(\frac{dq}{dt}\right)_0 = -L_e \left(\frac{dm}{dt}\right)_0 \tag{6.18}$$

where L_e is the latent heat of evaporation (2260 kJ/kg). Similar to heat transfer rate, the mass transfer rate of the motionless drop at equilibrium is obtained from Szakáll et al. (2021) as

$$\left(\frac{dm}{dt}\right)_0 = -D_v \int_S \left(\frac{\delta \rho_v}{dx}\right)_{x=a} dS \tag{6.19}$$

In Eq. 6.19, D_v is the diffusivity of water vapor, and ρ_v is the water vapor density. For a motionless drop, the above integral can be solved for ρ_v at steady state boundary conditions. At $x = \infty$, $\rho_{v,\infty}$ is the water vapor density of ambient conditions far away from the drop, and at $x = a$, $\rho_{v,a}$ is the water vapor density at the drop surface. Thus,

$$\left(\frac{dm}{dt}\right)_0 = 4\pi D_v(\rho_{v,\infty} - \rho_{v,a}) \tag{6.20}$$

In a realistic case, the presence of airflow will affect these heat and mass transfer rates, which is addressed with the help of ventilation coefficients f_h and f_v for heat transfer and mass transfer, respectively (Pruppacher and Klett, 2010, Chapter 13). When a relatively warm drop is injected into an environment colder than the drop temperature, a conductive heat flux flows from the air into the drop, described by Eq. 6.17. Concurrently, heat is lost from the drop due to evaporation as shown in Eq. 6.18. Combining equations 6.17, 6.18, and 6.20, and considering the ventilation coefficients, the total rate of heat gained by the drop can be expressed as

$$\left(\frac{dq}{dt}\right)_{total} = 4\pi a k_a f(T_\infty - T_a).f_h + 4\pi L_e D_v(\rho_{v,\infty} - \rho_{v,a}).f_v \tag{6.21}$$

This total heat flux into the drop causes the drop temperature to cool down at a rate proportional to its mass, given by

$$\left(\frac{dq}{dt}\right)_{total} = mc_p\frac{d}{dt}(T_a - T_\infty) \tag{6.22}$$

where m is the mass of the drop and c_p is the specific heat capacity of water. By equating Eqs. 6.21 and 6.22, the drop temperature adaptation is governed by the following equations

$$mc_p\frac{d}{dt}(T_a - T_\infty) = 4\pi a k_a(T_\infty - T_a).f_h + 4\pi L_e D_v(\rho_{v,\infty} - \rho_{v,a}).f_v \tag{6.23}$$

$$\frac{4}{3}\pi a^3 \rho_w c_p \frac{d}{dt}(T_\infty - T_a) = -4\pi a k_a(T_\infty - T_a).f_h - 4\pi L_e D_v(\rho_{v,\infty} - \rho_{v,a}).f_v \tag{6.24}$$

Integrating Eq. 6.24, the drop temperature adaptation can be approximated as

$$T_\infty - T_a(t) = (T_\infty - T_{a,0})exp(-t/\tau) \tag{6.25}$$

where $T_{a,0}$ is the initial temperature of the drop, and τ is the reciprocal of the exponential decay constant in Eq. 6.24, given as

$$\tau = \frac{a^2 \rho_w c_p}{3\left[k_a L_e D_v \left(\frac{d\rho_v}{dt}\right)_{sat}\right] f} \tag{6.26}$$

An assumption here is that the ventilation coefficients for heat and mass transfer are equal, i.e., $f_h = f_v = f$. From the drop surface temperature measurements via the infrared thermometer, relaxation time τ was found to be 14.26 s. Using this experimentally derived τ at -20°C in Eq. 6.26, ventilation coefficient f was found to be 3.26.

From the experimentally derived f, the diabatic freezing time for an isolated drop was calculated by assuming quasi steady state conditions for heat transfer. The rate of release of latent heat during freezing, the rate of heat conduction through the ice-shell, and the rate of heat loss due to evaporation and conduction to the environment are equal to each other. These heat balance conditions are represented by the following relations in Pruppacher and Klett (2010, Chapter 16) as

$$4\pi\rho_w L_m r^2 \frac{dr}{dt}\left(1 - \frac{c_p \Delta T}{L_m}\right) = \frac{4\pi k_i a r[T_o - T_a(r)]}{a-r} \tag{6.27}$$

and

$$\frac{4\pi k_i a r[T_o - T_a(r)]}{a-r} = 4\pi a k_a (T_a(r) - T_\infty).f_h + 4\pi L_e D_v(\rho_{v,a} - \rho_{v,\infty}).f_v \tag{6.28}$$

where $\rho_w = 1000\ \mathrm{kg\,m^{-3}}$ is the density of water, and $L_m = 334\ \mathrm{kJ\,kg^{-1}}$ is the latent heat of melting of ice. Solving the pair of equations above, the total diabatic freezing time is expressed as

$$t_D^{'} = \frac{\rho_w L_m a^2[1 - (T_0 - T_\infty)c_p/L_m]}{3f(T_0 - T_\infty)\left[k_a + L_e D_v \left(\frac{d\rho_v}{dT}\right)_{sat}\right]} \tag{6.29}$$

Following the determination of f, the diabatic freezing time was calculated using Eq. 6.29. The ratio of experimental and calculated diabatic freezing times is shown as a function of drop diameter in Fig. 6.22. The obtained mean ratio of 0.89 indicates that on average, the theoretically calculated diabatic freezing times overestimated the experimentally determined values. The diabatic freezing times estimated from Eq. 6.29 were observed to be in good agreement for experiments performed at -28 °C (dark blue dots in Fig. 6.22). For the other two temperatures -20 and -15 °C, the mismatch was larger. The few data points at -10 °C could also be represented well with the theoretical estimations. The mismatch in the diabatic freezing times could be partly attributed to the average values of the constant terms (k_a, D_v, $\left(\frac{d\rho_v}{dT}\right)_{sat}$) in the calculations for obtaining the ventilation coefficient f from τ in Eq. 6.26. For the experiments performed with the external ventilation (of 0.2 cm/s), the f values were increased from 3.26 to 3.46 for the theoretical calculations.

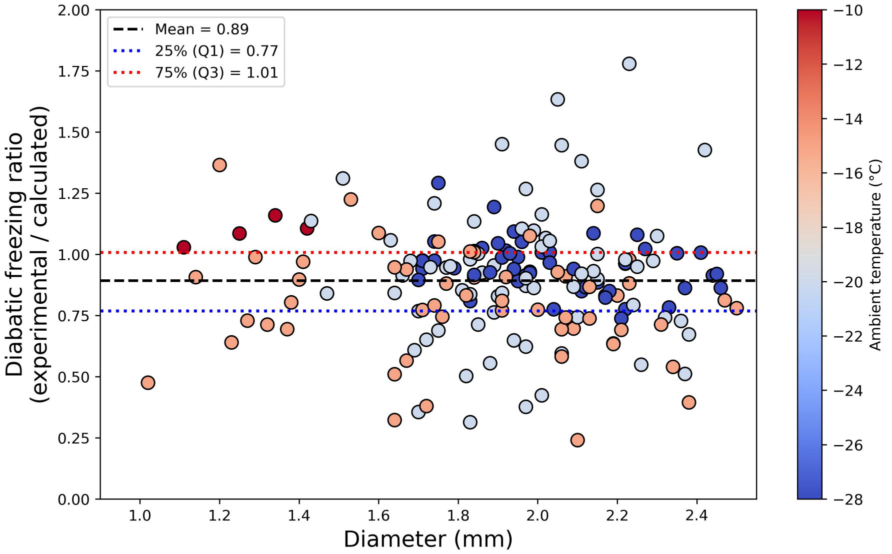

Figure 6.22: Comparison of experimental diabatic freezing time with theoretically calculated freezing time. Different colors indicate the different ambient temperatures. Orange, red, light blue and dark blue colored markers correspond to -10, -15, -20, and-28 °C ambient temperatures, respectively. The black dashed line shows the mean of the ratio of experimental to theoretically calculated diabatic freezing times. Blue and red dotted lines indicate the 25% and 75% quartiles of the shown ratio.

6.2.7 Effect of different INPs and varying solute concentrations on the freezing timescales

Effect of different INPs

This section focuses on the influence of the characteristic timescales: ice-shell formation time, adiabatic and diabatic freezing time for individual INP types (AgI, illite-NX, and feldspar), and also for AgI with dissolved NaOH. To avoid biases arising due to different ambient temperatures, only the experiments performed at -20 °C were considered for this section, which consisted of 99 drops. The results for individual INPs are summarized in Table 6.2.

The average ice-shell formation time for standalone AgI without external ventilation was found to be 68.53 ± 34.44 ms, which is about 3 times larger than the ice-shell formation time observed with both illite-NX (26.42 ± 15.96 ms) and feldspar (19.48 ± 7.44 ms). Among the different INPs, AgI nucleates at much warmer supercooling temperatures due to its high nucleating efficiency compared to the other two INPs. This resulted in slower crystal growth rates and in comparatively longer ice-shell formation times. The slower growth rates and initiation of freezing at comparatively warmer supercooling for AgI can be clearly seen. A certain influence of external ventilation could also be noted in the ice-shell formation times of

Table 6.2: Results of experiments conducted at 20 °C for different INPs.

Characteristic time	AgI	Illite-NX	Feldspar	NaOH (20 mg/L)	NaOH (60 mg/L)	AgI+Illite
Ice-shell formation (ms) - no ventil	68.53 ± 34.44	26.42 ± 15.96	19.48 ± 7.44	59.85 ± 30.15	–	51.75 ± 26.48
Ice-shell formation (ms) - ventil	63.50 ± 27.35	20.29 ± 10.08	18.20 ± 7.28	47.67 ± 12.94	36.67 ± 17.37	33.61 ± 14.92
Adiabatic freezing (s) - no ventil	0.65 ± 0.05	0.62 ± 0.22	0.68 ± 0.10	0.46 ± 0.07	–	0.56 ± 0.08
Adiabatic freezing (s) - ventil	0.54 ± 0.06	0.49 ± 0.07	0.67 ± 0.12	0.55 ± 0.15	0.54 ± 0.16	0.64 ± 0.31
Diabatic freezing (s) - no ventil	34.05 ± 4.77	23.85 ± 7.27	29.96 ± 9.12	34.82 ± 5.82	–	24.11 ± 2.70
Diabatic freezing (s) - ventil	33.85 ± 16.81	23.11 ± 3.85	31.03 ± 11.80	33.09 ± 9.01	36.78 ± 9.23	50.94 ± 19.48

the three different INPs. For the externally ventilated drops, the average ice-shell formation times decreased by 7.4%, 23.3%, and 6.6% for AgI, illite-NX, and feldspar, respectively. The number of INP particles (i.e., concentration or moles) present in a levitating drop could also be attributed to this difference in ice-shell formation times among the INPs. The molar masses (in g/mol) of AgI, illite-NX, and feldspar are: 234.79, 394.34, and 278.33, respectively. For a drop with 2 mm diameter, and considering the highest concentration of the individual INPs from Table 6.1, their corresponding number of moles are: 3.56×10^{-9}, 6.35×10^{-9} and 1.05×10^{-8} for AgI, illite-NX and feldspar, respectively. Thus, for a 2 mm raindrop, illite-NX had approximately twice the number of AgI particles, and feldspar had approximately thrice the number of AgI particles inside the drop. In light of the current experimental data, the ice nucleating efficiency as well as the molarity of the aqueous suspension were found to have a profound influence on the ice-shell formation time.

Also shown in Table 6.2 are the diabatic and adiabatic freezing times for the individual INPs. In the adiabatic freezing stage, the average freezing times were found to be the lowest for illite-NX among the three INPs, for drops with external ventilation (0.49 ± 0.07 s) and for drops without external ventilation (0.62 ± 0.22 s). The change in adiabatic freezing time was about 16.9%, 20.9% and 1.5% lower for the externally ventilated drops for AgI, illite-NX and feldspar, respectively. Similarly, illite-NX showed the shortest diabatic freezing stage of about 23 s, compared to the other two INPs. Drops with and without external ventilation revealed almost similar freezing times. The average diabatic freezing times for AgI and feldspar were about 34 and 30 s, respectively. However, unlike the ice-shell formation time, neither adiabatic nor diabatic freezing times were affected significantly due to changes in the INPs. AgI, illite-NX and feldspar were all found to have similar average adiabatic and diabatic freezing times within the standard deviations. A conclusive reasoning for the observed shorter adiabatic and diabatic freezing times for illite-NX could not be established. A possible argument might be related to the molecular structure of the individual INPs. The hexagonal structure of AgI is very similar to that of ice lattice structure, which makes it a very efficient INP (Marcolli et al., 2016). Therefore, drops with AgI as INP should have the fastest freeze times. A tetrahedral structure of microcline feldspar particles and surface defects of the crystalline plane in (100) orientation shows high affinity to the prismatic plane of ice crystals (Kiselev et al., 2017). Illite-NX has a porous multi-layered crystallographic structure, but the ice nucleating activity could be very site specific (Broadley et al., 2012). The efficiency of illite-NX can be considered the lowest and also very highly variable among the three INPs used in this study. During the experiments, illite-NX also took the longest time for initiation of freezing, sometimes more than 2-3 minutes after the drop was introduced into the acoustic field. This long freezing initiation time could act as a compensating factor for the least effective INP, in terms of freezing times. Drops with illite-NX as INP were at the supercooled stage for a longer time, and would have much faster heat dissipation during freezing, compared to the drops with other INPs. The proper extent of the dependence of crystal lattices, surface morphologies, and the nature of attached functional groups on the ice nucleating efficiency is not clearly known and provides an avenue for further research (Kanji et al., 2017).

A few experiments were also performed combining two INPs, AgI and illite-NX. This combination decreased the ice-shell formation time as compared to AgI as a standalone INP by about 24.5%. These experiments were performed initially to improve the optics of the recordings at faster frame rates (higher than 1200 fps). Standalone AgI in our experiments produced transparent ice-shells during freezing, making visual inspection of the videos cumbersome and inefficient at times. With illite-NX as INP, the frozen drops were more opaque, and visual inspection of the recordings turned out to be less challenging. However, illite-NX as a standalone INP required much lower ambient temperatures and longer supercooling, as compared to AgI. Hence, some experiments with a combination of both INPs were performed. Apart from the optical aspect, the combination of the two INPs affects the interfacial growth kinetics through their spatial distribution and the combined number of active nucleating sites. Nevertheless, a detailed study needs to be performed for different concentrations of the INP combinations and mixing proportions before stating any conclusive statements. Hence, any further comparison for the INP combination samples, besides a reduction in the ice-shell formation time, cannot be formulated with the limited state of the dataset. The results from the combinations of the INPs have been used in the previous analyses for statistical purposes.

Stuart and Jacobson (2004) considered the ice-shell formation time as the adiabatic freezing time in their drop freezing model for calculating chemical retention of dissolved solutes during freezing. From the present investigation, it was found that the ice-shell formation timescale is about an order of magnitude smaller than the adiabatic freezing time. AgI as INP showed the maximum average ice-shell formation time for experiments with no ventilation, which was less than 12.6% of its adiabatic freezing time. For other INPs, this ratio of ice-shell formation time to adiabatic freezing time was even lower.

Ventilation does seem to reduce the average ice-shell formation times and adiabatic freezing times for AgI and illite-NX. However, alongside the stochastic nature of freezing processes and high standard deviations in the freezing timescales, the true effect of external ventilation in the experiments and the current M-AL setup as a whole could not be clearly verified.

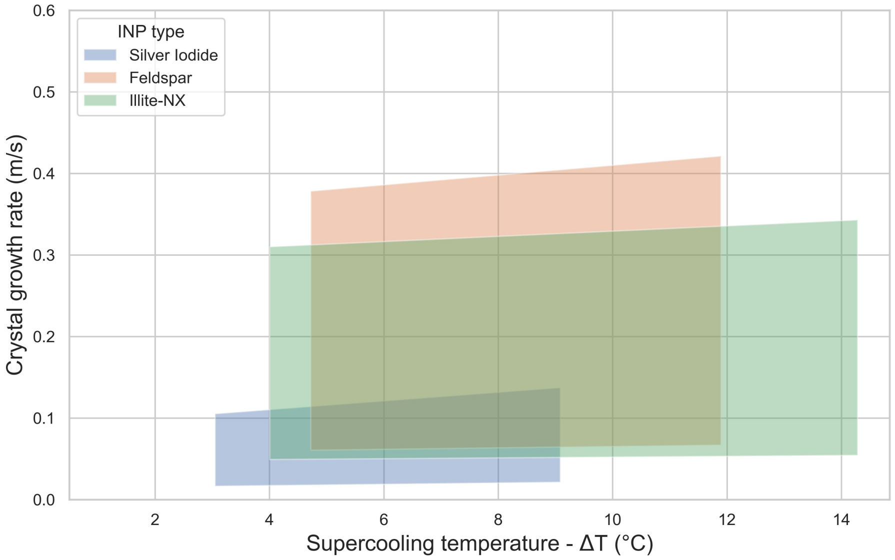

Figure 6.23: Comparison of crystal growth rates for the three INPs, observed at -20 °C ambient temperatures.

The range of crystal growth rates for standalone AgI, illite-NX, and feldspar is shown in Fig. 6.23. They were calculated from the ratio of drop circumference (upper limit) and drop radius (lower limit) to the ice-shell formation time, in a similar manner shown previously in Fig. 6.5. Mathematically, the lower limit is scaled by a factor of 2π to obtain the upper limit of the crystal growth rates. The ice crystal growth rates for the individual INPs were evaluated and plotted only for the experiments performed at -20 °C ambient temperature. The drop freezing temperatures for AgI varied from -3 to -9 °C. AgI showed the slowest growth rates and least variation in their supercooling or drop freezing temperatures. Feldspar showed the fastest growth rates among the three, and the drop freezing temperature varied between -4.7 to -11.9 °C. Drops with illite-NX showed the highest variability in their supercooling temperatures, the drop freezing temperatures ranged from -4 to -14.3 °C. Further insights and discussions on the effect of dissolved solute on freezing timescales are provided in the following section.

Effect of dissolved solutes

To investigate the effect of dissolved solutes on freezing timescales, experiments were performed by adding NaOH to the aqueous suspension of AgI. The samples were prepared with 20 and 60 mg/L concentrations of NaOH. From Table 6.2 it can be seen that ice-shell formation time reduced with increasing NaOH concentration, for both with and without ventilation cases. Only the experiments performed at ambient temperatures of -20 °C and drop sizes in the range of 2± 0.2 mm were considered in this analysis. Furthermore, the concentration of AgI was kept constant at 0.016 g/L. The final dataset for the ensuing analysis consisted of 27 frozen drops.

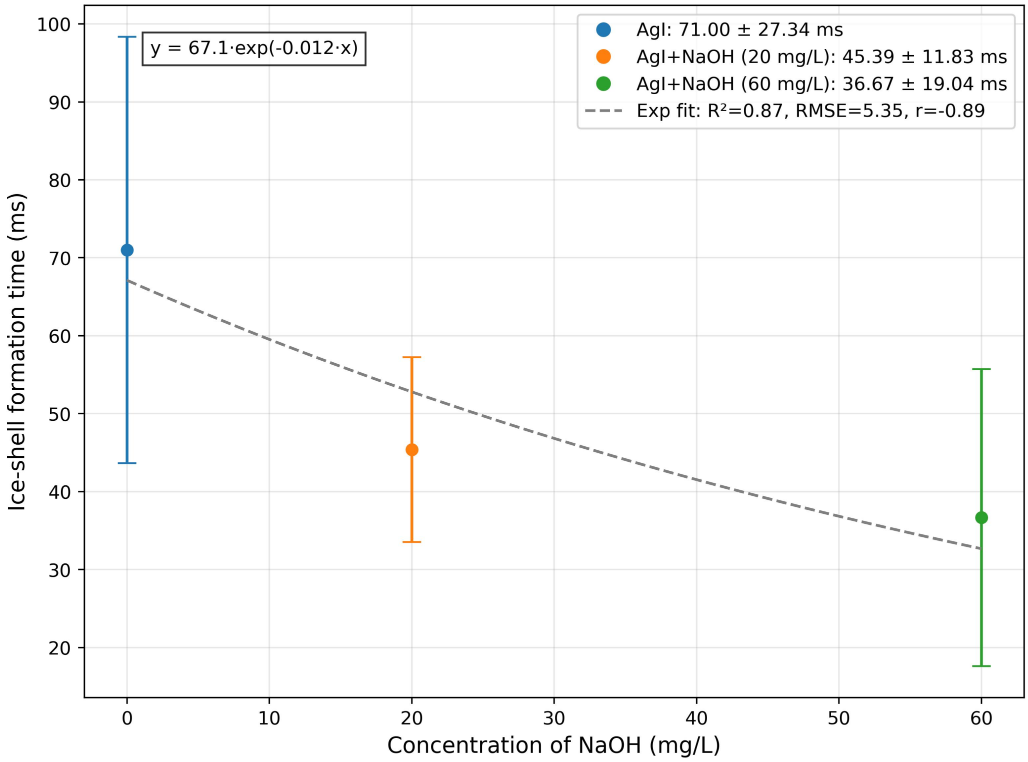

Figure 6.24: Ice-shell formation time as a function of added solute concentration.

The variation of ice-shell formation as a function of solute concentration is shown in Fig. 6.24. The average ice-shell formation time for standalone AgI was 71.00 ± 27.34 ms, for experiments with 20 mg/L NaOH, the average ice-shell formation time was 45.39 ± 11.83 ms, a reduction of about 36% as compared to standalone AgI. For experiments with 60 mg/L NaOH concentration, the average ice-shell formation time was found to be 36.67 ± 19.04 ms, which is about 48 % less from standalone AgI case. The addition of dissolved solute alongside the INP (AgI in this case) does seem to lower the ice-shell formation time in an exponential manner, as shown in Eq. 6.30, as compared to the time taken to form the ice-shell without any dissolved solutes. Pruppacher (1967) showed that dissolved salt solutions can increase ice crystal growth rates by modifying the interfacial growth kinetics, for the solute concentration interval 10^{-4} to 10^{-2} mol/L. For NaOH, the corresponding concentration interval would be 4 to 400 mg/L. Relevant to our experiments, some possible explanations for faster crystal growth rates could be: either from the enhancement of interfacial electric field at the ice-water interface during crystallization process, or increased heat dissipation rate from the sharper and thinner tips of the propagating dendritic branches for salt solution, as compared to pure water (Pruppacher, 1967). Microscopic imaging of the propagating ice fronts in our experiments was not feasible. Providing the highly polar nature of NaOH, it could be a combination of both the factors mentioned above, contributing to faster crystal growth rates (i.e., faster ice-shell formation time) observed in our experiments with dissolved NaOH. As stated previously, the best fit among the three: linear, power law, and exponential was chosen for quantifying the observed relationships. Exponential fit had the least root mean square error (RMSE = 5.35) and was chosen as the best fit. The ice-shell formation time and its dependence on the concentration of dissolved NaOH in an aqueous suspension with AgI as INP is expressed mathematically as

$$I_c = 67.10 \times e^{0.012 \times c} \tag{6.30}$$

where I_c is the solute concentration dependent ice-shell formation time (in ms) and c is the concentration in mg/L.

For calculating the retention indicator (RI) in Chapter 5, the total freezing time τ_{frz} was considered as the time taken for the formation of the ice-shell. For calculations presented in Table 5.3 in Chapter 5, freezing time $\tau_{frz} = 4.8$ ms was informed from a single observation. In the current set of experiments, the average ice-shell formation time for drops with 60 mg/L dissolved NaOH was about 36.7 ms, which is almost 8 times higher than τ_{frz}. The slightly longer ice-shell formation time for dissolved NaOH could be due to the fact that the single component retention experiments had two different types of dissolved solutes. One was the component being investigated, and the other was the concentration tracking tracer. Perhaps the interaction of different dissolved solutes affected the shell formation time even more. Aside from this speculation, the precise effect of two different dissolved substances on the ice-shell formation time cannot be clearly stated from the current results, and could be investigated in future experiments. Nevertheless, the freezing timescale consideration for the RI analysis to be in the millisecond range was correctly assigned. Even with comparatively higher values of shell formation time for dissolved NaOH, it is at least 4 orders of magnitude higher than the total solute mass expulsion times, presented in Table 5.3. The finding that the ice-shell formation time decreased with increasing concentration of dissolved solutes indicates that the high chemical retention observed during freezing of raindrops is indeed limited by the formation of an ice-shell.

The variation of adiabatic freezing time with added solute concentration is shown in Fig 6.25. Unlike ice-shell formation time, no clear trend for either increase or decrease of adiabatic freezing time with changes in NaOH concentrations was seen. The average adiabatic freezing time for standalone AgI, AgI with 20 mg/L NaOH, and AgI with 60 mg/L NaOH were: 0.59± 0.07 s, 0.52± 0.07 s and 0.59± 0.15 s, respectively. An initial decrease of 12% in the average adiabatic freezing time was seen as the concentration of NaOH was increased from 0 to 20 mg/L. However, upon increasing NaOH concentration up to 60 mg/L, the average adiabatic freezing time increased to 0.59 s, similar to that of standalone AgI, and with a much larger standard deviation. Owing to the large scatter, any mathematical relationship could not be established from the current dataset for the adiabatic freezing timescale.

Figure 6.26 shows the variation of diabatic freezing time as a function of added solute concentration. Here, a minimal overall increase in diabatic freezing time can be seen with increasing NaOH concentrations, but also with high scatter around standalone AgI. The average values of diabatic freezing time for standalone AgI, AgI with 20 mg/L, and AgI with 60 mg/L are: 37.59 ± 13.83 s, 35.79 ± 8.38 s and 40.03 ± 7.01 s, respectively. Akin to adiabatic freezing time, no mathematical expression could be proposed with the current highly variable state of the experimental data for the diabatic freezing timescale.

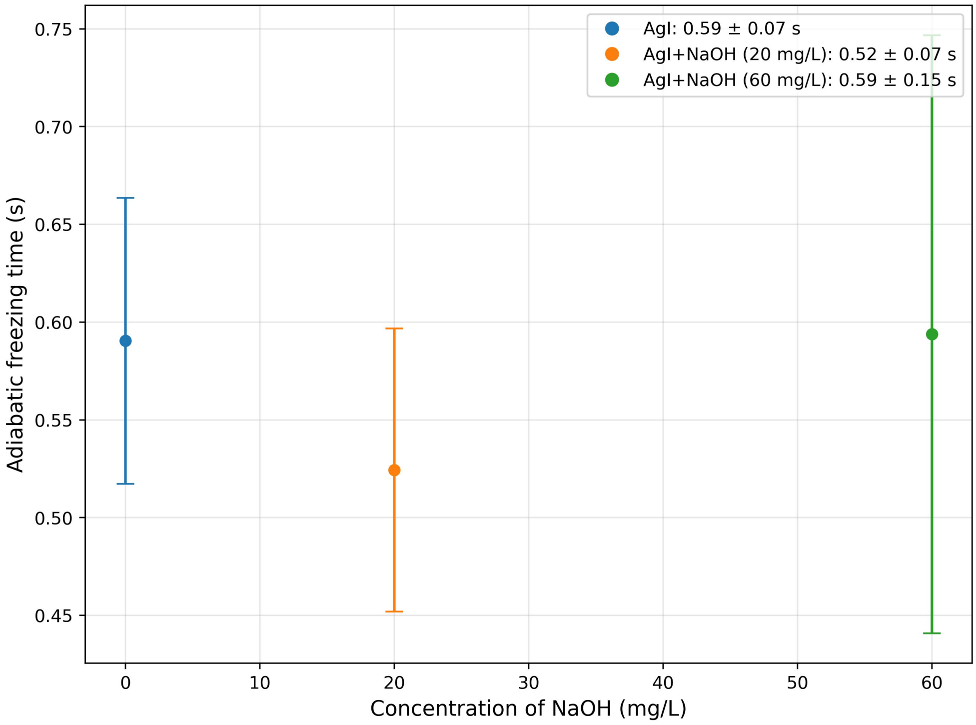

Figure 6.25: Adiabatic freezing time as a function of added solute concentration.

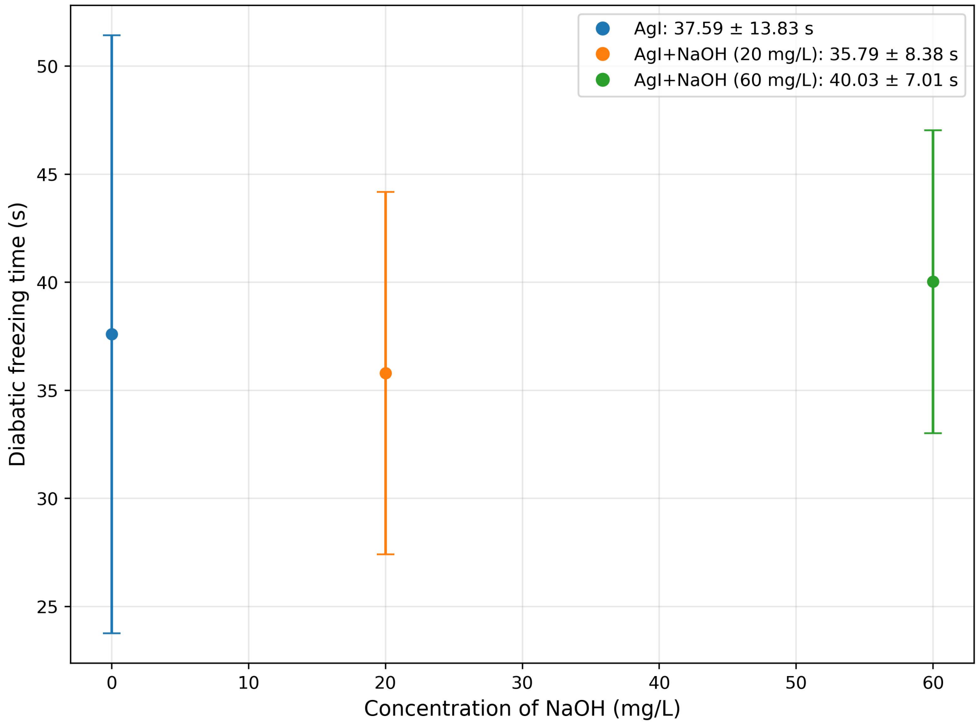

Figure 6.26: Diabatic freezing time as a function of added solute concentration.

6.3 Conclusions

Formation of an ice-shell was observed immediately after the initiation of freezing in order of tens of milliseconds, with an average value of 42.73 ms for 1.1 to 2.7 mm sized raindrops. Ice-shell formation time was found to be dependent on the drop freezing temperature, ambient temperature, drop sizes, INP concentration (molarity), and type of INPs. Lower freezing temperatures showed faster ice-shell formation time. The number of INPs suspended inside a raindrop also affected the time taken to form an ice-shell. The higher the number of INPs, the lower was the ice-shell formation time. In addition to drop freezing temperature and INP concentration, the presence of dissolved solute particles NaOH decreased the ice-shell formation time in an exponential manner. Experiments with standalone AgI as INP showed the longest ice-shell formation time among all the INPs used, due to comparatively lower drop freezing temperatures, high ice-nucleating efficiency of AgI, resulting in comparatively slower crystal growth rates after ice nucleation. Ice-shell formation time normalized with drop circumference as a function of drop freezing temperature was proposed from the experimental findings (Eq 6.3). Ice-shell formation time as a function of dissolved solute concentration was also provided (Eq 6.30) from this study.

Overall ice-shell formation time was found to be in milliseconds range. This indicates that ice-shell formation time is much faster than the solute expulsion time shown in Table 5.3, Chapter 5, by at least 4 orders of magnitude. The ice-shell would prevent any dissolved solutes from being expelled by the drop during its freezing. Thus, resulting in high retention of the dissolved substances observed in Chapter 5.

Comparing the timescales, it is evident that ice-shell formation is a part of the adiabatic freezing stage. Physically, only a small portion of the supercooled liquid freezes during the adiabatic freezing stage, and drop surface warms up due to the uptake of latent heat released during freezing. In terms of timescales, the adiabatic stage can be thought as cumulative of the time taken for the formation of the ice-shell and the time taken by the drop to distribute the released latent heat uniformly to its surface. Further investigations at a molecular and material specific level would be beneficial to better understand the heat dissipation times during the phase change from liquid to solid ice.

Chapter 7

Contributions in other projects

7.1 Retention during freezing of raindrops - Study of ambient aerosol samples

Experiments for this study were performed with M-AL setup and analysis of the data was published in:

”Seymore, J., **Gautam, M.**, Szakáll, M., Theis, A., Hoffmann, T., Ma, J., Zhou, L., and Vogel, A. L.: Retention during freezing of raindrops – Part 2: Investigation of ambient organics from Beijing urban aerosol samples, Atmos. Chem. Phys., 25, 11829–11845, https://doi.org/10.5194/acp-25-11829-2025, 2025.”

Summary of the publication:

Aim: To investigate chemical retention during drop freezing, particularly the redistribution of water-soluble organic compounds (WSOC) from aerosols, which is poorly understood but relevant to vertical transport and cloud processes in the UTLS.

Methods: Laboratory freezing experiments were conducted using aqueous extracts of Beijing PM2.5 aerosols. Single droplets were levitated acoustically at –15 °C, frozen without additional INPs, collected, and analyzed by ultra-high resolution mass spectrometry (UHRMS) to determine compound-specific retention coefficients.

Main Results: Retention coefficients of WSOC exhibited a broad, non-normal distribution up to 1 and did not follow the sigmoidal relation with Henry’s Law solubilities typically reported for cloud droplets. Compound classes behaved differently: nitro- and sulfate-substituted species showed consistently high retention, while CHO groups (e.g., sugars, organic acids, terpenoids) displayed variable values.

Conclusion: Drop freezing redistributes organic compounds in ways not captured by current models. Anthropogenic NOx and SOx products are preferentially retained, potentially reducing their transport to higher altitudes, whereas more variable CHO compounds may be redistributed in the atmosphere.

I was a significant contributor to this publication. JS and JM prepared the samples. The experiments were designed by JS, AT, MS and me. I performed the experiments with the M-AL setup. JS, JM, and AV performed the analytical measurements. JS wrote the manuscript. I, along with JS, AT, MS, JM, AV, and AT reviewed and edited the manuscript.

7.2 Retention during riming: Experiments with the Mainz vertical wind tunnel

In addition to experiments with M-AL for investigating the freezing of raindrops, Mainz vertical wind tunnel (M-WT) setup was also used as part of a collaborative study for investigating retention during riming of μm-sized cloud droplets for single substances. Results from these experiments were published in:

”Borchers, C., Seymore, J.,**Gautam, M.**, Dörholt, K., Müller, Y., Arndt, A., Gömmer, L., Ungeheuer, F., Szakáll, M., Borrmann, S., Theis, A., Vogel, A. L., and Hoffmann, T.: Retention of α-pinene oxidation products and nitro-aromatic compounds during riming, Atmos. Chem. Phys., 24, 13961–13974, https://doi.org/10.5194/acp-24-13961-2024, 2024.”

Summary of the publication:
Aim: To investigate chemical retention during rime freezing, a key process in graupel and hail formation, and to determine how organic compounds are redistributed between ice and gas phases, affecting their transport to the upper troposphere.

Methods: Experiments were conducted in the Mainz vertical wind tunnel under dry and wet growth conditions and varying pH. Retention coefficients were measured for several atmospherically relevant organics, including cis-pinic acid, cis-pinonic acid, (−)-pinanediol, and various nitrophenols.

Main Results: Retention coefficients of the tested compounds showed a dependence on the effective Henry’s law constant (H*), consistent with earlier findings for inorganic and small organic molecules.

Conclusion: The established correlation between retention and solubility (H^*) extends to more complex organic molecules, suggesting that retention behavior during rime freezing can be generalized beyond small species, with implications for modeling organic redistribution in clouds.

I was a significant contributor to this publication. The wind tunnel experiments were designed and performed by CB, JS, KD, YM, AA, LG, AT, AV, TH, and me. CB wrote the manuscript. I, along with JS, AT, MS, AV, and TH, reviewed and edited the manuscript.

Chapter 8

Precision (or lack thereof)

8.1 Uncertainties in immersion freezing experiments

Here, the possible sources of error in the measurements and analyses, which could potentially introduce biases altogether, if any, are discussed. In the immersion mode of freezing, immersed INPs remain in an aqueous suspension. The probability of freezing depends highly on the number density of INPs present per volume of the levitating drops. The larger the number of particles inside a drop, the greater the probability of freezing. AgI in its aqueous suspension form tends to agglomerate and sediment when kept idle for sometime, in between measurements. Due to this reason, while injecting a drop inside the levitator, through a syringe, the bottom part of the syringe near the needle, was often seen to have higher concentration of AgI than at the top part. Utmost care was taken to keep the aqueous suspensions inside the syringe as uniform as possible, with the help of a magnetic stirrer, and also by manually shaking the syringe before injecting every drop. However, over time, as the experiments continued and volume of aqueous suspension in the syringe reduced, the exact INP concentration of the levitating drops might vary slightly, leaning towards marginally low concentrations. The wide temperature range seen in the frozen fraction plots could be partly attributed due to this phenomenon.

When discussing uncertainness, the accuracy ranges of the measuring instruments also should also be considered. Prolong exposure of the infrared thermometer at the lower ambient temperatures (below -20 °C) also affected the accuracy. Timely calibration checks were performed to ensure that the measurements were not affected by any instrumentation biases. Maintaining uniformity of the acoustic field at cold temperatures, was also one aspect, that needs to be considered. Icing of reflector plates were observed to disrupt the acoustic field, and introduce large variability in the recorded temperatures, and should be checked very frequently. Owing to these not so easily quantifiable uncertainties, a ± 10% of the data from the frozen fraction and INAS density plots were removed.

For the MMT particles, their layered crystalline structure resulted in more stable aqueous solutions. However, due to their poor ice nucleating ability compared to AgI, a wide variation in their freezing temperatures could be seen.

Another source of uncertainty could be introduced by the presence of pre-existing INPs in the water, used for preparing aqueous suspensions. Szakáll et al. (2021) shows that background frozen fraction spectra from purified water could also affect the observed frozen fractions, for the M-AL setup. This background spectrum would be applicable for drop freezing temperatures lower than 253 K (21 °C). For freezing experiments performed with AgI, the background frozen fraction spectra could be neglected as all the drops froze at temperatures warmer than 260 K (13 °C) for the investigated concentrations. However, for experiments with MMT, the background frozen fraction needs to be considered if the frozen fractions are, for some reason, extrapolated to lower temperatures. From their experiments with M-AL setup, Szakáll et al. (2021) show that a temperature correction factor of 0.05 units could be introduced to the overall frozen fraction, for drop freezing temperatures lower than 253 K.

8.2 Uncertainties in retention experiments

The first facet in this category is related to the desorption corrections, as the final results revolve around the correction for desorption during freezing. As mentioned in Section 5.2.3, firstly, the initial retained fraction (R_i) with dissolved chemical substances was measured, with AgI as INP to initiate freezing. Subsequently, quantitative analysis of those substances was done to infer how much of them was retained during freezing. Following this, to correct for any desorption, the same measurement and analysis process (Section 5.2.3) was repeated, but without the addition of AgI. Desorption measurements were performed at -15 °C cold-room temperature, which corresponds to $-3.9 \pm 0.3\,^{\circ}$C drop freezing temperature.

Desorption mostly happens at warm temperatures, and by lowering the temperatures beyond -15 °C, desorption would play a negligible role. Colder temperatures would essentially slow down the reaction kinetics for desorption to be effective (Mitra and Hannemann, 1993; Seinfeld and Pandis, 2016). Furthermore, the low surface area to volume ratio for the case of the raindrops, is another indicator of lower overall desorption as well (Jost, 2017). Consequently, the desorption corrections measured at $-3.9 \pm 0.3\,^{\circ}$C drop freezing temperature were applied to each of the measured substances. Also, from previous experimental retention measurements from von Blohn et al. (2013) and Borchers et al. (2024), it can be confirmed that there is not much desorption at very cold temperatures, and hence desorption correction factor should not ideally create any major errors or biases in the results.

For each investigated substance (for single components and binary mixtures), 11 data points were measured. The retention coefficient presented here is the average of those 11 data points, and their corresponding standard deviations represent the individual error ranges. The overall measurement error for retention coefficients was calculated with the help of the multiplicative theory of error propagation (Lindberg, 2000) for both the numerator and denominator in Eq. 5.3. It was seen that, except for acetic acid (both as single components and binary mixture measurements), the overall error was below 10 % for almost all other substances. The higher error in acetic acid quantification arose mostly due to bad peak quality for its chromatogram, and consequently, further sensitivity studies involving acetic acid in its binary mixture form (Mixture A1) have not been done. There could be some fluctuations arising from the instrumentation due to minor differences in the retention time of the same chemical species when they pass through the mobile phase of the detection column. However, these fluctuations were addressed in the standard deviation and final error propagation calculations in the results.

Furthermore, errors in measured retention coefficients could be possible from the dissociation of substances, especially for pH sensitivity studies. pH of the solutions was altered by adding hydrochloric acid (HCl) to lower the pH and sodium hydroxide (NaOH) to increase the pH. HCl and NaOH can also interact with the investigated substances and dissociate them into their ionic form. In this case, the overall concentration of the investigated substances could be lowered, and a lower concentration of substances might not have enough partial pressure in the liquid phase (inside the levitated drops before freezing) for them to be expelled from the drop when it freezes. If the initial liquid phase concentration were to decrease by more than an order of magnitude, this could result in essentially higher retention and perhaps create a bias in our measurements. However, even after the addition of HCl or NaOH to alter the pH of the solution, the initial concentration of 20 mgL^{-1} for all the investigated substances did not change much. After addition, the lowest measured initial liquid phase concentration was 17.8 mgL^{-1} (11% decrease). The total number of moles of the dissolved substances had the same order of magnitude as their initial liquid phase concentration in the solution. Thus, any significant source of biases towards a higher retention coefficient, due to the addition of HCl or NaOH, can be neglected in our measurements. All the same, both instrumentation and personal biases should not be completely ignored, even with utmost precautions. High standard deviations for measurements concerning acetic acid and 2-nitrophenol are a testament to this fact.

8.3 Uncertainties in high-speed freezing experiments

For experiments with high-speed freezing of raindrops, the first consideration is the analysis of the ice-shell formation time from the recordings. Specifically, for experiments with AgI as an INP, some recordings showed a sort of transparent shell formation. Improving the optics helped in mitigating this source of error to some extent. However, some uncertainties could still persist. For such transparent shell formation recordings, locating the initiation of freezing was tricky. Cases where the uncertainty in the start and end of shell formation exceeded 10% of the recording frame rate were excluded from the final analyses. If a maximum error of ± 10% is considered in evaluating both the start and end of freezing, a cumulative error of 20% could be expected in the final results. Ice-shell formation times were presented as the mean and one standard deviation throughout this dissertation. The high standard deviation (see Table 6.2) seen for standalone AgI could be partly attributed to this lack of complete clarity for the start and end of shell formation, along with the random nature of the freezing process. For better optics in the recording, polarizing filters were tested as well. However, the polarizing filters reduced the light intensities reaching the high-speed camera significantly, for frame rates higher than 500 fps, and were discarded later on.

Illte-NX was initially added to AgI for improving the optics. However, only a handful of experiments were performed with the combination of these two INPs. The freezing curves and INAS densities were not analyzed within the scope of this work. A multi-component singular approach (Murray et al., 2012; Vali, 2014) could provide a better insight into their interaction and freezing characteristics. To design a separate set of experiments for that purpose was beyond the objectives of this work. Regardless, the ice-shell formation times, diabatic and adiabatic freezing times were included for the analyses. Freezing experiments with illite-NX, feldspar, and AgI with NaOH provided clearer shell formation images.

Disturbances in the acoustic field also affected the levitated drops during the experiments. These oscillations mostly arose due to (a) thermal instability of the ultrasonic power source upon long exposure in the cold working environment, (b) deposition of ice on the reflector plate, (c) increasing the ventilation around the levitated drop, (d) sometimes completely random fluctuations, and also a combination of (a) and (c). Analysis of the data for unstable and oscillating drops was found to affect the diabatic freezing time greatly, compared to ice-shell formation and adiabatic freezing time. Highly unstable and oscillating drops were not included in the final analysis. These issues (a and b) were also faced during retention experiments, but to a lesser extent as compared to high-speed freezing experiments here. Also, the presence of a mass tracking tracer in the retention measurements helped mitigate such issues effectively.

In addition to oscillations, the acoustic field trapped tiny ice particles, which at times went undetected in the field of view of the camera. These trapped ice particles were observed to have initiated the freezing of the levitated drops at times, providing a classical example of contact freezing instead of the immersion mode of freezing. Utmost care needs to be taken for such incidents, as they can incorporate biases in the drop freezing temperature and the subsequent freezing timescales. Diabatic freezing times for these contact freezing events were not much affected, but the ice-shell formation and the adiabatic formation time for the contact freezing cases showed a lot of variation. Especially if the contact from external ice particles occurred at warmer supercooling temperatures (less than 3 °C). Such recordings were only a handful and were excluded from the analysis. Similar to the previous section, errors arising due to instrumentation calibration, sizing of the drops, and observer biases in scanning through more than 200,000 images could lead to potential sources of error. Recordings with higher than 5% uncertainty for locating the start and end of freezing were meticulously reviewed before including them in the final analyses.

Besides the experimental side of things, uncertainties arising from the numerical estimations of freezing timescales should also be considered. The theoretically derived adiabatic freezing time is highly dependent on the intrinsic kinetic coefficient (k_{int}). Internal kinetics of a freezing front would vary for different INPs, as their molecular alignment in water varies. Our results did not reveal a statistically significant dependence of adiabatic freezing time on supercooling or drop freezing temperature. Hence, the term k_{int} was applied to obtain a temperature independent relation for estimating the adiabatic freezing time. In retrospect, k_{int} is sensitive to both temperature and impurities present in the solvent, i.e., water. For pure water, the intrinsic kinetic coefficient would be much higher than the average value of 7×10^{-6} ms−1K−1, and would decrease with increasing level of impurities in the water. Such a decrease would lead to longer adiabatic freezing time.

Similarly, estimation of diabatic freezing time also possesses the ability to introduce errors and uncertainties. As mentioned earlier, the terms in Eq. 6.29: k_a, D_v, and $\left(\frac{d\rho_v}{dT}\right)_{sat}$ are averaged values for T_∞ = -20 °C. Ventilation coefficient f, derived from relaxation time τ, was calculated (using Eq. 6.26) from a point measurement for a drop freezing at -20 °C. A tiresome but more accurate approach would be estimate τ and subsequently f for each of the frozen drops. In terms of magnitude, f values are at least 2 orders of magnitude higher than the other uncertain parameters k_a, D_v, and $\left(\frac{d\rho_v}{dT}\right)_{sat}$. Uncertainty introduced from f would be more significant than the terms. From Eq. 6.29 we can see that any uncertainty for f would scale linearly for diabatic freezing time, $t_D^{'}$. Collectively, a simple quantification can be seen in Fig. 6.22, where the mean of the ratio of experimental to calculated diabatic freezing time is about 11% less.

Chapter 9

Summary and Outlook

The works presented in this dissertation can be summarized in three major sections: the first section involves immersion freezing characteristics of a certain common INP - AgI, and rather uncommon INPs - doped MMT (objective - O1). The second section is focused on the retention of dissolved chemicals in aqueous solution during freezing of raindrops (objective - O2). Objectives - O4 and O5 were carried out as part of collaborative work, and they are outlined in the second section. The third section is the investigation of drop freezing timescales and their associated microphysical aspects (objective - O3).

9.1 Immersion freezing of raindrops

Immersion freezing experiments were performed with mm sized raindrops, using an acoustic levitator setup inside a walk-in cold room facility. The raindrops were produced from purified aqueous suspensions with ice nucleating particles (INPs) immersed in them.

The immersion freezing experiments presented in Chapter 4 were aimed at characterizing silver iodide (AgI) as INP, which was used for the majority of the work presented in this thesis. AgI was successfully characterized at three different ambient temperatures and at three different concentrations (Fig. 4.1). The ice nucleating active site (INAS) density as a function of temperature (Fig. 4.2) was determined. The median drop freezing temperatures for ambient temperatures of -15, -20, and -28 °C and corresponding AgI concentrations of 0.2, 0.01, and 0.0003 g/L were found to be -3.9, -6.7, and -8.9 °C, respectively (Table 4.1).

Similar to AgI, chemically treated montmorillonite (MMT) samples were also characterized with the same setup. The MMT samples went through a cation exchange procedure, where the predominant Na^+ ions in the commercially available Swy-2 MMT powder were replaced with different cations. Ion exchanged MMT samples showed lower median freezing temperatures compared to purified MMT powder, lowest for Cesium doped MMT. Overall it was found that the ice nucleating ability for the doped MMT samples were reduced as compared to pure MMT samples. These results encourage to further investigate this somewhat underexplored aspect of ice nucleation, including both theoretical and modeling studies, in understanding its overall impact on the atmosphere.

Objective O1 - characterizing immersion freezing experiments with different INPs was achieved in this section. Results from the immersion freezing experiments performed with AgI has been published in Gautam et al. (2025), shown in Appendix A.1.1. Results from the immersion freezing experiments with doped MMT samples have not been published yet.

9.2 Chemical retention during freezing

In experiments with the acoustic levitator setup, using previously characterized AgI as INP, the retention of several species during freezing of 2 ± 0.1 mm drops was investigated. Chemical retention of nitric, formic, acetic acids, and 2-nitrophenol were studied as single components. Furthermore, the combination of formic acid with nitric acid, and formic acid with 2-nitrophenol were studied as binary mixtures to determine how the differential incorporation or segregation of two substances impacts their chemical retention. Retention experiments were performed at different pH levels (3 to 7) and at different drop freezing temperatures (-3.9 ± 0.3 °C and -6.9 ± 1.1 °C).

From our results, it was concluded that most of the substances are fully retained, with retention coefficients R close to or equal to 1 (Table 5.2). We did not observe the previously reported sigmoidal dependencies on the effective Henry's law coefficient H^* (Fig. 5.4). This indicates that for raindrops, the physical properties such as drop size and ice-shell formation during the freezing process supersede the previously informed dependence on inherent chemical properties such as H^* for cloud droplets (von Blohn et al., 2011, 2013; Jost et al., 2017; Borchers et al., 2024). An ice-shell is formed within milliseconds during the initiation of freezing and acts as a limiting factor for dissolved substances to be expelled from the drop. As a single component, acetic acid and 2-nitrophenol showed sensitivity to pH and temperature; acidic conditions and lower temperatures slightly affected higher retentions (Fig. 5.2 and 5.3). In contrast, formic acid as a single component did not show any sensitivity to either pH or temperature. Following a similar trend as formic acid, the binary mixtures also did not show any pH or temperature sensitivity, and substances were completely retained in their mixture form.

We performed a timescale analysis of our experimental results via the retention indicator (RI). The solute mass expulsion timescales were found to be at least 5 orders of magnitude higher than the corresponding freezing timescales. For formic acid and 2-nitrophenol, the aqueous phase expulsion time was the controlling factor, whereas for nitric and acetic acid, the gaseous phase expulsion time was found to be the controlling factor for higher RI values. As such, we provide an updated fit for mapping RI to the R values, which now includes both μm sized cloud droplets and mm sized raindrops.

An interpretation of our results is that during freezing of raindrops, any dissolved substances would be most likely entirely scavenged by precipitation. We provided new parameterizations for the retention indicator applicable for computational studies concerning retention of trace gases to extrapolate from μm to mm size ranges.

Be that as it may, some caveats indeed need to be specified for such experimental studies. Firstly, the data set for the investigated species can be expanded by further investigating substances with H^* between 10^3 and 10^7, which was the range for H^* values showing sigmoidal dependencies between H^* and R in the case of smaller cloud droplets. One needs to keep in mind that, in addition to drop sizes, the freezing pathways were also different for previously investigated cloud droplets. Secondly, aspects such as ventilation, differences in drop freezing temperatures and experimental temperatures, the possibility of secondary ice formation due to splitting or cracking of the drops during freezing, effect of dissolved solutes on freezing timescales need to be investigated.

Another interesting venture would be investing in the retention of binary or tertiary mixtures for cloud droplet sizes. In addition to this, research and experiments (both μm and mm size ranges) involving ambient air sampled from different vertical profiles could shed light on their chemical compositions and also help us understand their chemical retention. Finally, modeling studies explicitly involving chemical retention could be used and improved upon with recent experimental findings, in order to better understand the interlinked microphysical and chemical processes occurring during chemical retention. In addition to a numerical drop model study for chemical retention, a box model approach can be used in existing convective transport models to verify observational case studies and the experimental results collectively.

The second objective (O2) of this dissertation, to investigate the chemical retention of trace gases during freezing of raindrops, was achieved and has been published in Gautam et al. (2025), shown in Chapter 5. In the fourth objective (O4), chemical retention of aromatic nitrophenols and α-pinene oxidation products for μm sized cloud droplets was investigated in the vertical wind tunnel setup, which has been published in Borchers et al. (2024). Objective - O5 was performed by investigating aqueous filter extracts of ambient air samples for retention of water soluble organic compounds, using the M-AL for raindrops, has been published in (Seymore et al., 2025). Objectives O4 and O5 were performed as collaborative research, and concise versions of both these studies have been summarized in Chapter 7.

9.3 Fast dynamics of freezing raindrops

The finding that ice-shell formation was a major contributor for observed high chemical retention for the investigated species led us to investigate further the freezing timescales. This work was designed to delve deeper into the ice-shell formation time, adiabatic and diabatic freezing times, for different INPs (AgI, illite-NX, and feldspar) and also at different dissolved solute concentrations (NaOH) besides the INPs. Additionally, an attempt was made to study the effect of external ventilation and its influence on the freezing timescales. The size range of the drops was broadened from 1.1 - 2.7 mm.

An interesting observation was the formation of ice-shell immediately after the initiation of freezing, rather than after completion of adiabatic freezing, as reported in the literature, e.g., Lauber et al. (2018). Comparing the timescales, ice-shell formation can be considered as a part of the adiabatic freezing stage. Ice-shell formation time was observed and considered (in the analysis) to be completed once the propagating ice crystals encompasses the entire circumference of the drop. The ice-shell formation time and crystal growth rate has been used analogously for comparing ice crystal growth rates from previous studies (Pruppacher and Klett, 2010). Unlike Stuart and Jacobson (2004), the ice-shell formation time and adiabatic freezing time were not similar: adiabatic freezing time was found at least one order of magnitude higher. If the entire size range and all INPs combined together are considered, the average ice-shell formation time was found to be 42.73 ms for a total of 274 frozen raindrops. Ice-shell formation depends on the drop freezing temperatures, concentration(molarity) of INPs, and also on dissolved solute concentrations. Low drop freezing temperatures led to faster shell formation. Increased concentration of INP and also dissolved NaOH lowered the shell formation time. Among the INPs, for experiments without external ventilation and at -20 °C, standalone AgI without NaOH had the highest average ice-shell formation time of 68.53 ± 34.44 ms, followed by illite-NX with 26.42 ± 15.96 ms and feldspar showing least ice-shell formation time of 19.48 ± 7.44 ms (Table 6.2). Addition of 20 mg/L NaOH to AgI decreased the average ice-shell formation time to 59.85 ± 30.15 ms. Overall, no significant effect of ventilation could be seen in our experiments. This originates from the fact that very minimal external ventilation could be applied without disrupting the highly sensitive acoustic field of the levitator setup. Due to such minimal effects, the mathematical equations formulated from the analysis considered both the ventilated and the non ventilated drops collectively.

Adiabatic and diabatic freezing timescales were also investigated during the freezing of the levitated drops. Observed average adiabatic and diabatic freezing times were 0.6 and 30.86 s, respectively. Adiabatic and diabatic freezing timescales were found to be significantly dependent on the drop sizes and ambient temperature. Larger drop sizes and warmer ambient temperatures lead to longer adiabatic and diabatic freezing times. Variation in ambient temperatures showed a stronger correlation for diabatic freezing time as compared to the freezing time for the adiabatic stage. The adiabatic and diabatic freezing times normalized with drop surface area showed stronger correlation with ambient temperatures. Effects of different INPs and concentration of dissolved NaOH showed large variation in the adiabatic and diabatic freezing times. The added concentration levels (20 and 60 mg/L) were perhaps too low to observe any statistically significant trend.

A size dependent analysis of the three freezing timescales was performed for the subset of 2 ± 0.2 mm drop sizes (Appendix A.2.1). The average values for ice-shell formation time decreased slightly, as compared to the entire size range of 1.1 to 2.7 mm. However, adiabatic and diabatic freezing time revealed similar average values. The general form of dependencies on drop freezing, ambient temperature, and drop sizes remained the same for the three timescales, for the size dependent dataset. Additionally, diabatic freezing time showed significant linear dependence on drop freezing temperatures for the 2 ± 0.2 mm drop sizes.

Evidence for secondary formation due to splitting or cracking was meticulously looked at, but without any success. The internal pressure built up inside the ice-shell was around 85 bar, much lower than the 100 bar threshold suggested in Kleinheins et al. (2021). The internal pressure was not strong enough to rupture the ice-shell for liquid or ice particles to be ejected during its freezing. As the supercooled drop froze and solidified, protrusions in the vertical direction were seen. Due to the temperature difference between the drop surface and environment, these protrusions were sometimes seen to melt and refreeze immediately on the surface of the drops (Fig. 6.3). Moderate-sized raindrops with low ventilation could perhaps be considered as an upper size bound for secondary ice production pathways during freezing of raindrops.

Theoretical estimations of adiabatic freezing time shed light on the importance of the parameter intrinsic kinetic coefficient on the freezing rate. A thorough and detailed investigation of the adiabatic freezing process and associated internal kinetics on a molecular level could improve our understanding of material and INP specific freezing timescales. Similarly, numerical estimation of diabatic freezing also revealed the significance of accurate evaluation of ventilation coefficients, in order to properly understand the heat and mass transfer processes during freezing. Acoustic levitated drops were seen to have significantly lower ventilation around them as compared to naturally falling raindrops in the same size range (Pruppacher and Klett, 2010). A fluid dynamical approach suggested by Yarin et al. (1998) and Wakata et al. (2024), especially for acoustically levitated drops, could be considered in future studies to resolve and understand some of the discrepancies in freezing timescales.

Further investigating the effect of ventilation on the ice- shell formation and other timescales should be considered in future studies. Experimental or theoretical studies conducted to relate ice-shell formation time and added solutes with different molecular structures, and with different binding efficiencies with ice lattice, would be insightful. Improvements could also be done with recording aspects of the experiment, such as the use of a thermal camera with very high frame rates, and optical arrangements dedicated to such high speed recordings. With advances in imaging technologies, a 3-dimensional recording apparatus could provide insightful information for such fast freezing events. With the current setup, only a 2-dimensional image or video can be recorded. The use of two cameras was aimed at resolving this issue to some extent. For freezing events that initiated from the backside of the drop relative to the camera lens, locating the precise initiation of freezing was a tedious task. Such experimental studies would be more fruitful and perhaps more informative if theoretical modeling of the processes went hand in hand. One such possibility would be to look at the observed freezing dynamics via a classical two-phase Stefan problem for spheres (McCue et al., 2008), which is used to treat such phase-boundary problems by considering a unidirectional heat flow during freezing (or melting). Recent studies report investigating these phase transition issues for understanding the evolution of cloud droplet lifetime and temperature and using the COMSOL Multiphysics software application (Roy et al., 2024). These approaches, perhaps, could be further applied for delving into the freezing dynamics for drops in mm sizes as well.

The third objective of this dissertation (O3) was carried out and described in Chapter 6. Preliminary results from high-speed freezing experiments were published as an appendix in Gautam et al. (2025), shown in Appendix A.1.2. The majority of the results shown in this section have not yet been published.

Appendix A

Appendix

A.1 Appendix for Chapter 5

A.1.1 Appendix A: Characterization of INP

Freezing of levitated drops

To characterize the INP (AgI) we levitated drops and recorded their drop surface temperature as they froze, at three pairs of different concentrations and cold room temperatures: 0.2, 0.01, and 0.0003 g/L, and corresponding cold room temperatures of -15, -20, and -28°C. For both combinations of concentration and temperature, the freezing profiles of about 50 drops were recorded. The crucial information derived from these three sets of measurements was obtaining the freezing profiles of the levitated drops during their freezing. Figure A.1 shows a typical drop freezing profile as the temporal evolution of the drop surface temperature. The drop when injected to the nodes of the standing wave, had initially a temperature higher than 0°C. The warm drop underwent gradual and uniform cooling and reached a supercooled stage (0 to 20 seconds). The supercooled stage continued until nucleation was initiated, where the rapid crystal growth started (about 25 seconds) and drop surface temperature rose sharply to about 0°C. The rapid crystal growth can be interpreted as adiabatic freezing and the corresponding temperature was taken as the freezing temperature of the drop. At this temperature, the supercooled drop entered an ice-water equilibrium, visible as the flattened section in Fig. A.1 (30 to 80 seconds). During this stage, transfer of latent heat took place that can be interpreted as the diabatic freezing of the levitated drop. The supercooled drop then underwent a phase transition from liquid to solid state. Finally, the drop surface temperature cooled down to ambient temperature, reaching a steady state (100 seconds) once it was completely frozen.

Frozen fraction

Within the range of the sample size of 50 drops for each set of frozen fraction measurements, the precise drop freezing temperatures varied. We grouped the recorded drop freezing tem-

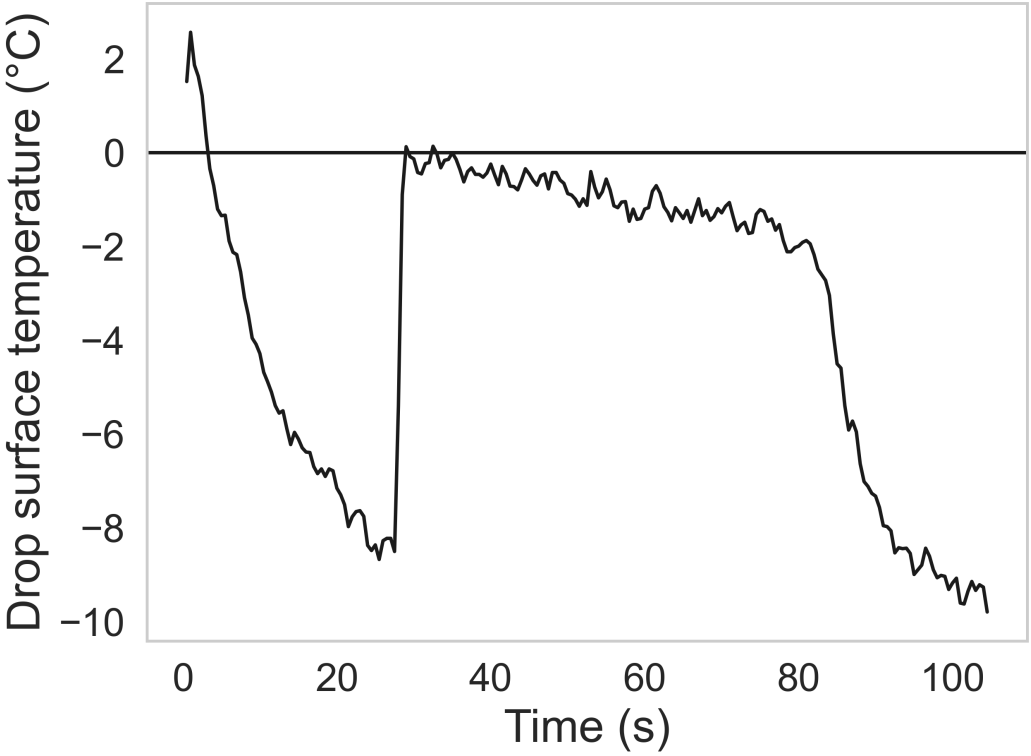

Figure A.1: Evolution of drop surface temperature during its freezing as measured by the infrared thermometer.

peratures in bins with a width of 0.5 °C. Corresponding to each bin, the number of frozen drops at each interval were grouped. A cumulative distribution was formed with the grouped bins. As commonly used in ice nucleation studies, frozen fraction or f_{ice} was determined, which is calculated as the fraction of total drops that were frozen at a particular temperature (more details in Szakáll et al., 2021). The temperature at which f_{ice} was 50% was taken as the 'median drop freezing temperature' for each set of concentration and cold room temperature pair.

The frozen fractions for each set of measurements are shown in Fig. A.2. The average drop freezing temperature was -3.9°C for AgI concentration of 0.2 g/L and cold room temperature of -15°C. For the combination of 0.01 g/L and -20 °C, the average drop freezing temperature was -6.7 °C and -8.9 °C for the combination of 0.0003 g/L and -28°C. We conducted our retention measurements at a cold room temperature of -23°C. To obtain the freezing profile at this temperature, we refitted the freezing profile obtained for -20°C using the following equation:

$$f_{ice\_23} = 1 - \exp \frac{c_{23} * \ln(1 - f_{ice\_20})}{c_{20}} \tag{A.1}$$

where f_{ice_23} is the desired frozen fraction distribution at -23°C. c_{20} and c_{23} are the INP

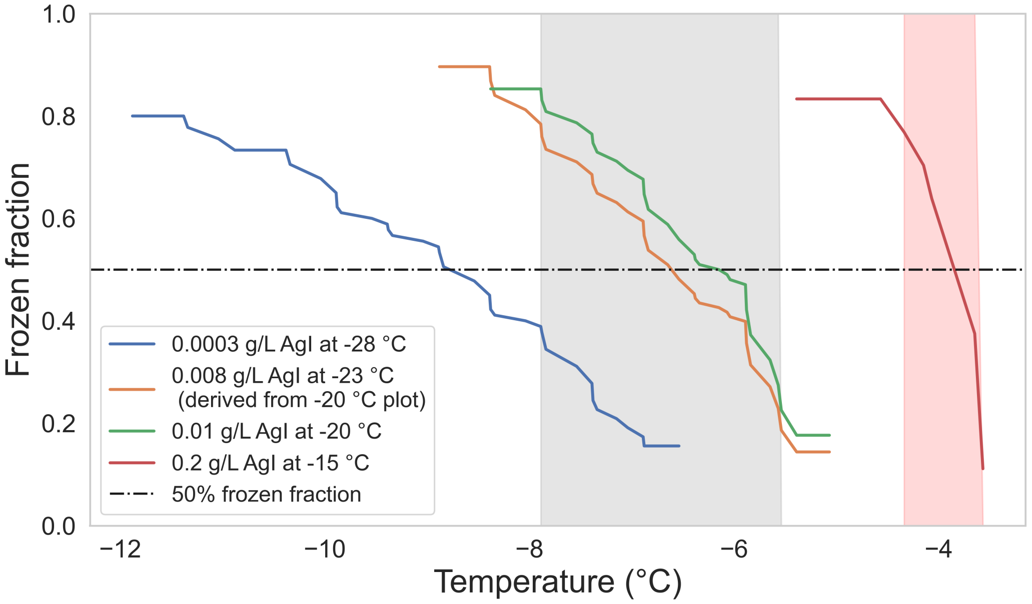

Figure A.2: Frozen fraction at different ambient temperatures and concentrations of AgI. Shaded regions mark the two selected temperature ranges for retention measurements. The shaded regions lie within the interval where the frozen fraction is in between 0.8 and 0.2.

concentrations at the two different temperatures of -20°C and -23°C, respectively. f_{ice_20} is the experimentally derived frozen fraction at -20°C. The cooling rate of the drop surface temperature was practically identical at these two cold room temperatures. Equation A.1 is adopted from the relation between ice nucleation active sites (n_s) and f_{ice} and at a particular INP concentration and temperature (see Szakáll et al., 2021, Eq 5).

We selected the interval where frozen fraction lies between 20% to 80% as the temperature deviation during our retention experiments. Shaded regions in Fig. A.2 show this temperature deviation for experiments done at -15°C and -23°C cold room temperatures. The average drop freezing temperatures (frozen fraction at 50%) in these two cases were $-3.9 \pm 0\,3°C$ (red-shaded region) and $-6.9 \pm 1\,1°C$ (gray shaded region).

A.1.2 Appendix B: Ice-shell formation during freezing

The investigation of the drop freezing mechanism in the acoustic levitator led to the realization of the ice-shell formation. During the rapid crystal growth stage within the first 25 s, as discussed in Appendix A.1.1, Fig. A.1, an ice-shell formed around the supercooled drop within milliseconds (Fig. A.3). After the formation of the shell, freezing inside the drop proceeded gradually until it was completely frozen. The shell formation process was recorded with a high speed camera setup at 600 frames per second, and at a cold room temperature of -15 °C.

This observation validates the higher retention coefficients of the substances measured during our freezing-retention experiments, as compared to the previously measured sub-

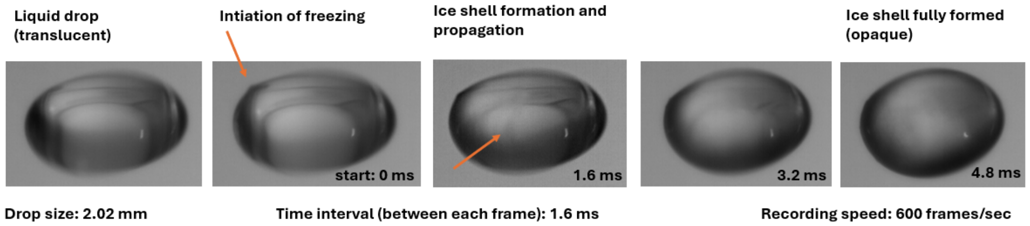

Figure A.3: Consecutive frames showing the formation of ice-shell, recorded with a high speed camera at 600 frames per second, and at a cold room temperature of -15 °C. In the liquid phase (leftmost image), the drop is seen as translucent, which gradually turns opaque as the ice-shell is formed (rightmost image).

stances involving riming-retention. The ice-shell inhibited the expulsion of the dissolved chemical substances from the drop. The expulsion timescale as discussed and calculated in Section 5.3.5 was several orders of magnitude higher than the freezing time scale of 4.8 milliseconds (Fig. A.3). This led to a higher value of the retention indicator, even for more volatile substances such as 2-nitrophenol, which had the lowest effective Henry's law constant among the investigated substances (Figure 5.5 and Table 5.3).

A.1.3 Supplementary information

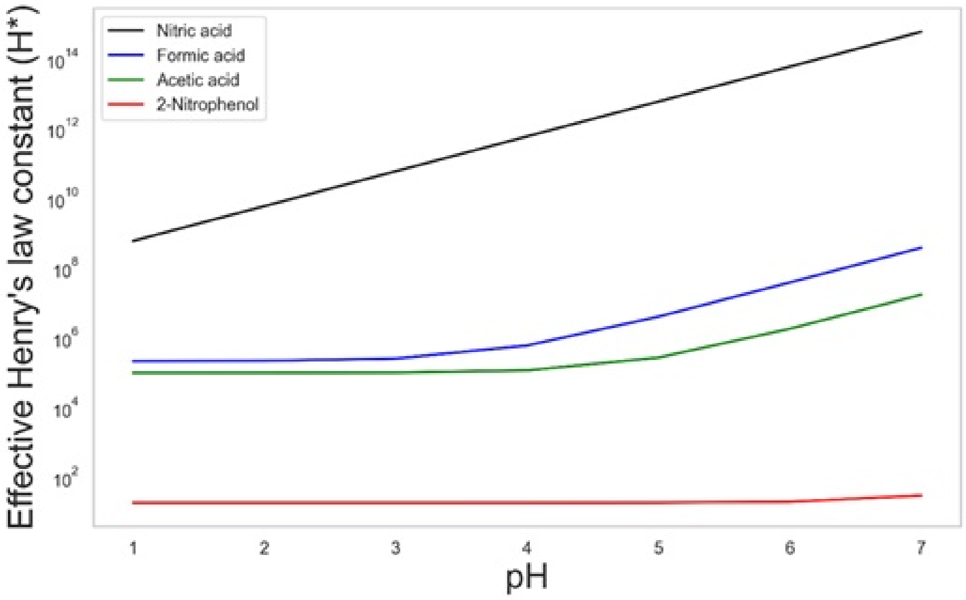

Figure A.4: Variation of effective Henry's constant as a function of pH at 25°C for nitric, formic and acetic acids, and 2-nitrophenol.

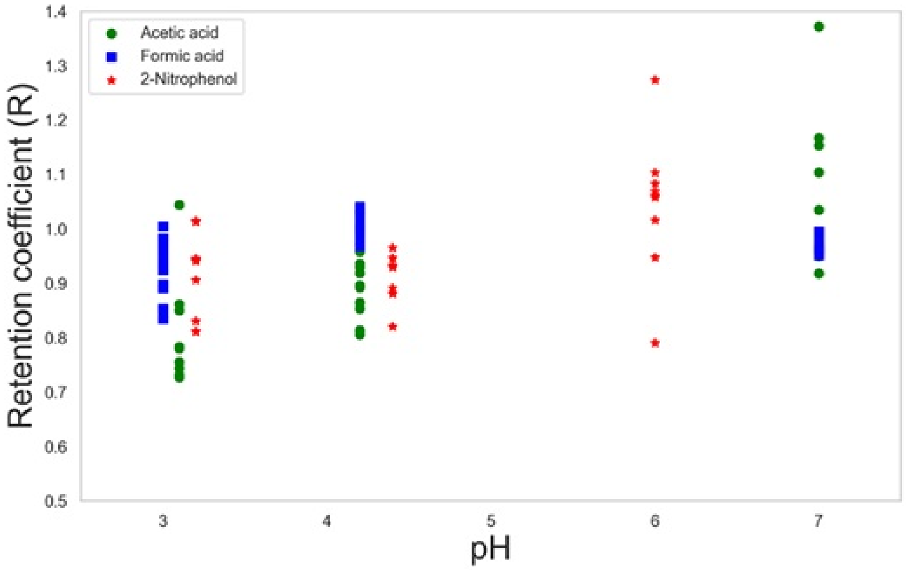

Figure A.5: pH sensitivity of retention coefficients of single components, complementary to Figure 4.2(a) of the manuscript.

A.2 Appendix for Chapter 6

A.2.1 Appendix A: Size dependent variabilities of characteristic timescales

Ice-shell formation time

The measurement dataset was trimmed to include only drops within 2 ± 0.2 mm in diameter, in order to check for any biases in the data arising due to variation in drop sizes. The trimmed dataset consisted of 140 drops. Figures A.6 and A.7 are analogous to the Figures 6.6 and 6.7. The variation of ice-shell formation time for 2 ± 0.2 mm maintains the similar trend seen for the entire size range (Fig. 6.6). As seen earlier, ice-shell formation time increases for warmer freezing temperatures. A strong linear dependency for the ice-shell formation time on drop freezing temperatures can also be seen for the trimmed dataset ($p = 8.60 \times 10^{-9}$). The reduction in ice-shell formation time for drops with ventilation was about 8.68% as compared to drops without external ventilation, also with large standard deviations.

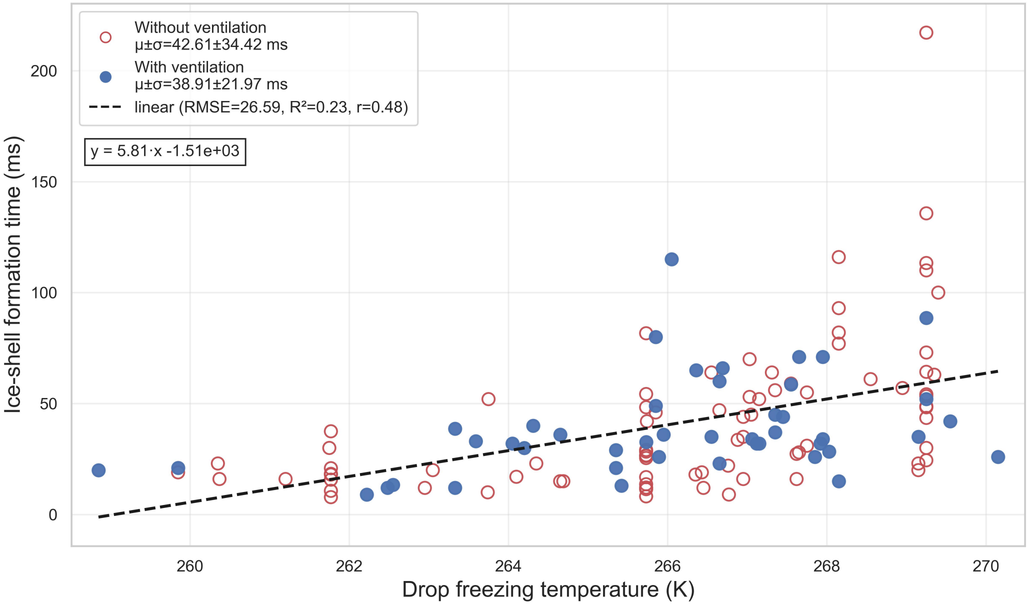

Figure A.6: Ice-shell formation time as a function of the drop freezing temperature for 2 ± 0.2 mm drops.

However, in contrast to drop freezing temperatures, ice-shell formation did not show any significant dependency on ambient temperatures for 2 ± 0.2 mm drops, with $p = 0.59$. It can be seen in Fig A.7 that ice-shell formation time is almost independent of the ambient temperature for the trimmed dataset, compared to the entire size range seen in Fig. 6.7.

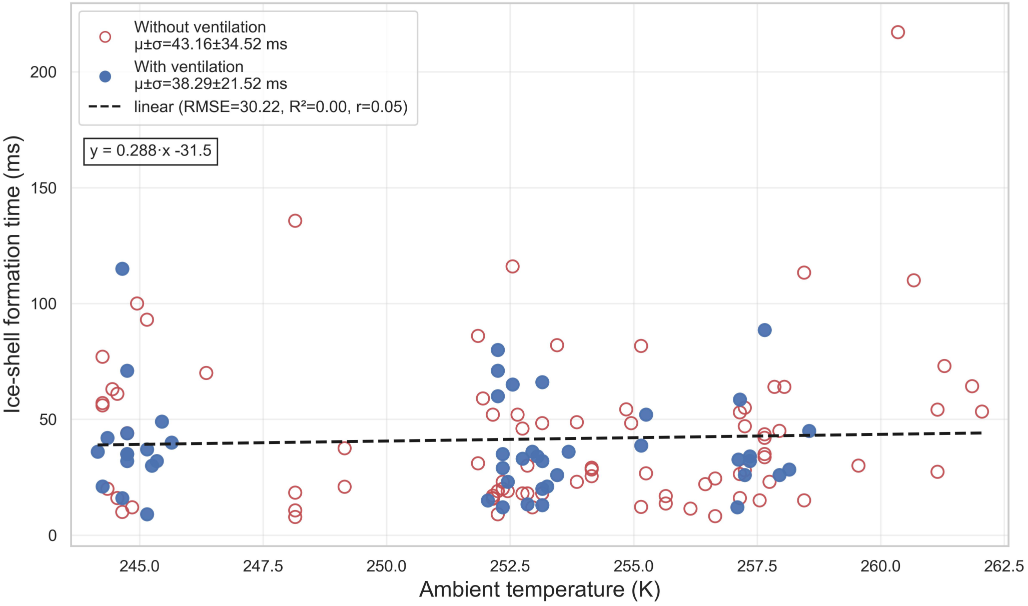

Figure A.7: Ice-shell formation time as a function of the ambient temperature for 2 ± 0.2 mm drops.

Adiabatic freezing time

The size dependent variability of adiabatic freezing time on drop freezing and ambient temperatures is shown in Figures A.8 and A.9, respectively, which comprised 140 drops in the 2 ± 0.2 mm size range. The adiabatic freezing time showed a mildly decreasing trend with drop freezing temperatures, which can also be seen through its negative correlation coefficient of $r = -0.08$. This negative trend is, however, not statistically significant ($p = 0.43$), owing to large scatter in the dataset.

The trimmed dataset for 2 ± 0.2 mm sized drops in Fig. A.9 maintains a similar variability for the dependence of adiabatic freezing time on ambient temperature, seen previously in Fig. 6.12. Colder ambient temperatures led to faster adiabatic freezing time. Faster crystal growth rates at colder temperatures can be attributed to the observed shorter average adiabatic freezing time, for both size dependent and size independent scenarios.

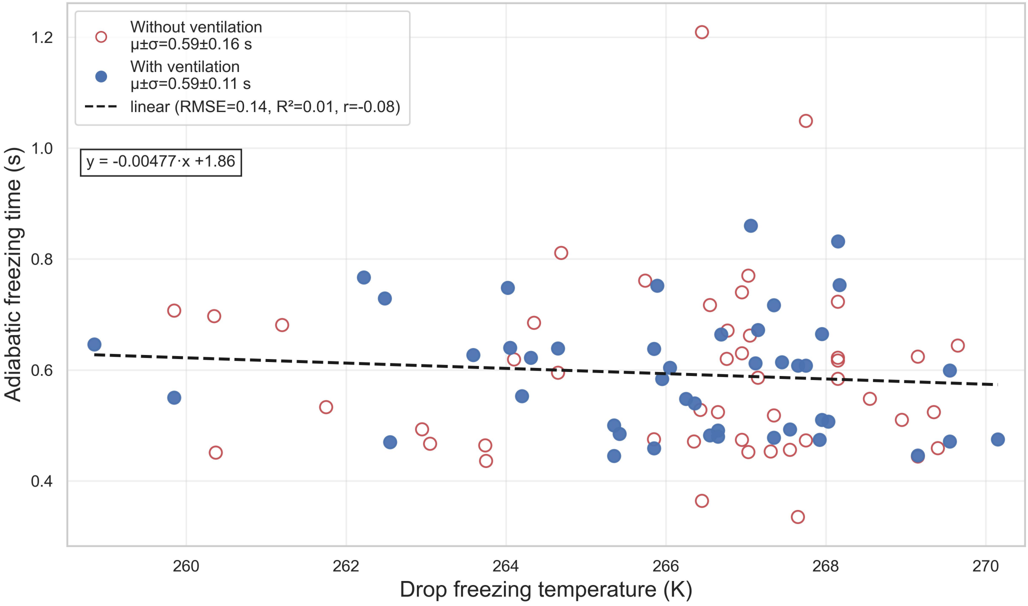

Figure A.8: Adiabatic freezing time as a function of the drop freezing temperature for 2 ± 0.2 mm drops.

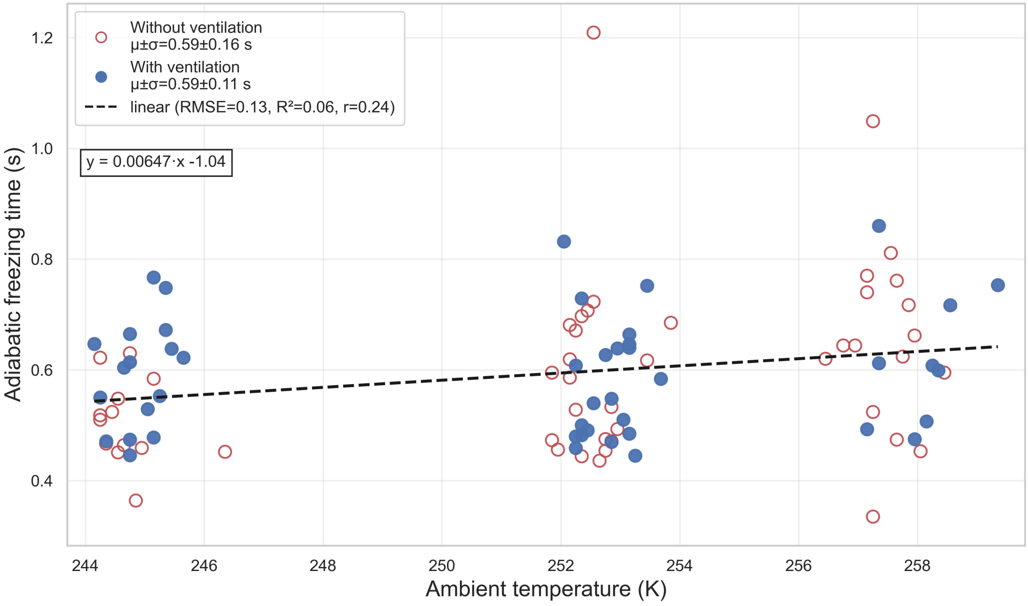

Figure A.9: Adiabatic freezing time as a function of the ambient temperature for 2 ± 0.2 mm drops.

Diabatic freezing time

Diabatic freezing times for 2± 0.2 mm sized drops showed a stronger correlation on drop freezing temperature (Fig. A.10, $r = 0.22$), as compared to its size dependent variation seen in Fig. 6.16 ($r = 0.13$). Linear regression tests also revealed a significant dependence on drop freezing temperature for the size independent case, with $p = 0.04$. This significance is, however, very close to the limiting value of $p = 0.05$.

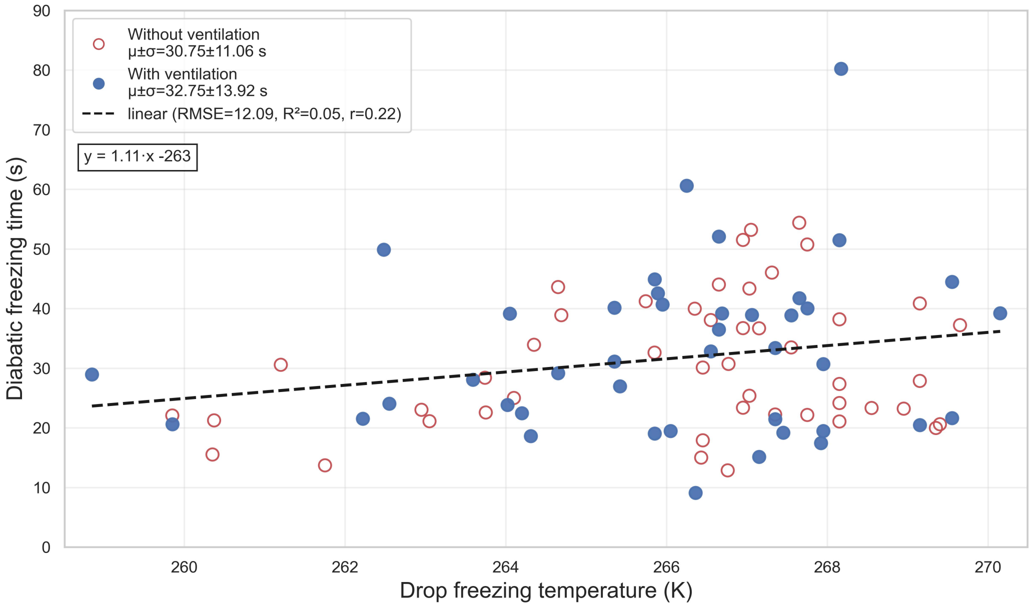

Figure A.10: Diabatic freezing time as a function of the drop freezing temperature for 2 ± 0.2 mm drops.

With respect to ambient temperatures, size dependent diabatic freezing times showed a highly significant linear dependency, with $p = 1.1 \times 10^{-11}$. Also, a much stronger correlation can be seen for size dependent diabatic freezing times, with $r = 0.67$.

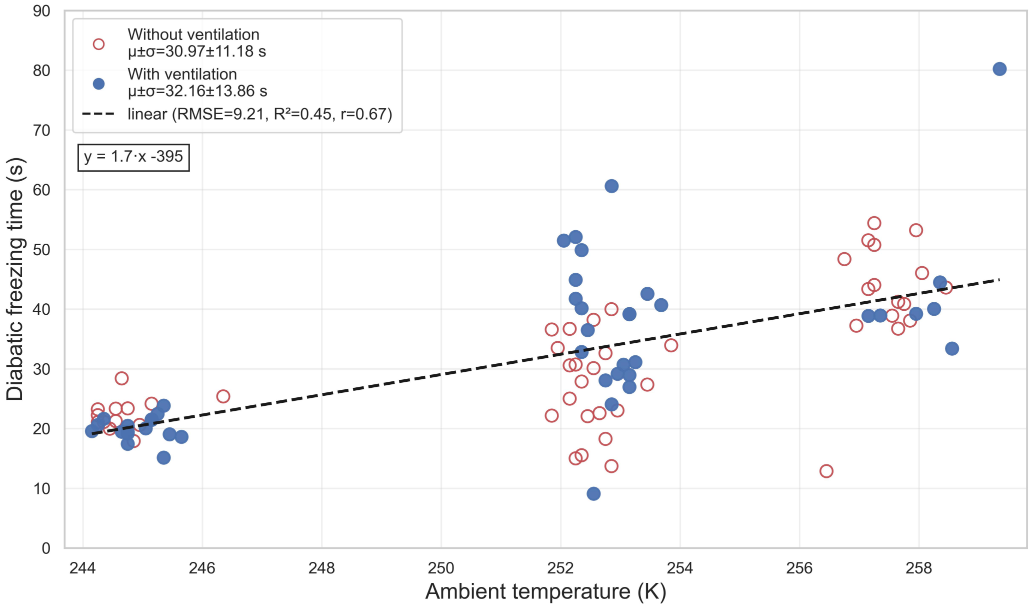

Figure A.11: Diabatic freezing time as a function of the ambient temperature for 2 ± 0.2 mm drops.

A.2.2 Appendix B: Correlation among the variables

Here, the dependencies and variations of the characteristic timescales: ice-shell formation time, diabatic and adiabatic freezing times on experimental variables: drop diameter, drop freezing temperature, ambient cold room temperature, and concentration of INPs are shown. A correlation matrix using Pearson's correlation coefficient was generated for the above mentioned parameters collectively and shown in Fig. A.12. Positive correlations are indicated in shades of red and negative correlations in shades of blue. While generating the correlation matrix, all the rows of the parameters and variables that had at least one empty value were omitted. Hence, the correlation coefficients shown here and in Figures 6.6 to 6.20 are slightly different. For instance, in Fig. 6.6, rows with missing values from ice-shell formation time and drop freezing temperature were omitted. The correlation coefficient found in Fig. 6.6 was 0.47, as opposed to 0.44 in Fig. A.12 for the same two parameters. Nevertheless, the difference is insignificant, and a general form of dependencies among the experimental variables could be seen collectively in Fig. A.12.

For ice-shell formation time, drop freezing temperature (0.44) and concentration of INP (-0.50) showed the highest correlation. Diabatic freezing time had the strongest correlation with cold room temperature (0.45). For adiabatic freezing time, drop diameter (0.26) showed the highest correlation.

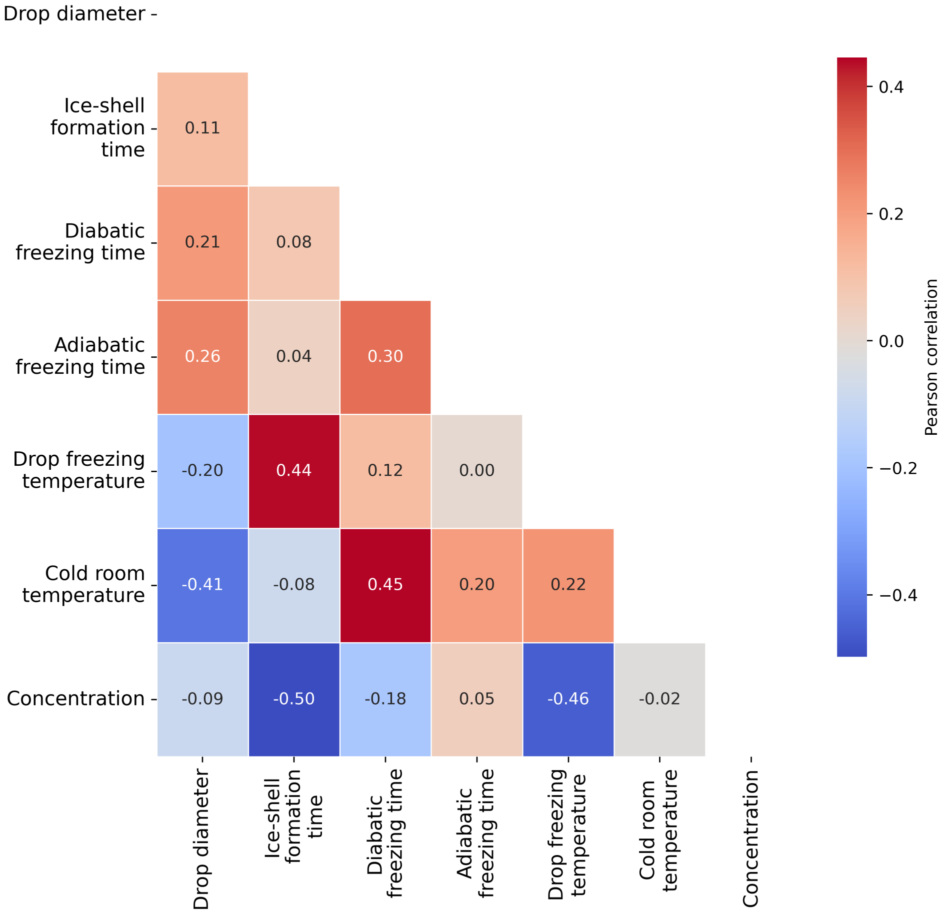

Figure A.12: Correlation matrix between the characteristic timescales, temperatures, size, and INP concentrations. Red color indicating higher positive correlation, and blue color indicating negative correlation among the variables.

A.2.3 Appendix C: Some interrelationships among the timescales

Some relationships among the characteristic timescales are discussed in this section. The ratio of ice-shell formation time to adiabatic freezing time (Is-A ratio) is plotted against drop sizes in Fig. A.13a. For the majority of the experiments, the ice-shell formation time was between 3.5 and 9

In Fig. A.13b, the ratio of ice-shell formation time to the diabatic freezing time (Is-D ratio) is shown. On average, diabatic freezing time was found to be about 3 orders of magnitude larger than the time taken for the formation of ice-shell. Here, for the majority of the drops, ice-shell formation time was found to be about 0.07 to 0.18 % of the diabatic freezing time. And experiments performed at colder temperatures (-20 and -28 °C) showed larger variation, maximum ratio being 0.71%

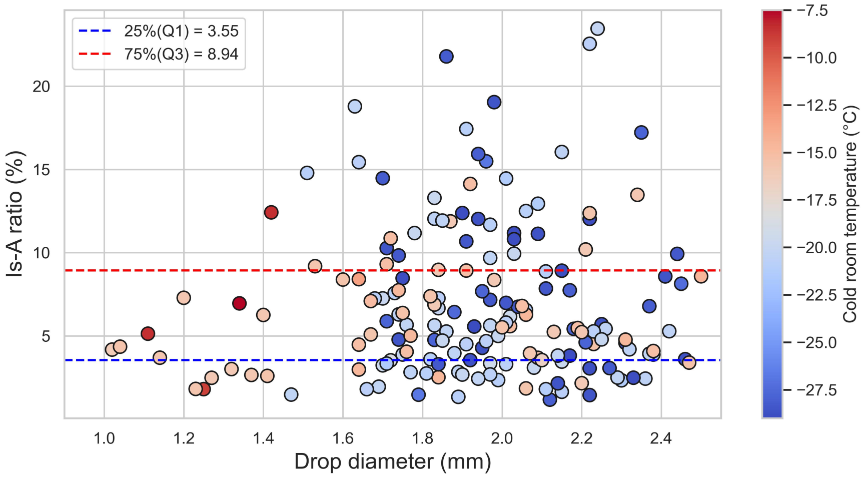

(a) Ratio of ice-shell formation time to adiabatic freezing time as a function of drop sizes.

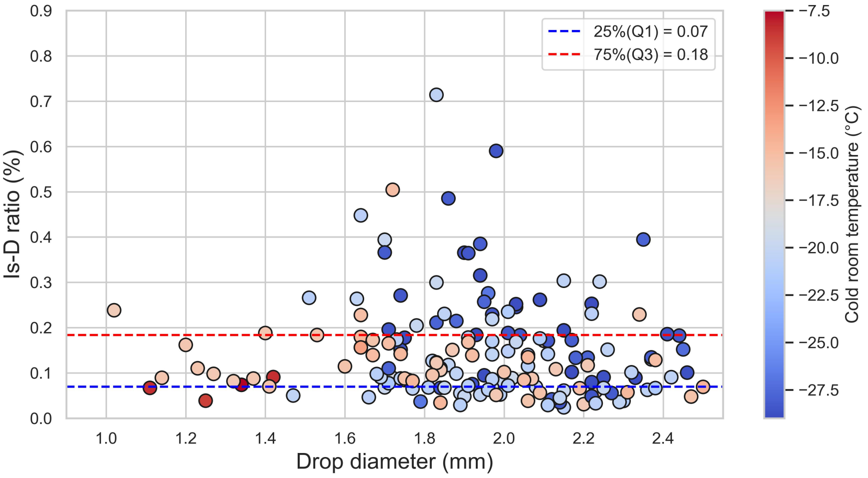

(b) Ratio of ice-shell formation time to diabatic freezing time as a function of drop sizes.

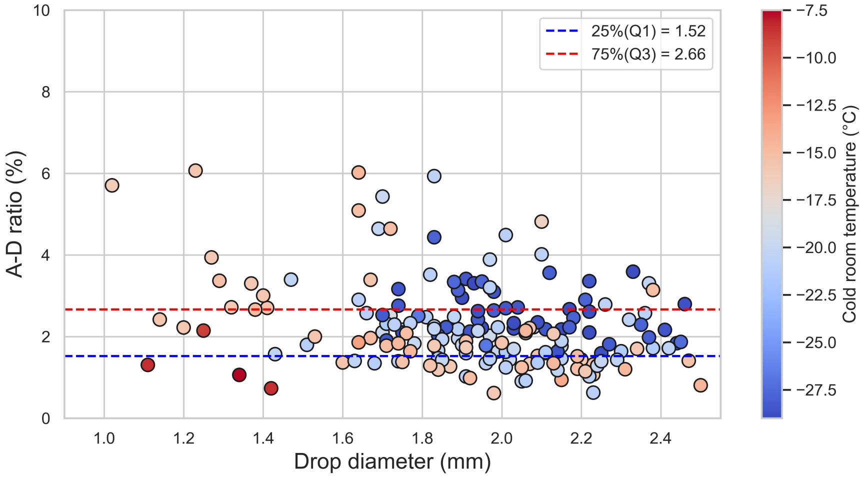

(c) Ratio of adiabatic freezing time to diabatic freezing time as a function of drop sizes

Figure A.13: Interrelationship among ice-shell formation time, diabatic and adiabatic freezing times.

Similarly, the ratio of adiabatic to diabatic freezing time (A-D ratio), as a function of drop diameter, is shown in Fig. A.13c. The adiabatic freezing stage was found to be about 1.5 to 2.5% of the longer diabatic freezing stage, on average. Here, larger deviations were observed for experiments performed at -15 and -20 °C, and for drops smaller than 1.8 mm. For comparatively slower cooling rates, the heat exchange from the drop to the environment during freezing took longer, thus increasing the A-D ratios. Maximum adiabatic freezing time was about 6% of the diabatic freezing time.

Nomenclature

Abbreviations

BET	Brunauer–Emmett–Teller method
CCN	Cloud condensation nuclei
HPLC	High performance liquid chromatography
IC	Ion chromatography
INAS	Ice nucleating active sites
INP	Ice nucleating particle
M-AL	Mainz Acoustic Levitator
MMT	Montmorillionite
NPF	New particle formation
PBL	Planetary boundary layer
PMT	Purified montmorillonite
RMSE	Root mean square error
SOA	Secondary organic aerosol
UTLS	Upper troposphere and lower stratosphere
VOC	Volatile organic compounds

Symbols

α	Mass accommodation coefficient	
ΔT	Supercooling temperature	°C
δ	Thickness of ice-shell	m
ρ_v	Density of water vapor	kg/m^3

ρ_w	Density of water	$\mathrm{kg/m^3}$
τ	Drop relaxation time	s
τ_{ad}	Diabatic freezing time	s
τ_{aq}	Aqueous expulsion time	s
τ_d	Adiabatic freezing time	s
τ_{exp}	Total solute mass expulsion time	s
τ_{frz}	Freezing time of a drop (= ice-shell formation time for retention indicator calculations)	s
τ_g	Gaseous expulsion time	s
τ_i	Interfacial mass expulsion time	s
τ_r	Expulsion time due to aqueous reactions	s
a	Drop radius	m
A_{T1}	Normalized adiabatic freezing time as a function of drop freezing temperature	$\mathrm{s/mm^2}$
A_{T2}	Normalized adiabatic freezing time as a function of ambient temperature	$\mathrm{s/mm^2}$
c	Concentration	mg/L
c_p	Specific heat capacity of water	kJ/(kg K)
D	Desorption coefficient	
D_{aq}	Aqueous diffusivity	$\mathrm{cm^2/s}$
D_g	Gaseous diffusivity	$\mathrm{cm^2/s}$
D_{T1}	Normalized adiabatic freezing time as a function of drop freezing temperature	$\mathrm{s/mm^2}$
D_{T2}	Normalized adiabatic freezing time as a function of ambient temperature	$\mathrm{s/mm^2}$
D_v	Diffusivity of water vapor	$\mathrm{cm^2/s}$
F	Freezing rate	
f	Ventilation coefficient	
f_h	Ventilation coefficient for mass transfer	
f_v	Ventilation coefficient for heat transfer	
f_{ice}	Frozen fraction	
f_{mass}	Frozen mass fraction of a drop	

$G^{'}$	Growth velocity for adiabatic freezing time estimation	m/s
G_{m1}	Crystal growth rate for drop circumference	m/s
G_{m1}	Crystal growth rate for drop radius	m/s
H^*	Dimensionless effective Henry's constant	
I_c	Solute concentration dependent ice-shell formation time	ms
I_{T1}	Normalized ice-shell formation time as a function of drop freezing temperature	s/m
I_{T2}	Normalized ice-shell formation time as a function of ambient temperature	s/m
J_s	Homogeneous nucleation rate	
J_v	Heterogeneous nucleation rate	
J_h	Conductive heat flux density	$\mathrm{W/m^2}$
k_a	Thermal conductivity in air	W/(m K)
k_{int}	Empirical intrinsic kinetic coefficient	m/(K s
K_t	Cumulative nucleus spectra	
L_e	Latent heat of evaporation	kJ/kg
L_f	Latent heat of freezing	kJ/kg
L_m	Latent heat of melting	kJ/kg
m, m_{tot}	Total mass of the drop	kg
m_{ice}	Mass of frozen part of a drop	kg
N_f	No. of frozen drops	
N_o	Total no. of drops	
n_s	INAS density	$\#/\mathrm{m^2}$
q	Diffusional heat	J
R	Retention coefficient	
R_i	Initial retention coefficient	
RI	Retention indicator	
S	Drop surface area	$\mathrm{m^2}$
SSA	Specific surface area	$\mathrm{m^2/g}$

t	Time	s
t'_{ad}	Estimated adiabatic freezing time	s
t'_{D}	Estimated diabatic freezing time	s
T_0	Freezing point of water	°C or K
T_f	Drop freezing temperature	°C or K
T_∞	Ambient room temperature	°C or K
V	Volume	m^3
v	Thermal velocity	m/s
x	Radial distance from drop center	m
r	Pearson's correlation coefficient	

Bibliography

Abbatt, J. P. (2003). Interactions of atmospheric trace gases with ice surfaces: Adsorption and reaction. *Chemical reviews*, 103(12):4783–4800.

Ambroz, F., Macdonald, T. J., Martis, V., and Parkin, I. P. (2018). Evaluation of the bet theory for the characterization of meso and microporous mofs. *Small methods*, 2(11):1800173.

Andreae, M. O. (2019). Emission of trace gases and aerosols from biomass burning–an updated assessment. *Atmospheric Chemistry and Physics*, 19(13):8523–8546.

Andreae, M. O. and Crutzen, P. J. (1997). Atmospheric aerosols: Biogeochemical sources and role in atmospheric chemistry. *Science*, 276(5315):1052–1058.

Baltensperger, U., Kalberer, M., Dommen, J., Paulsen, D., Alfarra, M. R., Coe, H., Fisseha, R., Gascho, A., Gysel, M., Nyeki, S., et al. (2005). Secondary organic aerosols from anthropogenic and biogenic precursors. *Faraday Discussions*, 130:265–278.

Bardakov, R., Krejci, R., Riipinen, I., and Ekman, A. M. (2022). The role of convective up-and downdrafts in the transport of trace gases in the amazon. *Journal of Geophysical Research: Atmospheres*, 127(18):e2022JD037265.

Bardakov, R., Thornton, J. A., Riipinen, I., Krejci, R., and Ekman, A. M. (2021). Transport and chemistry of isoprene and its oxidation products in deep convective clouds. *Tellus B: Chemical and Physical Meteorology*, 73(1):1–21.

Barth, M., Kim, S.-W., Wang, C., Pickering, K., Ott, L., Stenchikov, G., Leriche, M., Cautenet, S., Pinty, J.-P., Barthe, C., et al. (2007). Cloud-scale model intercomparison of chemical constituent transport in deep convection. *Atmospheric Chemistry and Physics*, 7(18):4709–4731.

Barth, M., Stuart, A. L., and Skamarock, W. (2001). Numerical simulations of the july 10, 1996, stratospheric-tropospheric experiment: Radiation, aerosols, and ozone (sterao)-deep convection experiment storm: Redistribution of soluble tracers. *Journal of Geophysical Research: Atmospheres*, 106(D12):12381–12400.

Bela, M. M., Barth, M. C., Toon, O. B., Fried, A., Homeyer, C. R., Morrison, H., Cummings, K. A., Li, Y., Pickering, K. E., Allen, D. J., et al. (2016). Wet scavenging of soluble gases in dc3 deep convective storms using wrf-chem simulations and aircraft observations. *Journal of Geophysical Research: Atmospheres*, 121(8):4233–4257.

Borchers, C., Seymore, J., Gautam, M., Dörholt, K., Müller, Y., Arndt, A., Gömmer, L., Ungeheuer, F., Szakáll, M., Borrmann, S., et al. (2024). Retention of α-pinene oxidation products and nitro-aromatic compounds during riming. *Atmospheric Chemistry and Physics*, 24(24):13961–13974.

Boucher, O., Randall, D., Artaxo, P., Bretherton, C., Feingold, G., Forster, P., Kerminen, V.-M., Kondo, Y., Liao, H., Lohmann, U., et al. (2013). Clouds and aerosols. In *Climate change 2013: The physical science basis. Contribution of working group I to the fifth assessment report of the intergovernmental panel on climate change*, pages 571–657. Cambridge University Press.

Brand, A. (2014). Experimentelle untersuchungen des retentionskoeffizienten organischer säuren in wassertropfen. Diploma thesis, University of Mainz, Germany.

Broadley, S., Murray, B., Herbert, R., Atkinson, J., Dobbie, S., Malkin, T., Condliffe, E., and Neve, L. (2012). Immersion mode heterogeneous ice nucleation by an illite rich powder representative of atmospheric mineral dust. *Atmospheric Chemistry and Physics*, 12(1):287–307.

Cantrell, W. and Heymsfield, A. (2005). Production of ice in tropospheric clouds: A review. *Bulletin of the American Meteorological Society*, 86(6):795–808.

Carlton, A., Wiedinmyer, C., and Kroll, J. (2009). A review of secondary organic aerosol (soa) formation from isoprene. *Atmospheric Chemistry and Physics*, 9(14):4987–5005.

Chapman, E., Sklarew, D., and Flickinger, J. (1986). Organic acids in springtime wisconsin precipitation samples. *Atmospheric Environment (1967)*, 20(9):1717–1725.

Chebbi, A. and Carlier, P. (1996). Carboxylic acids in the troposphere, occurrence, sources, and sinks: A review. *Atmospheric Environment*, 30(24):4233–4249.

Cohen, A. J., Brauer, M., Burnett, R., Anderson, H. R., Frostad, J., Estep, K., Balakrishnan, K., Brunekreef, B., Dandona, L., Dandona, R., et al. (2017). Estimates and 25-year trends of the global burden of disease attributable to ambient air pollution: an analysis of data from the global burden of diseases study 2015. *The lancet*, 389(10082):1907–1918.

Connolly, P., Möhler, O., Field, P., Saathoff, H., Burgess, R., Choularton, T., and Gallagher, M. (2009). Studies of heterogeneous freezing by three different desert dust samples. *Atmospheric Chemistry and Physics*, 9(8):2805–2824.

Corti, T., Luo, B., De Reus, M., Brunner, D., Cairo, F., Mahoney, M., Martucci, G., Matthey, R., Mitev, V., Dos Santos, F., et al. (2008). Unprecedented evidence for deep convection hydrating the tropical stratosphere. *Geophysical Research Letters*, 35(10).

Cuchiara, G., Fried, A., Barth, M., Bela, M., Homeyer, C., Gaubert, B., Walega, J., Weibring, P., Richter, D., Wennberg, P., et al. (2020). Vertical transport, entrainment, and scavenging processes affecting trace gases in a modeled and observed seac4rs case study. *Journal of Geophysical Research: Atmospheres*, 125(11):e2019JD031957.

Cuchiara, G., Fried, A., Barth, M., Bela, M., Homeyer, C., Walega, J., Weibring, P., Richter, D., Woods, S., Beyersdorf, A., et al. (2023). Effect of marine and land convection on wet scavenging of ozone precursors observed during a seac4rs case study. *Journal of Geophysical Research: Atmospheres*, 128(5):e2022JD037107.

Davidovits, P., Kolb, C. E., Williams, L. R., Jayne, J. T., and Worsnop, D. R. (2006). Mass accommodation and chemical reactions at gas- liquid interfaces. *Chemical reviews*, 106(4):1323–1354.

DeMott, P. J., Möhler, O., Cziczo, D. J., Hiranuma, N., Petters, M. D., Petters, S. S., Belosi, F., Bingemer, H. G., Brooks, S. D., Budke, C., et al. (2018). The fifth international workshop on ice nucleation phase 2 (fin-02): laboratory intercomparison of ice nucleation measurements. *Atmospheric Measurement Techniques*, 11(11):6231–6257.

Diehl, K., Debertshäuser, M., Eppers, O., Schmithüsen, H., Mitra, S., and Borrmann, S. (2014). Particle surface area dependence of mineral dust in immersion freezing mode: investigations with freely suspended drops in an acoustic levitator and a vertical wind tunnel. *Atmospheric Chemistry and Physics*, 14(22):12343–12355.

Diehl, K., Simmel, M., and Wurzler, S. (2006). Numerical sensitivity studies on the impact of aerosol properties and drop freezing modes on the glaciation, microphysics, and dynamics of clouds. *Journal of Geophysical Research: Atmospheres*, 111(D7).

Ervens, B. (2015). Modeling the processing of aerosol and trace gases in clouds and fogs. *Chemical reviews*, 115(10):4157–4198.

Ervens, B., George, C., Williams, J., Buxton, G., Salmon, G., Bydder, M., Wilkinson, F., Dentener, F., Mirabel, P., Wolke, R., et al. (2003). Capram 2.4 (modac mechanism): An extended and condensed tropospheric aqueous phase mechanism and its application. *Journal of Geophysical Research: Atmospheres*, 108(D14):4226–4247.

Fan, W., Chen, T., Zhu, Z., Zhang, H., Qiu, Y., and Yin, D. (2022). A review of secondary organic aerosols formation focusing on organosulfates and organic nitrates. *Journal of Hazardous Materials*, 430:128406.

Field, P. R., Lawson, R. P., Brown, P. R., Lloyd, G., Westbrook, C., Moisseev, D., Miltenberger, A., Nenes, A., Blyth, A., Choularton, T., et al. (2017). Secondary ice production: Current state of the science and recommendations for the future. *Meteorological Monographs*, 58:7–1.

Gautam, M. and coauthors (2024). Retention during freezing of raindrops, part i: Investigation of single and binary mixtures. `https://doi.org/10.5281/zenodo.14319648`.

Gautam, M., Theis, A., Seymore, J., Hey, M., Borrmann, S., Diehl, K., Mitra, S. K., and Szakáll, M. (2025). Retention during freezing of raindrops–part 1: Investigation of single and binary mixtures of nitric, formic, and acetic acids and 2-nitrophenol. *Atmospheric Chemistry and Physics*, 25(19):11813–11828.

Gokhale, N. R. and Lewinter, O. (1971). Microcinematographic studies of contact nucleation. *Journal of Applied Meteorology and Climatology*, 10(3):469–473.

Graedel, T. (2012). *Chemical compounds in the atmosphere*. Elsevier.

Gunz, D. W. and Hoffmann, M. R. (1990). Field investigations on the snow chemistry in central and southern california—ii. carbonyls and carboxylic acids. *Atmospheric Environment. Part A. General Topics*, 24(7):1673–1684.

Hallett, J. (1964). Experimental studies of the crystallization of supercooled water. *Journal of Atmospheric Sciences*, 21(6):671–682.

Haynes, W. M. (2016). *CRC handbook of chemistry and physics*. CRC press.

Haywood, J. and Boucher, O. (2000). Estimates of the direct and indirect radiative forcing due to tropospheric aerosols: A review. *Reviews of geophysics*, 38(4):513–543.

Henry, W. (1803). Iii. experiments on the quantity of gases absorbed by water, at different temperatures, and under different pressures. *Philosophical Transactions of the Royal Society of London*, 93:29–274.

Hindmarsh, J., Russell, A., and Chen, X. (2003). Experimental and numerical analysis of the temperature transition of a suspended freezing water droplet. *International Journal of Heat and Mass Transfer*, 46(7):1199–1213.

Hiranuma, N., Auvermann, B. W., Belosi, F., Bush, J., Cory, K. M., Georgakopoulos, D. G., Höhler, K., Hou, Y., Lacher, L., Saathoff, H., et al. (2021). Laboratory and field studies of ice-nucleating particles from open-lot livestock facilities in texas. *Atmospheric Chemistry and Physics*, 21(18):14215–14234.

Hodzic, A., Campuzano-Jost, P., Bian, H., Chin, M., Colarco, P. R., Day, D. A., Froyd, K. D., Heinold, B., Jo, D. S., Katich, J. M., et al. (2020). Characterization of organic aerosol across the global remote troposphere: a comparison of atom measurements and global chemistry models. *Atmospheric Chemistry and Physics*, 20(8):4607–4635.

Homeyer, C. R., Pan, L. L., Dorsi, S. W., Avallone, L. M., Weinheimer, A. J., O'Brien, A. S., DiGangi, J. P., Zondlo, M. A., Ryerson, T. B., Diskin, G. S., et al. (2014). Convective transport of water vapor into the lower stratosphere observed during double-tropopause events. *Journal of Geophysical Research: Atmospheres*, 119(18):10–941.

Hoose, C. and Möhler, O. (2012). Heterogeneous ice nucleation on atmospheric aerosols: a review of results from laboratory experiments. *Atmospheric Chemistry and Physics*, 12(20):9817–9854.

Hussain, S. and Haji-Akbari, A. (2021). Role of nanoscale interfacial proximity in contact freezing in water. *Journal of the American Chemical Society*, 143(5):2272–2284.

Ickes, L., Welti, A., Hoose, C., and Lohmann, U. (2015). Classical nucleation theory of homogeneous freezing of water: thermodynamic and kinetic parameters. *Physical Chemistry Chemical Physics*, 17(8):5514–5537.

Iribarne, J., Barrie, L., and Iribarne, A. (1983). Effect of freezing on sulfur dioxide dissolved in supercooled droplets. *Atmospheric Environment (1967)*, 17(5):1047–1050.

Iribarne, J., Pyshnov, T., and Naik, B. (1990). The effect of freezing on the composition of supercooled droplets—ii. retention of s (iv). *Atmospheric Environment. Part A. General Topics*, 24(2):389–398.

Johnson, B. J., Betterton, E. A., and Craig, D. (1996). Henry's law coefficients of formic and acetic acids. *Journal of Atmospheric Chemistry*, 24:113–119.

Jost, A. (2017). *A Wind Tunnel Investigation on the Effects of Accretional Growth of Ice Hydrometeors: Implications on Microphysics and Organic Chemistry.* Phd thesis, University of Mainz, Germany.

Jost, A., Szakáll, M., Diehl, K., Mitra, S. K., and Borrmann, S. (2017). Chemistry of riming: the retention of organic and inorganic atmospheric trace constituents. *Atmospheric Chemistry and Physics*, 17(16):9717–9732.

Kanakidou, M., Myriokefalitakis, S., and Tsigaridis, K. (2018). Aerosols in atmospheric chemistry and biogeochemical cycles of nutrients. *Environmental Research Letters*, 13(6):063004.

Kanji, Z. A., Ladino, L. A., Wex, H., Boose, Y., Burkert-Kohn, M., Cziczo, D. J., and Krämer, M. (2017). Overview of ice nucleating particles. *Meteorological monographs*, 58:1–1.

Kar, A., Bhati, A., Lokanathan, M., and Bahadur, V. (2021). Faster nucleation of ice at the three-phase contact line: Influence of interfacial chemistry. *Langmuir*, 37(43):12673–12680.

Kaufman, Y. and Tanré, D. (2003). Satellite remote sensing — aerosol measurements. In Holton, J. R., editor, *Encyclopedia of Atmospheric Sciences*, pages 1941–1956. Academic Press, Oxford.

Kiselev, A., Bachmann, F., Pedevilla, P., Cox, S. J., Michaelides, A., Gerthsen, D., and Leisner, T. (2017). Active sites in heterogeneous ice nucleation—the example of k-rich feldspars. *Science*, 355(6323):367–371.

Kleinheins, J., Kiselev, A., Keinert, A., Kind, M., and Leisner, T. (2021). Thermal imaging of freezing drizzle droplets: pressure release events as a source of secondary ice particles. *Journal of the Atmospheric Sciences*, 78(5):1703–1713.

Kolb, C., Cox, R. A., Abbatt, J., Ammann, M., Davis, E., Donaldson, D., Garrett, B. C., George, C., Griffiths, P., Hanson, D., et al. (2010). An overview of current issues in the uptake of atmospheric trace gases by aerosols and clouds. *Atmospheric Chemistry and Physics*, 10(21):10561–10605.

Koopal, L. (1978). *Inference of polymer adsorption from electrical double layer measurements: the silver iodide-polyvinyl alcohol system.* Wageningen University and Research.

Korolev, A. and Leisner, T. (2020). Review of experimental studies of secondary ice production. *Atmospheric Chemistry and Physics*, 20(20):11767–11797.

Korolev, A. V. and Mazin, I. P. (2003). Supersaturation of water vapor in clouds. *Journal of the atmospheric sciences*, 60(24):2957–2974.

Lamb, D. and Blumenstein, R. (1987). Measurement of the entrapment of sulfur dioxide by rime ice. *Atmospheric Environment (1967)*, 21(8):1765–1772.

Lauber, A., Kiselev, A., Pander, T., Handmann, P., and Leisner, T. (2018). Secondary ice formation during freezing of levitated droplets. *Journal of the Atmospheric Sciences*, 75(8):2815–2826.

Lindberg, V. (2000). Uncertainties and error propagation. *Manual on Uncertainties, Graphing and the Vernier Caliper, Part I. Rochester Institute of Technology, New York, USA.(http://www. rit. edu/uphysics/uncertinities/Uncertinitiespart2. html# addsub).*

Lindenmayer, C. S. (1959). *The Solidification of Supercooled Aqueous Solutions.* Phd thesis, Harvard University, USA.

Lohmann, U. and Feichter, J. (2005). Global indirect aerosol effects: a review. *Atmospheric Chemistry and Physics*, 5(3):715–737.

Long, Y., Chaumerliac, N., Deguillaume, L., Leriche, M., and Champeau, F. (2010). Effect of mixed-phase cloud on the chemical budget of trace gases: A modeling approach. *Atmospheric Research*, 97(4):540–554.

Marcolli, C., Nagare, B., Welti, A., and Lohmann, U. (2016). Ice nucleation efficiency of agi: review and new insights. *Atmospheric Chemistry and Physics*, 16(14):8915–8937.

Mari, C., Jacob, D. J., and Bechtold, P. (2000). Transport and scavenging of soluble gases in a deep convective cloud. *Journal of Geophysical Research: Atmospheres*, 105(D17):22255–22267.

Martini, M., Allen, D. J., Pickering, K. E., Stenchikov, G. L., Richter, A., Hyer, E. J., and Loughner, C. P. (2011). The impact of north american anthropogenic emissions and lightning on long-range transport of trace gases and their export from the continent during summers 2002 and 2004. *Journal of Geophysical Research: Atmospheres*, 116(D7):22.

Mayer, A. (2016). Experiments on the immersion freezing process of cellulose particles. Bachelor thesis, University of Mainz, Germany.

McCue, S. W., Wu, B., and Hill, J. M. (2008). Classical two-phase stefan problem for spheres. *Proceedings of the Royal Society A: Mathematical, Physical and Engineering Sciences*, 464(2096):2055–2076.

Mitra, S. and Hannemann, A. (1993). On the scavenging of so 2 by large and small rain drops: V. a wind tunnel and theoretical study of the desorption of so 2 from water drops containing s (iv). *Journal of atmospheric chemistry*, 16:201–218.

Mungall, E. L., Abbatt, J. P., Wentzell, J. J., Wentworth, G. R., Murphy, J. G., Kunkel, D., Gute, E., Tarasick, D. W., Sharma, S., Cox, C. J., et al. (2018). High gas-phase mixing ratios of formic and acetic acid in the high arctic. *Atmospheric Chemistry and Physics*, 18(14):10237–10254.

Murray, B., O'sullivan, D., Atkinson, J., and Webb, M. (2012). Ice nucleation by particles immersed in supercooled cloud droplets. *Chemical Society Reviews*, 41(19):6519–6554.

Myerson, A. S. and Kirwan, D. J. (1977a). Impurity trapping during dendritic crystal growth. 1. computer simulation. *Industrial & Engineering Chemistry Fundamentals*, 16(4):414–420.

Myerson, A. S. and Kirwan, D. J. (1977b). Impurity trapping during dendritic crystal growth. 2. experimental results and correlation. *Industrial & Engineering Chemistry Fundamentals*, 16(4):420–425.

Niedermeier, D., Shaw, R., Hartmann, S., Wex, H., Clauss, T., Voigtländer, J., and Stratmann, F. (2011). Heterogeneous ice nucleation: exploring the transition from stochastic to singular freezing behavior. *Atmospheric Chemistry and Physics*, 11(16):8767–8775.

Paulot, F., Wunch, D., Crounse, J. D., Toon, G., Millet, D. B., DeCarlo, P. F., Vigouroux, C., Deutscher, N. M., González Abad, G., Notholt, J., et al. (2011). Importance of secondary sources in the atmospheric budgets of formic and acetic acids. *Atmospheric Chemistry and Physics*, 11(5):1989–2013.

Peckhaus, A., Kiselev, A., Hiron, T., Ebert, M., and Leisner, T. (2016). A comparative study of k-rich and na/ca-rich feldspar ice-nucleating particles in a nanoliter droplet freezing assay. *Atmospheric Chemistry and Physics*, 16(18):11477–11496.

Pitter, R. and Pruppacher, H. (1973). A wind tunnel investigation of freezing of small water drops falling at terminal velocity in air. *Quarterly Journal of the Royal Meteorological Society*, 99(421):540–550.

Pöschl, U. (2005). Atmospheric aerosols: composition, transformation, climate and health effects. *Angewandte Chemie International Edition*, 44(46):7520–7540.

Pruppacher, H. and Klett, J. (2010). *Microphysics of Clouds and Precipitation.* Springer Science & Business Media.

Pruppacher, H. R. (1967). Some relations between the structure of the ice-solution interface and the free growth rate of ice crystals in supercooled aqueous solutions. *Journal of Colloid and Interface Science*, 25(2):285–294.

Reicher, N., Segev, L., and Rudich, Y. (2018). The weizmann supercooled droplets observation on a microarray (wisdom) and application for ambient dust. *Atmospheric Measurement Techniques*, 11(1):233–248.

Roy, P., Rauber, R. M., and Di Girolamo, L. (2024). Evolution of cloud droplet temperature and lifetime in spatiotemporally varying subsaturated environments with implications for ice nucleation at cloud edges. *Atmospheric Chemistry and Physics*, 24(20):11653–11678.

Ryu, Y.-H. and Min, S.-K. (2022). Improving wet and dry deposition of aerosols in wrf-chem: Updates to below-cloud scavenging and coarse-particle dry deposition. *Journal of Advances in Modeling Earth Systems*, 14(4):e2021MS002792.

Schneider, C. A., Rasband, W. S., and Eliceiri, K. W. (2012). Nih image to imagej: 25 years of image analysis. *Nature methods*, 9(7):671–675.

Schwartz, S. E. (1986). Mass-transport considerations pertinent to aqueous phase reactions of gases in liquid-water clouds. In *Chemistry of multiphase atmospheric systems*, pages 415–471. Springer.

Scott, T. A. (1976). Solid and liquid nitrogen. *Physics Reports*, 27(3):89–157.

Seinfeld, J. H. and Pandis, S. N. (2016). *Atmospheric chemistry and physics: from air pollution to climate change.* John Wiley & Sons.

Sempére, R. and Kawamura, K. (1994). Comparative distributions of dicarboxylic acids and related polar compounds in snow, rain and aerosols from urban atmosphere. *Atmospheric Environment*, 28(3):449–459.

Seymore, J., Gautam, M., Szakáll, M., Theis, A., Hoffmann, T., Ma, J., Zhou, L., and Vogel, A. L. (2025). Retention during freezing of raindrops–part 2: Investigation of ambient organics from beijing urban aerosol samples. *Atmospheric Chemistry and Physics*, 25(19):11829–11845.

Shrivastava, M., Cappa, C. D., Fan, J., Goldstein, A. H., Guenther, A. B., Jimenez, J. L., Kuang, C., Laskin, A., Martin, S. T., Ng, N. L., et al. (2017). Recent advances in understanding secondary organic aerosol: Implications for global climate forcing. *Reviews of Geophysics*, 55(2):509–559.

Snider, J. R. and Huang, J. (1998). Factors influencing the retention of hydrogen peroxide and molecular oxygen in rime ice. *Journal of Geophysical Research: Atmospheres*, 103(D1):1405–1415.

Snider, J. R., Montague, D. C., and Vali, G. (1992). Hydrogen peroxide retention in rime ice. *Journal of Geophysical Research: Atmospheres*, 97(D7):7569–7578.

Sporre, M. K., Blichner, S. M., Schrödner, R., Karset, I. H., Berntsen, T. K., Van Noije, T., Bergman, T., O'donnell, D., and Makkonen, R. (2020). Large difference in aerosol radiative effects from bvoc-soa treatment in three earth system models. *Atmospheric Chemistry and Physics*, 20(14):8953–8973.

Stuart, A. L. and Jacobson, M. (2003). A timescale investigation of volatile chemical retention during hydrometeor freezing: Nonrime freezing and dry growth riming without spreading. *Journal of Geophysical Research: Atmospheres*, 108(D6):4178–4194.

Stuart, A. L. and Jacobson, M. (2004). Chemical retention during dry growth riming. *Journal of Geophysical Research: Atmospheres*, 109(D07):305.

Stuart, A. L. and Jacobson, M. (2006). A numerical model of the partitioning of trace chemical solutes during drop freezing. *Journal of Atmospheric Chemistry*, 53:13–42.

Szakáll, M., Debertshäuser, M., Lackner, C. P., Mayer, A., Eppers, O., Diehl, K., Theis, A., Mitra, S. K., and Borrmann, S. (2021). Comparative study on immersion freezing utilizing single-droplet levitation methods. *Atmospheric Chemistry and Physics*, 21(5):3289–3316.

Thibodeaux, L. J. and Mackay, D. (2010). *Handbook of chemical mass transport in the environment*. CRC Press.

Tost, H., Lawrence, M. G., Brühl, C., Jöckel, P., Team, G., et al. (2010). Uncertainties in atmospheric chemistry modelling due to convection parameterisations and subsequent scavenging. *Atmospheric Chemistry and Physics*, 10(4):1931–1951.

Tremp, J., Mattrel, P., Fingler, S., and Giger, W. (1993). Phenols and nitrophenols as tropospheric pollutants: emissions from automobile exhausts and phase transfer in the atmosphere. *Water, Air, and Soil Pollution*, 68:113–123.

Tröstl, J., Chuang, W. K., Gordon, H., Heinritzi, M., Yan, C., Molteni, U., Ahlm, L., Frege, C., Bianchi, F., Wagner, R., et al. (2016). The role of low-volatility organic compounds in initial particle growth in the atmosphere. *Nature*, 533(7604):527–531.

Tsigaridis, K., Daskalakis, N., Kanakidou, M., Adams, P., Artaxo, P., Bahadur, R., Balkanski, Y., Bauer, S., Bellouin, N., Benedetti, A., et al. (2014). The aerocom evaluation and intercomparison of organic aerosol in global models. *Atmospheric Chemistry and Physics*, 14(19):10845–10895.

Twomey, S. (1974). Pollution and the planetary albedo. *Atmospheric Environment (1967)*, 8(12):1251–1256.

Vali, G. (2014). Interpretation of freezing nucleation experiments: singular and stochastic; sites and surfaces. *Atmospheric Chemistry and Physics*, 14(11):5271–5294.

Vali, G., DeMott, P., Möhler, O., and Whale, T. (2015). A proposal for ice nucleation terminology. *Atmospheric Chemistry and Physics*, 15(18):10263–10270.

von Blohn, N., Diehl, K., Mitra, S., and Borrmann, S. (2011). Wind tunnel experiments on the retention of trace gases during riming: nitric acid, hydrochloric acid, and hydrogen peroxide. *Atmospheric Chemistry and Physics*, 11(22):11569–11579.

von Blohn, N., Diehl, K., Nölscher, A., Jost, A., Mitra, S. K., and Borrmann, S. (2013). The retention of ammonia and sulfur dioxide during riming of ice particles and dendritic snow flakes: laboratory experiments in the mainz vertical wind tunnel. *Journal of Atmospheric Chemistry*, 70:131–150.

Wakata, Y., Chao, X., Sun, C., and Diddens, C. (2024). Evaporation of acoustically levitated bicomponent droplets: Mass and heat transfer characteristics. *Journal of Fluid Mechanics*, 984:A17.

Wang, J., Krejci, R., Giangrande, S., Kuang, C., Barbosa, H. M., Brito, J., Carbone, S., Chi, X., Comstock, J., Ditas, F., et al. (2016). Amazon boundary layer aerosol concentration sustained by vertical transport during rainfall. *Nature*, 539(7629):416–419.

Warneck, P. (1999). *Chemistry of the natural atmosphere*, volume 71. Elsevier.

Warneck, P. and Williams, J. (2012). *The atmospheric chemist's companion: Numerical data for use in the atmospheric sciences*. Springer.

Wildeman, S., Sterl, S., Sun, C., and Lohse, D. (2017). Fast dynamics of water droplets freezing from the outside in. *Physical review letters*, 118(8):084101.

Williamson, C. J., Kupc, A., Axisa, D., Bilsback, K. R., Bui, T., Campuzano-Jost, P., Dollner, M., Froyd, K. D., Hodshire, A. L., Jimenez, J. L., et al. (2019). A large source of cloud condensation nuclei from new particle formation in the tropics. *Nature*, 574(7778):399–403.

Wright, T. P., Petters, M. D., Hader, J. D., Morton, T., and Holder, A. L. (2013). Minimal cooling rate dependence of ice nuclei activity in the immersion mode. *Journal of Geophysical Research: Atmospheres*, 118(18):10–535.

Yarin, A., Pfaffenlehner, M., and Tropea, C. (1998). On the acoustic levitation of droplets. *Journal of Fluid Mechanics*, 356:65–91.

Yau, M. K. and Rogers, R. R. (1996). *A short course in cloud physics*. Elsevier.

Yu, P., Rosenlof, K. H., Liu, S., Telg, H., Thornberry, T. D., Rollins, A. W., Portmann, R. W., Bai, Z., Ray, E. A., Duan, Y., et al. (2017). Efficient transport of tropospheric aerosol into the stratosphere via the asian summer monsoon anticyclone. *Proceedings of the National Academy of Sciences*, 114(27):6972–6977.

Zhang, C. and Harrington, J. Y. (2014). Including surface kinetic effects in simple models of ice vapor diffusion. *Journal of the Atmospheric Sciences*, 71(1):372–390.

Zheng, Y., Chen, Q., Cheng, X., Mohr, C., Cai, J., Huang, W., Shrivastava, M., Ye, P., Fu, P., Shi, X., et al. (2021). Precursors and pathways leading to enhanced secondary organic aerosol formation during severe haze episodes. *Environmental Science & Technology*, 55(23):15680–15693.